UNIVERSITÀ DEGLI STUDI DI PADOVA

DIPARTIMENTO DI SCIENZE CHIMICHE

CORSO DI DOTTORATO DI RICERCA IN SCIENZA E INGEGNERIA DEI MATERIALI E DELLE NANOSTRUTTURE

CICLO XXX

DESIGN AND DEVELOPMENT OF A SICM-EC DEVICE FOR H_2/O_2 DETECTION IN PHOTOELECTROCATALYTIC WATER SPLITTING PROCESS

Tesi redatta con il contributo finanziario del Centro di Studi Interdipartimentale "Giorgio Levi Cases"

COORDINATORE: Ch.mo Prof. Giovanni Mattei

SUPERVISORE: Ch.mo Prof.ssa Giovanna Brusatin

CO-SUPERVISORE: Dott.ssa Monica Giomo

DOTTORANDO: Michele Zanatta

ANNO ACCADEMICO 2017/2018

"Puto multos potuisse ad sapientiam pervenire, nisi putassent se pervenisse, nisi quaedam in se dissimulassent, quaedam opertis oculis transiluissent."

Lucius Annaeus Seneca

Abstract

The last century has seen a skyrocketing role of energy resources. The industrial world was overwhelmed by this dramatic change, making the exploitation of renewable energy resources one of the greatest challenges of 21st century. In this context, hydrogen arises as the most promising candidate to substitute crude oil and an increased interest on this topic has been observed over the last years. In particular, last years saw an increasing interest on this topic. In particular, researchers focused on sustainable methods for hydrogen production: currently, the scientific frontier is represented by photoelectrocatalytic water splitting, the most promising method for hydrogen production through water splitting. In this work, useful results for technological advance in the field of photoelectrocatalytic water splitting are introduced. More specifically, a new, easily realised probe for investigation of catalyst is described: in particular, attention is focused on pH detection over microstructured photoelectrocatalysts during water splitting process. The study, design, fabrication and characterisation of this integrated scanning ion conductance microscope - electrochemical (SICM-EC) probe, with new electrodic material and insulating coating, are presented. Approach to hydrogen sensing through electrochemical measurements using the integrated device as sensing electrode are shown. Influence of different pH on open circuit potential of the sensing probe is described and exploited for investigation on water splitting process over macro and micro electrodes. Microelectrodes covered with Co-Pi photoelectrocatalyst, known for coupling many elements of natural photosynthesis with a self-repairing behaviour, were fabricated. They were used to perform water splitting and data from experimental tests are shown. Finally, a new microfluidic device was designed to combine advantages of photoelectrocatalysis with the positive features of microfluidic systems. Moreover, fluid dynamics in this proposed device is investigated through simulations. Further perspectives include simultaneous pH sensing and topographical imaging of photoelectrocatalysts and deep studies on their behaviour inside a microfluidic system.

Sommario

Nel secolo scorso si è visto un incremento drammatico dell'importanza delle risorse energetiche. Il mondo industriale è stato segnato da questo cambiamento profondo, rendendo lo sfruttamento delle fonti energetiche rinnovabili una delle più grandi sfide del XXI secolo. In questo contesto, l'idrogeno si pone come il candidato più promettente per la sostituzione del petrolio greggio e negli ultimi anni si è visto un interesse crescente su questo argomento. In particolare, i ricercatori si sono concentrati su metodi sostenibili per la produzione di idrogeno: attualmente la frontiera scientifica è rappresentata dalla scissione dell'acqua mediante fotoelettrocatalisi, il metodo più promettente per la produzione di idrogeno mediante la scissione dell'acqua. In questo lavoro vengono introdotti risultati utili per l'avanzamento tecnologico nel campo della scissione fotoelettrocatalitica dell'acqua. Più specificatamente, viene descritta una nuova sonda per lo studio del catalizzatore, facilmente realizzata: in particolare, l'attenzione viene posta sul rilevamento del pH durante il processo di scissione dell'acqua al di sopra di fotoelettrocatalizzatori microstrutturati. Viene presentato lo studio, la progettazione, la fabbricazione e la caratterizzazione di questo dispositivo integrato microscopio a scansione di conduttanza ionica - elettrochimico (SICM-EC), preparato con materiale elettrodico e rivestimento isolante nuovi. Viene mostrato l'approccio al rilevamento di idrogeno attraverso misure elettrochimiche usando il dispositivo integrato come elettrodo di rilevamento. Viene descritta l'influenza che valori diversi di pH hanno sul potenziale di circuito aperto della sonda, sfruttata per l'analisi del processo di scissione dell'acqua su macro e microelettrodi. Sono stati fabbricati microelettrodi ricoperti da fotoelettrocatalizzatore Co-Pi, noto per combinare molti elementi della fotosintesi naturale con un comportamento auto-riparante. Questi microelettrodi sono stati usati per effettuare la scissione dell'acqua e vengono mostrati dati provenienti da prove sperimentali. Infine, è stato progettato un nuovo dispositivo microfluidico per combinare i vantaggi della fotoelettrocatalisi con le caratteristiche positive dei sistemi microfluidici. Inoltre, attraverso simulazioni è studiata la fluidodinamica che avviene in questo dispositivo proposto. Ulteriori prospettive includono il rilevamento simultaneo di pH e l'imaging topografico dei fotoelettrocatalizzatori, con studi approfonditi sul loro comportamento all'interno di un sistema microfluidico.

Index

1 – Introduction

Nowadays, it is common to hear journalists, politicians or in general not science professionals discussing about renewable resources. In some cases, the topic covers the exploitation of molecular hydrogen and its means of production. To understand thoroughly the importance of research on sustainable energy resources, a synthetic introduction on the historical context is helpful.

The last century has seen a skyrocketing role of energy resources. Indeed, the last years of the second industrial revolution (1870-1914) were a life-changing event for the citizens of industrialised countries: they started making contact with mass-produced commodities, ranging from pharmaceutical products to chemicals. In particular, industrial chemistry saw a boom of chemical processes for production of many basic compounds. Some of those processes are still used today: probably the most famous one is the Haber-Bosch process of ammonia production. The following years were interested by the rise of polymer industry: the first studies on synthetic polymers were carried out by the German chemist Hermann Staudinger, who in 1920 published a cutting-edge, landmark paper describing polymerisation.[1] Another credited pioneer in this field of science was the American chemist Wallace Carothers.

The industrial world was overwhelmed by this dramatic change and therefore started looking for new, suitable and convenient resources. Industries switched from coal-based energy production methods to petrol, which was also transformed in oil refineries into more useful products, such as the olefin monomers used in polymer industry. This shift had, of course, a huge geopolitical impact: the continuously increasing industrialisation went along with the rise in energy demand and the industrialised countries started to exploit any mean that could lead to energy independence. Some examples could be easily found in colonisation of Africa by European countries or in the invasion of Korea and China by the Empire of Japan between 1910 and 1937 (and subsequently in war between the Empire of Japan and the United States of America as a reaction to the oil embargo placed by the USA in 1941). The struggle for the control of energy resources is still ongoing.

In addition to colonialism, two world wars and the chess game between superpowers for influence in the Middle East, the 20th century was characterised by the oil

crisis of 1973. This date is widely recognised as the starting point of worldwide interest in alternative energy resources, since for generation of electricity and for fuel production it was almost exclusively used crude oil.[2,3] For this reason, the exploitation of renewable energy sources has become one of the greatest challenges of the current century: among them solar energy, which is potentially clean, safe and unlimited and could be converted into electricity by photoelectric effect or in other energy sources, is the most important one.

In this context, hydrogen production arises as the most promising candidate to substitute crude oil. As we will see in the next chapter, there are several industrial methods suitable for hydrogen production, but currently the most challenging one is water splitting, a general term used to describe a chemical reaction in which water is separated into oxygen and hydrogen. Looking more in detail, the most convenient way to perform water splitting is through photoelectrocatalysis, which is recognised by the huge, increasing number of scientific publications concerning this topic.

1.1 – Thesis outline and experimental plan

This work was structured to provide useful results for technological advance in the field of photoelectrocatalytic water splitting. In chapter 2, an introduction on water splitting is presented, with insight on the state-of-the-art literature and the declaration of the aim of the thesis. In chapter 3, the fabrication and characterisation methods that have been used in the experimental part of this project are described. In chapter 4, the experimental results obtained in the three years available for this research are presented and discussed. In chapter 5, conclusions are drawn on the basis of the experimental results, with a farsighted look on future perspectives. References are presented at the end of each chapter for an easier consultation.

Table 1.1 shows the timeline of the Ph.D. project schedule in these three years.

Table 1.1 - Timeline of the Ph.D. project schedule.

1st YEAR	Study of SICM technique and its applications; creation and characterisation of a coupled SICM-EC probe
2nd YEAR	First approaches to water splitting through bibliographic study and preliminary experiments; local quantitative H_2 and O_2 detection; first experiments on OCP sensing
3rd YEAR	Design, preparation and characterisation of microstructured electrodes; pH sensing on photoelectrocatalysts during water splitting; study on integration of microelectrodes in a microfluidic system; design of the integrated microfluidic chip; fluid dynamics simulations

Bibliography

1. Staudinger, H. Über Polymerisation. *Berichte der Dtsch. Chem. Gesellschaft* **53,** 1073–1085 (1920).

2. Bastos, M. B. Brazil's Ethanol Program-An Insider's View. *Energy Tribune* (2007).

3. Betz, K. W. Remembering the Energy Crisis. *Energy User News* 4–6 (1998).

2 – Introduction on water splitting

2.1 – Energetic scenery

It is well know that there is a continuous increasing in energy demand at global scale, from developing countries and BRICS (Brazil, Russia, India, China, South Africa) as well as from more industrialized countries, due to both growing world population and lifestyle standards. Nowadays, it is estimated that about 90 % of total energy is provided by fossil fuels:[1] this massive use implies obvious environmental drawbacks, beside their implicit nature of non-renewable resources that necessarily involves research on other sources of energy in a relatively short-term scale to satisfy consumptions. One of the greatest challenges of 21st century is surely the exploitation of renewable energy resources, for its advantages in economy, environment and society.

The main renewable resources that are currently employed are wind, geothermal, hydropower and solar: they are undoubtedly cleaner and more sustainable with respect to coke, petroleum and natural gas, but each of these alternative energy sources has its peculiar limitation, most of them correlated to energy storage and discontinuous supply that makes this task more challenging. From the list above, solar energy seems to be the most favourable one since it is unlimited, renewable and free and it is used to produce both electricity and heat, but it is important to consider its disadvantages: sunlight is an intermittent source of energy and irradiation depends on geographical position, day, time and season; moreover, it has a low density per unit of Earth surface.[2] For this reason, recent research moved on a different topic. Hydrogen is the most promising fuel, since it is abundant from many sustainable and renewable resources (e.g. biomass or water: the process of "breaking" water into oxygen and hydrogen is called water splitting), has good energy conversion effectiveness, is environmentally friendly, can be transported over long distances, has high Higher Heating Value and Low Heating Value compared with many traditional fossil fuels and has a high storage capability with different options (e.g. in gas or liquid form, or absorbed in metal hydrides):[1] for these reasons, it is currently considered as a valuable carbon-free solution.

Next paragraph will describe in detail the current hydrogen production methods and future perspectives on their commercial applications.

2.2 – Principal hydrogen production technologies

To date, around 50% of the global hydrogen demand is met by natural gas steam reforming, making it the most commonly used process even if it has heavy greenhouse gases emissions as a consequence. The rest of hydrogen production is provided by oil reforming (30%), coal gasification (18%), water electrolysis (3.9%) and other sources (0.1%).[3] Since one of the main task of hydrogen-involving projects is to eliminate, or at least reduce, the harmful effects of fossil fuels, the target should be to produce hydrogen from clean and abundant sources: focusing on sustainable energy solution, most of the hydrogen production methods are still being developed for commercial application, such as thermochemical, thermoelectrochemical, photocatalytic, photochemical and photoelectrochemical; the only method that is commercially available is conventional electrolysis, as seen in the list above.

	Source		Brief description
	Primary energy	Material	
Electrolysis	Electrical	Water	Direct current is used to split water into O_2 and H_2 (electrochemical reaction)
Plasma arc decomposition		Fossil fuels	Cleaned natural gas pass through plasma arc to generate H_2 and carbon soot
Thermolysis	Thermal	Water	Thermal decomposition of water (steam) at temperatures over 2500 K
Thermochemical processes Water splitting		Water	Cyclical reactions (net reaction: water splitting into H_2 and O_2)
Biomass conversion		Biomass	Thermocatalytic conversion
Gasification			Conversion of biomass into syngas
Reforming			Conversion of liquid biomass (biofuels) into H_2
PV electrolysis	Photonic	Water	PV panels are used to generate electricity
Photocatalysis			Water is split into H_2 and O_2 by using the electron–hole pair generated by the photocatalyst
Photoelectrochemical			A hybrid cell simultaneously produces current and voltage upon absorption of light
Dark fermentation	Biochemical	Biomass	Biological systems to generate H_2 in the absence of light
High temperature electrolysis	Electrical + thermal	Water	Electrical and thermal energy are used together to drive water splitting at high temperatures
Hybrid thermochemical cycles			Electrical and thermal energy are used together to drive cyclical chemical reactions
Coal gasification			Conversion of coal into syngas
Fossil fuel reforming			Fossil fuels are converted to H_2 and CO_2
Biophotolysis	Photonic + biochemical	Biomass + water	Biological systems (microbes etc.) used to generate H_2
Photofermentation			Fermentation process activated by exposure to light
Artificial photosynthesis			Artificial systems mimic photosynthesis to generate H_2
Photoelectrolysis	Electrical + photonic	Water	Photoelectrodes and external electricity are used to drive water electrolysis

Figure 2.1 - Overview of H_2 production methods by primary energy and material sources.[1]

There are several ways to produce clean energy for electrolitical water splitting, from solar, geothermal, biomass, wind, ocean/tides to recycled energy from industrial processes and nuclear and thermal power plant.[1] The reaction that occurs in this process is the following:

$$2H_2O_{(l)} \rightarrow 2H_{2(g)} + O_2;\ E_0 = -1.229\ V$$

For water thermolysis, the reaction is:

$$H_2O \xrightarrow{heat} H_2 + \frac{1}{2}O_2$$

In order to obtain a reasonable degree of dissociation, this reaction requires temperatures above 2500 K.[1]

Thermochemical hydrogen production includes all processes that are essentially driven by heat, in particular thermochemical cycles like S-I, Cu-Cl and Mg-Cl. The main advantage of this method is no requirement of catalyst to drive or support any of the steps of the chemical reaction: moreover, there is no need of membranes to separate hydrogen and oxygen, the temperatures required are between 600 and 1200 K and the requirement of electrical energy is none or very low.[1] However, because of the relatively high reaction temperature requirements of these cycles, there are not many sustainable thermal energy sources available to drive the individual reactions in the cycle. Nuclear, concentrated solar, and biomass combustion heat can be listed as possible sustainable thermal energy sources to drive the reactions.

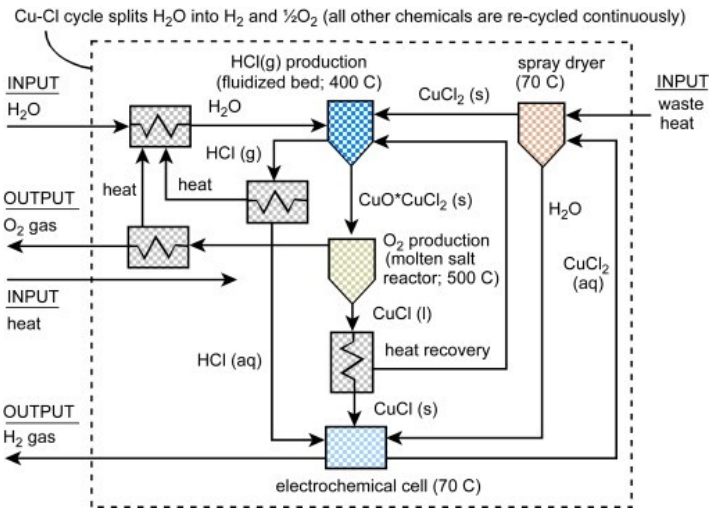

Figure 2.2 - Schematic of the Cu-Cl thermochemical cycle.[4]

Other hydrogen production methods include dark fermentation, the conversion of biochemical energy to hydrogen with microorganisms in absence of light and high-temperature electrolysis, where steam is dissociated to hydrogen and oxygen at temperatures between 700 and 1000 °C.[1] In particular, the last technology is generally considered more efficient than conventional room temperature electrolysis since efficiency increases with increasing temperature. In this system, water is converted to steam by using thermal energy. The system components are heated either directly by the steam supply or indirectly by heat transfer and the electrical energy demand is lower than that of conventional electrolysis methods.[3] Another advantage: the use of a clean heat source (i.e. solar, geothermal, and/or nuclear) as external heat source may lead to achieving zero greenhouse gas emissions. However, the system components have to meet specific requirements for an efficient hydrogen generation due to high operating temperatures.[3]

Coming to technologies that involve directly sunlight, photocatalysis uses photonic energy converting it to chemical energy splitting water into oxygen and hydrogen. The mechanism is well known: when the photocatalyst (a semiconductor) is hit by a photon with a certain energy, not less that the band gap, there is the formation of excitons, so an electron in the valence band (VB) of semiconductor can be excited into the conduction band (CB) absorbing the energy of this photon and subsequently a hole is also produced in the VB. Due to the presence of band gap, the photogenerated h^+/e^- pairs can migrate to the surface of the semiconductor before recombination where they are utilized to dissociate water. A semiconductor must satisfy a few requirements to be considered as a possible photocatalyst: the highest level of the VB should be more positive than water oxidation level (E_{O_2/H_2O}, 1.23 V vs normal hydrogen electrode, NHE); the lowest level of the CB should be more negative than the hydrogen evolution potential (E_{H_2/H_2O}, 0 V vs NHE); band gap must have a minimum value, as seen from the semireactions that occur at the surface:[2]

$$H_2O + 2h^+ \rightarrow 2H^+ + \frac{1}{2}O_2 \qquad E^0_{oxidation} = -1.23\ V$$

$$2H^+ + 2e^- \rightarrow H_2 \qquad E^0_{reduction} = 0.00\ V$$

$$H_2O \rightarrow H_2 + \frac{1}{2}O_2$$

From these semireactions (photogenerated holes and electrons are represented with h^+ and e^-) it is possible to state that a semiconductor eligible as photocatalyst for water splitting must have a band gap at least of 1.23 eV. In addition, kinetic overpotentials and losses typically push required value to around 2 eV.[5]

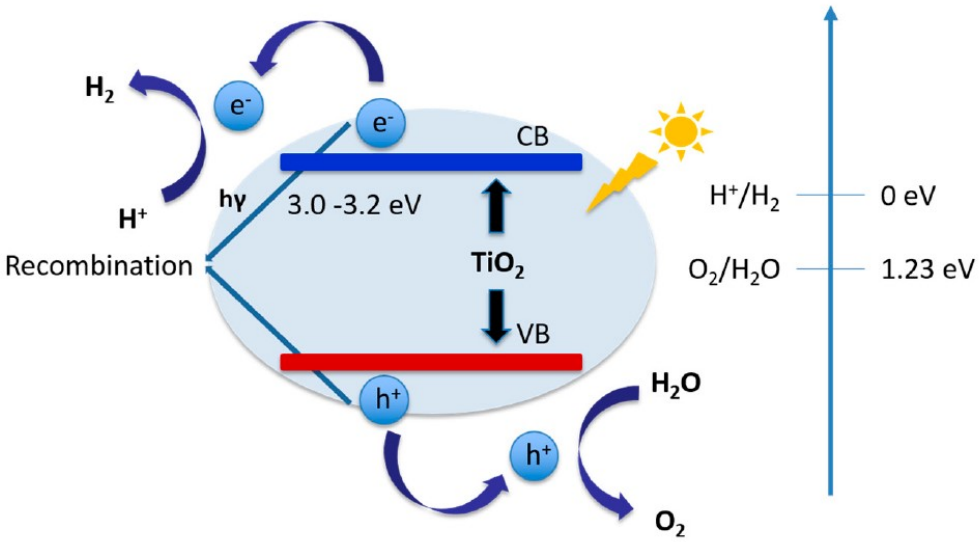

Figure 2.3 - Schematic band gap diagram of TiO_2.[2]

While in photocatalysis oxidation and reduction are both performed on the surface of the photocatalyst, in photoelectrocatalytic water splitting an additional potential bias, provided by a photovoltaic element, is applied to photocatalyst electrodes: in this way, e^- promoted to the CB of photocatalyst are driven to the counter electrode via the external circuit by applied bias potential, thus leaving h^+ on the surface of the semiconductor and suppressing recombination of electron/hole pairs since they react with water at two spatially separated electrodes.

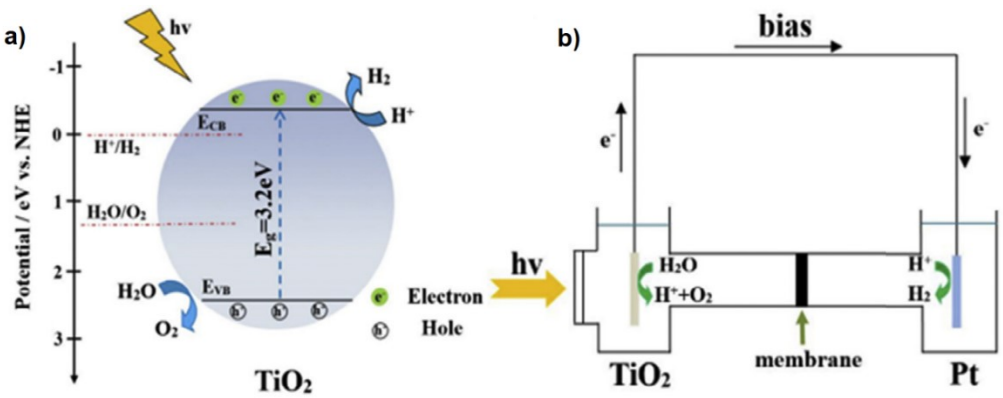

Figure 2.4 - Schematic diagram of a) photocatalitic and b) photoelectrocatalytic water splitting on TiO2. Adapted from ref. 5.

Since the latest methods presented here are hot topics on energy and hydrogen research, assumption supported by the continuously increasing amounts of scientific papers,[6] it is of interest to deepen the knowledge in this field by discussing the materials used to drive photocatalytic water splitting.

2.3 – Materials used in photoelectrocatalysis

As stated in the previous paragraph, an efficient photocatalyst for water splitting must satisfy the following requirements: relatively small band gap for visible light absorption; proper position of CB and VB at the surface to straddle the HER and OER potentials; high stability under sunlight irradiation in acidic/basic aqueous; a facile and efficient charge transfer from the surface of catalyst to the solution; low overpotentials for the oxidation/reduction of water.[7] To date, no cost-effective material satisfies these technical requirements for practical hydrogen production, each material having its own plus and drawbacks[8] Therefore, to accomplish a full knowledge on water splitting process, the main materials used and their intrinsic characteristics are examined.

Looking at the requirements listed above for operational water splitting, the first "material group" that comes into mind are the semiconductors: in fact, the first experiment on electrochemical photolysis of water ever, the well-known work by Fujishima and Honda in 1972,[9] involves TiO_2 as photocatalyst. Starting from this pioneering study, many authors focused their research on this semiconductor for photocatalytic application due to its abundance, chemical stability, low cost, relatively low toxicity, superior photostability and high intrinsic catalytic activity under UV illumination. However, titania has a large band gap (3.2/3.0 eV for anatase/rutile) that causes an inability to harvest visible light (its band gap covers only 5 % of the solar spectrum); moreover, its low electron mobility and short hole diffusion length (10-100 nm) are the causes of fast charge carrier recombination, which results in the release of unproductive energy like heat or photons.[2,8]

Other than TiO_2, other examples of metal oxides (such as Fe_2O_3, WO_3, ZnO, Cu_2O, Al_2O_3, Ga_2O_3, Ta_2O_5, CoO, ZrO_2)[10-14] have been widely studied for their stability in aqueous media and their low cost, but the largest part of metal oxides have a

large band gap that limits their ability to absorb visible light (as titania). Looking at the VB and CB in a common metal oxide, O has 2p electronic configuration while metal has s, that is translated in a large band gap for relatively ionic-bonded materials such as ZnO (3.4 eV), Ga_2O_3 (4.5 eV), Al_2O_3 (8.8 eV): changing metal to a transition one with d^n electronic configurations, like Fe_2O_3 (2.0 eV), Co_3O_4 (4.5 eV)[15] shows increased light absorption but lack efficient charge carrier transfer due to small polaron-dominated conductivity and associated high resistivity; the use of post-transition metals like in PbO (2.1 eV), SnO (2.4 eV), Bi_2O_3 (2.5 eV)[10,16] leads to better photogeneration of charge carriers that are however extracted less efficiently;[2,12] lastly, ternary metal oxide compounds like $BiVO_4$ (2.4 eV)[13] have both low band gap and reasonable band edge alignment for the water redox potentials. A big issue in typical metal oxides, however, is their attitude towards photocorrosion, in particular for ZnO:[2] this happens when the anion from the catalyst itself is oxidized by photogenerated holes instead of water.

Another class of semiconductors renowned for their potential role in photocatalytic water splitting are metal sulphides. CdS and ZnS are the most studied metal sulphides photocatalysts:[2,17] CdS in particular has a narrower band gap (2.4 eV)[18] compared to the average metal oxide and it is considered a promising material for visible light-driven water photocatalysis; however, this sulphide has low hydrogen production rates due to rapid recombination of photogenerated charge carriers. On the opposite, ZnS has a wide band gap (3.6 eV) and responds weakly to visible light.

In addition, nitrides and oxynitrides can as well be applied as photocatalysts in order to harvest solar light for water splitting. The 2p orbitals of nitrogen have higher energy than their correspondents of oxygen in metal oxides, therefore nitrides need a lower energy to excite electrons to CB. Some examples in recent literature include GaN, Ta_3N_5 and g-C_3N_4 (graphitic carbon nitrides).[2]

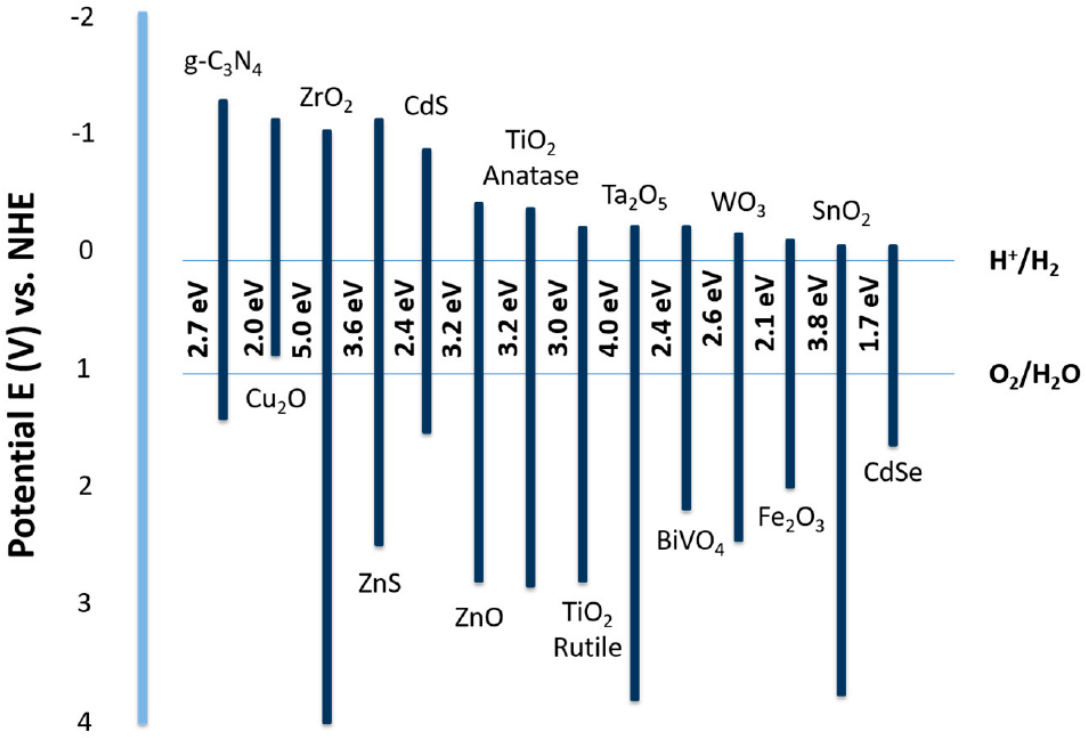

Figure 2.5 - Band structure illustration of various semiconductors, with respect of the redox potential of water splitting.[2]

As we have seen above, many research groups worldwide invested a lot in study and application of different kinds of semiconductors as photocatalysts, although each advantage of a material comes along with a specific drawback: metal oxides, sulphides and nitrides have a significantly lower band gap than that of TiO_2, however, unlike titania, they suffer from photocorrosion.[2] Recent research spent a great effort on reduce, if not eliminate at all, some of these disadvantages with different surface modification strategies aimed to tailor the properties of the materials listed above.

2.4 – How to improve efficiency of photocatalysts

We have already mentioned the condition a material should meet to be considered an ideal photocatalyst. In order to achieve these goals, research focused on tuning the electronic properties of semiconductors used for water splitting. Recent progress on strategies for enhancing photocatalyst performance include: multiple semiconductor system; doping; integration of electrocatalysts; nanostructural effects.

With the first methodology, different semiconductors are integrated and employed as photoelectrodes, so that they are responsive to a broader portion of the solar spectrum and the use of photonic energy is optimized. The formation of a semiconductor/semiconductor heterojunction can decrease the charge recombination rate by yielding long-lived h^+/e^- pairs:[2,19] this junction could be n-n or p-n, since a proper band alignment allows charge transfer from one semiconductor to the other.[20] There are several examples of this kind of coupling in literature, in particular with the aim to increase the spectral range of application of TiO_2; authors reported titania heterojunctions featuring $BiVO_4$,[2] CdS,[7] Cu_2O[21] among the most important. Anyway, multicomponent metal oxides have been developed as well, especially tailored for those having a large band gap: CuO/ZnO,[22] CdS/ZnO,[23] $WO_3/BiVO_4$,[24,25] Cu_2O/CuO[26] and many others.

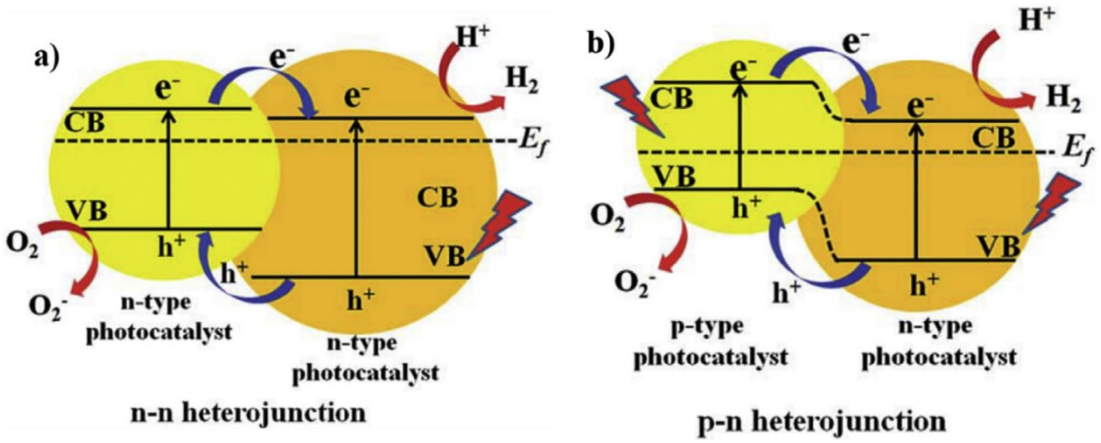

Figure 2.6 - Schematic diagram of charge transfer in a photocatalytic system with a) n-n heterojunction and b) p-n heterojunction.[5]

Material doping is a surface modification technique that bears huge advantages: improves the conductivity of the semiconductor; "engineers" the band gap of the semiconductor and enhances its optical absorption; increases extrinsic charge carrier density and increases the diffusion length of minority carrier. It is important to point out that doping is not a miraculous tool for surface scientists: certain levels of doping are critical for water splitting applications since it may introduce mid-gap bulk or surface states, reducing the energy barrier and inducing a new optical absorption edge.[2] In TiO_2, bulk doping can occur with metal and non-metal elements, replacing Ti (cation) and O (anion): consequently, doping sensitizes titania to visible light as well as suppresses recombination of charge carriers. Scientific literature reports doping of TiO_2 with N, C, B, S, F, Cl and P[27,28] as substitutes for O, while metal cations as Fe, Cu, V,

Co, Ni, Cr and Mn are used to replace Ti.[5,29,30] The other classes of semiconductors for photocatalysis can also benefit from doping (e.g. Si- doped Fe_2O_3).[7] Lastly, a mention is needed for doping with carbon, for example with carbon nanotubes, to extend photocatalytic activity to visible light:[31] although different mechanisms have been proposed to explain this effect, the mechanism of synergic effect of carbon remains unclear.[2]

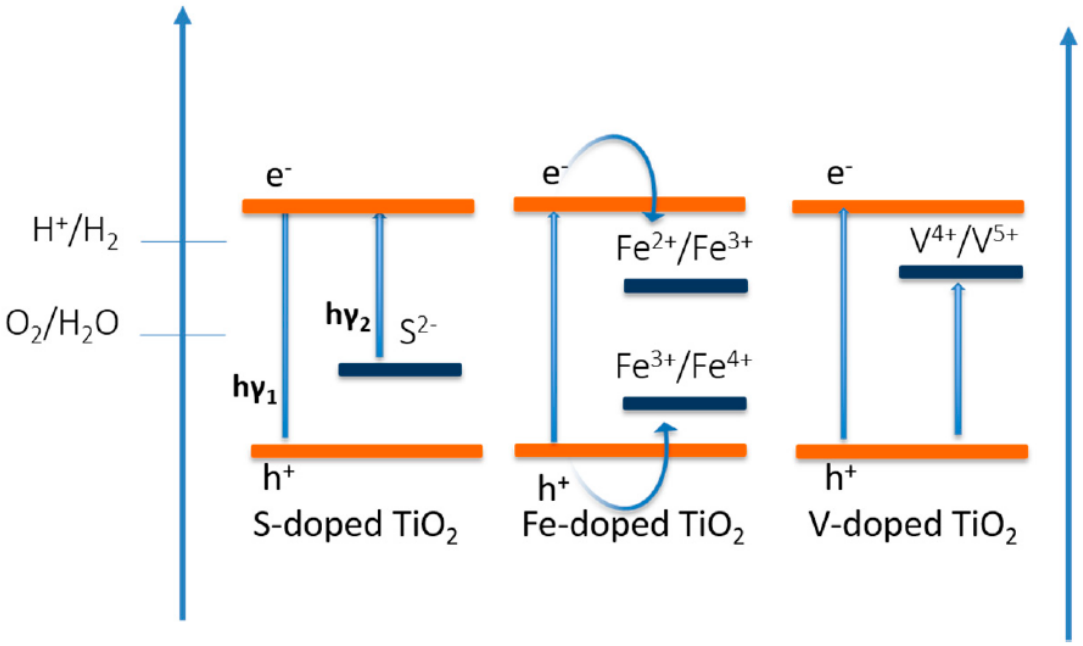

Figure 2.7 - Schematic band gap alignment of S-doped, Fe-doped and V-doped TiO_2.[2]

Integration of electrocatalysts is a strategy meant to reduce the overpotentials for HER and OER by deposition of particles of this material on the surface of a chosen semiconductor, therefore improving solar driven water splitting by prohibit the energy decreasing backward reaction: we can then talk of deposition of a co-catalyst. As suitable co-catalysts, RuO_2, NiO, Au, Pt, Pd and IrO_2[32,33] can be used: they have been reported to trap photogenerated electrons due to their significant role as electron sinks.[2] Among noble metals, Au has been elected the preferred co-catalyst for photocatalytic hydrogen production due to its high affinity towards photogenerated electrons, high resistance to oxidation and less activity towards side reactions.[2] It is necessary to consider, however, that the high cost of precious metals hinders their practical application.

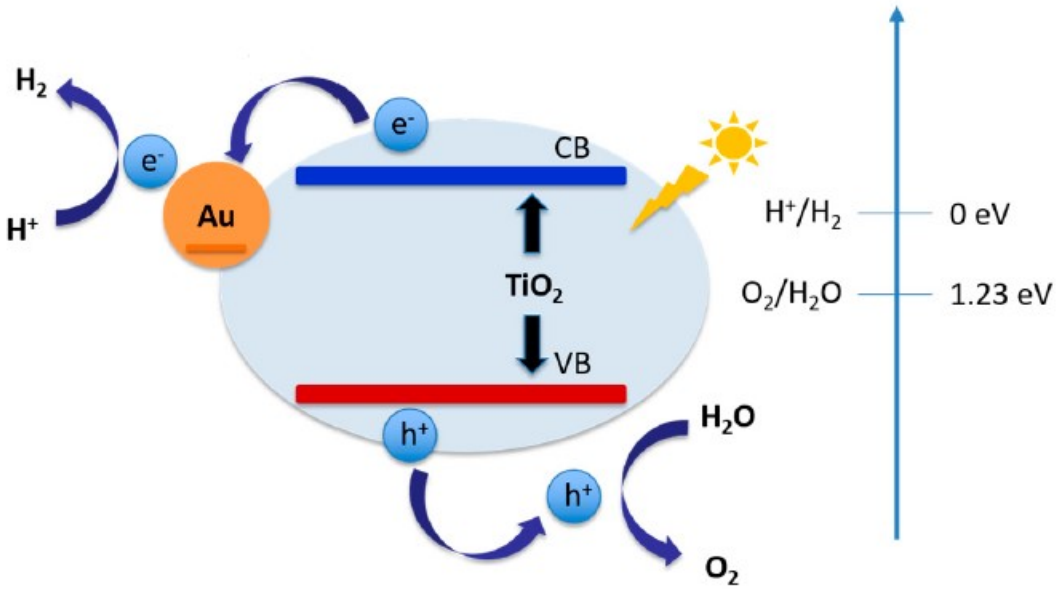

Figure 2.8 - Schematic illustration of heterojunction between Au nanoparticles and TiO_2 semiconductors. Adapted from ref. 2.

The implementation of nanostructured semiconductors with high surface area increases interactive sites at semiconductor/electrolyte interface, also enhancing charge transfer kinetics. Recently, one-dimensional, two-dimensional and three-dimensional hierarchical structures have demonstrated all these characteristics along with improved h^+/e^- separation, leading to improvement in the photocatalytic activity. This set of advantages derives from the decoupling of light absorption and charge carrier collection, together with shortening of diffusion path lengths for photogenerated charge carriers.[7] There are some examples of state-of-the-art nanostructured photocatalysts, including WO_3, $BiVO_4$, Fe_2O_3, Si, Cu_2O and C_3N_4[7] and looking in detail to the "classical" photocatalyst TiO_2 literature studies report photocatalytic application of nanotubes, nanowires, nanorods, nanosheets etc., synthesized via hydrothermal methods, solvothermal methods, sol-gel methods, template methods, electrospinning and electrochemical anodic oxidation.[5,34,35,36]

We have so far presented a brief overview on how H_2 is generated, what is the best method so far known to produce it and the characteristics of the materials used in the photoelectrocatalytic method. What has not been discussed yet is the techniques used to study the water splitting reactions: this will be the topic of the next paragraph.

2.5 – *In situ* sensing techniques

The main way to evaluate the efficiency of a photoelectrochemical cell is to measure quantitatively the products of the water splitting reaction. It is quite intuitive to find a solution to this task in gas chromatography-mass spectrometry: this method is very useful considering the incident light, so to have a measure of efficiency of the cell, but it gives little (if none) information on what happens at local scale. Data on these phenomena would be extremely useful, particularly if the device involves nanostructured semiconductors since semiconductor-electrolyte interface plays a very important role in shaping interfacial recombination, charge carrier transport and reaction pathways. *In situ* techniques useful for this goal should provide high spatial and temporal resolution for analysis of charge dynamics and reaction intermediates, while analysing electrodical surfaces and interfaces under operating conditions. These methods can be divided in spectroscopic and scanning-probe measurements (SPM).[37]

Spectroscopic methods are meant to give useful information about kinetics, phenomenological rate constants, recombination, trapping and lifetime of charge carriers. Developing a new generation of *in situ* techniques for studying photoelectrochemical water splitting presents a formidable challenge and only recently authors tried to study in deep this topic. Currently known spectroscopic techniques include: electrochemical impedance spectroscopy, used to study the effect of charge carrier transport, distribution and recombination in photoelectrodes, along with the nature of the electrochemical capacitance;[38,39] intensity modulated photocurrent spectroscopy, which analyses the dynamics of the charge-transport processes in dye-sensitized solar cells;[40] transient absorption spectroscopy, a pump-probe technique that is based on excitation of electrons in VB while measuring the transient absorption in the mid-IR and NIR regions;[a,41] X-ray absorption fine-structure, to understand charge transfer between photoelectrode and co-catalyst and the structures and active sites of co-catalyst in working conditions.[42] Other methods include synchrotron- based X-ray techniques, like X-ray reflectivity.[37]

[a] It is possible to measure the lifetime of holes by using visible light, the techniques is therefore called Photoinduced Absorption Spectroscopy.[63]

All the spectroscopic *in situ* techniques listed above are related to kinetics and mechanism of charge carriers, but no information is provided on the products of water splitting reaction: there is one exception, *in situ* infrared spectroscopy, useful for determination of reaction intermediates, but it is very challenging due to a strong IR absorption by the water molecules.[43] The answer to this task comes from SPM techniques, utilizing a probe scanning the surface of a sample and recording the interactions between the probe and the surface as a function of the probe position. The most representative example of this category is the Scanning Electro-Chemical Microscope (SECM), where an ultramicroelectrode (UME) works as an electrochemical probe to scan a photoelectrode under operating conditions: during the measurement, H_2 (O_2) generated at the photocathode (photoanode) is oxidised (reduced) at the UME and the corresponding current is recorded; this technique is therefore extremely useful in mapping the variation of gas evolution across the photoelectrode surface.[44]

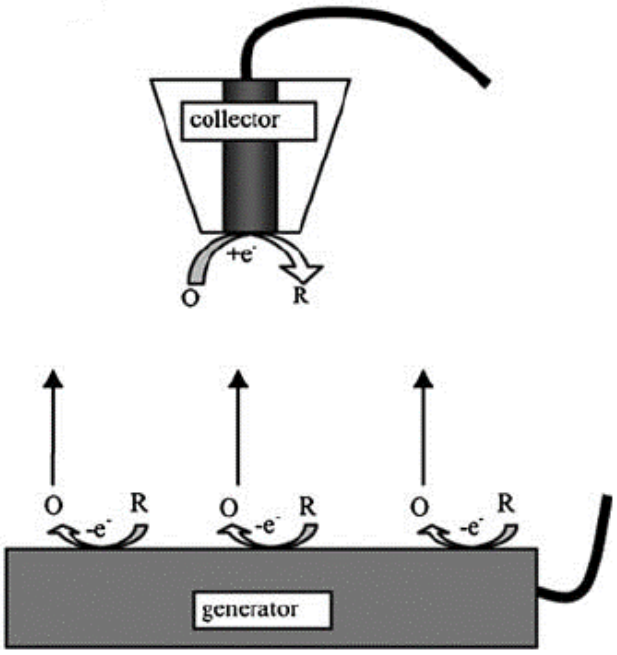

Figure 2.9 - Schematic of SECM operation. Adapted from ref. 45.

This last analytical instrument is indeed promising and has the required features to be set as a standard method for investigation on photoelectrocatalytic surfaces, thanks to the possibility of quantitative analysis of electrochemically active species and its high spatial resolution. In the next chapter the operative principle of SECM (and SICM) will be discussed further in detail: for now, the described characteristics are sufficient to introduce and justify the experimental work of this thesis.

2.6 – Motivations of the thesis

Looking at the semireactions that describe electrolysis, it is spontaneous to think that consumption and production of H^+ ions will modify the pH of the solution, at least at local scale: the surroundings of the photoelectrode will therefore experience the formation of a pH gradient. Formation of pH gradients at electrodes is a critical issue in hydrogen production, as well as in many electrochemical surface processes. Some examples of how this phenomenon can affect interfacial reactions that requires a precise pH control can be found in metal/semiconductor depositions, corrosions, etc.;[21,46] moreover, the formation of pH gradients at electrodes' surface is the cause of ohmic losses as well, thus leading to an efficiency drop of electrochemical cell (e.g. fuel cells).[47]

In the last years, many authors reported on the creation of devices useful for pH measurement at local scale, for different applications: among them, liquid ion-selective sensors,[48] conducting polymer-coated cantilevers,[49] gold nanoshell,[50] polymer microcapsules,[51] parylene-insulated iridium nanoelectrodes,[52] field-effect nanowire transistors[53] and fiber-optic[54] are remarkable as pioneering tools in this field of analysis. More recently, scientific research focused on the use of electrochemical scanning probe techniques, like SECM and scanning ion conductance microscopy (SICM),[55] employing double-function probes for simultaneous topographical imaging and pH mapping: these integrated designs provide a method to control the position of the electrode in the XYZ space and allows local pH measurement. Since the limitations of SECM are most commonly addressed by adopting constant-distance mode imaging schemes, in which the tip-sample spacing is maintained independently of the redox current,[56] many authors decided to switch their research interest to SICM-based integrated devices that provides a feedback signal for distance control, allowing to scan intricate surface properties and to measure pH with high spatial resolution thanks to the use of focused ion beam (FIB) technique.[57-62] These methods have a common drawback that is the cost of the single probe: the procedure is complex and increases the overall cost of a single pipette.

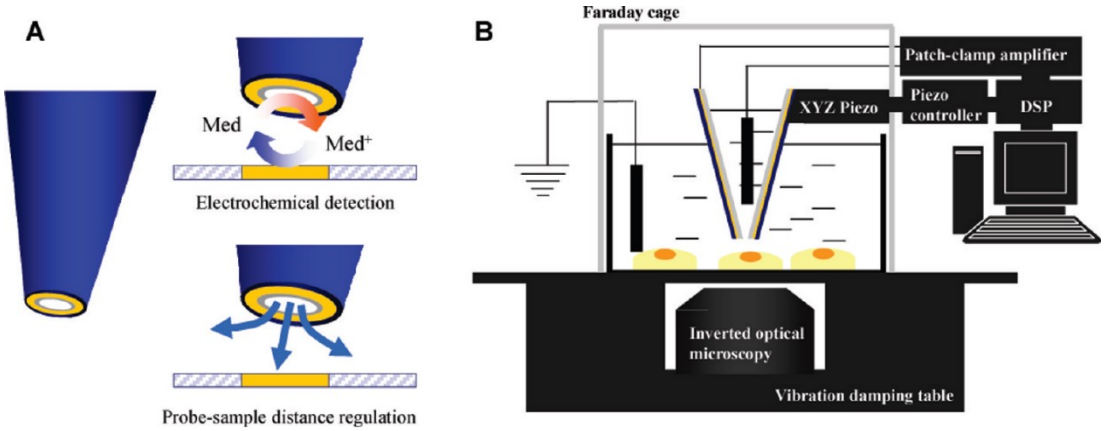

Figure 2.10 - Schematic illustration of a) the SECM/SICM system probe and b) the SECM/SICM setup.[60]

For this reason, the main aim of this thesis is to create a different coupled sensing electrode, with new electrodic material and insulating coating easily realised, suitable for both localized pH sensing and quantitative measurement of chemical species at local scale. In particular, attention is focused on pH detection over microstructured catalysts during water splitting process. In the next chapters, we will deepen the characteristics and the operative conditions of the technique used and of the methods for analysis and characterisation; then, the experimental part will describe the design of experiments, the conditions in which they have been performed and the results we obtained. The final part of this thesis contains the conclusions we can get from the results obtained and a brief discussion on the future perspectives of this work, focused towards the development of water splitting process into microfluidic systems.

Bibliography

1. Acar, C., Dincer, I. & Naterer, G. F. Review of photocatalytic water-splitting methods for sustainable hydrogen production. *Int. J. Energy Res.* **40,** 1449–1473 (2016).

2. Jafari, T. *et al.* Photocatalytic Water Splitting—The Untamed Dream: A Review of Recent Advances. *Molecules* **21,** 900 (2016).

3. Dincer, I. & Acar, C. Review and evaluation of hydrogen production methods for better sustainability. *Int. J. Hydrogen Energy* **40,** 11094–11111 (2014).

4. Naterer, G. *et al.* Recent Canadian advances in nuclear-based hydrogen production and the thermochemical Cu–Cl cycle. *Int. J. Hydrogen Energy* **34,** 2901–2917 (2009).

5. Ge, M. *et al.* A review of TiO_2 nanostructured catalysts for sustainable H_2 generation. *Int. J. Hydrogen Energy* **42,** 8418–8449 (2017).

6. Li, Y., Li, Y.-L., Sa, B. & Ahuja, R. Review of two-dimensional materials for photocatalytic water splitting from a theoretical perspective. *Catal. Sci. Technol.* **7,** 545–559 (2017).

7. Chen, S., Thind, S. S. & Chen, A. Nanostructured materials for water splitting - state of the art and future needs: A mini-review. *Electrochem. commun.* **63,** 10–17 (2016).

8. Chandrasekaran, S., Chung, J. S., Kim, E. J. & Hur, S. H. Advanced Nano-Structured Materials for Photocatalytic Water Splitting. *J. Electrochem. Sci. Technol.* **7,** 1–12 (2016).

9. Fujishima, A. & Honda, K. Electrochemical Photolysis of Water at a Semiconductor Electrode. *Nature* **238,** 37–38 (1972).

10. Madelung, O. *Semiconductors: data handbook*. (Springer Science & Business Media, 2012).

11. Schmitz, G., Gassmann, P. & Franchy, R. A combined scanning tunneling microscopy and electron energy loss spectroscopy study on the formation of thin, well-ordered β-Ga_2O_3 films on CoGa(001). *J. Appl. Phys.* **83,** 2533–2538 (1998).

12. Perevalov, T. V. *et al.* Electronic structure of α-Al_2O_3: Ab initio simulations and comparison with experiment. *JETP Lett.* **85,** 165–168 (2007).

13. Walsh, A., Yan, Y., Huda, M. N., Al-Jassim, M. M. & Wei, S.-H. Band Edge Electronic Structure of BiVO4 : Elucidating the Role of the Bi s and V d Orbitals. *Chem. Mater.* **21,** 547–551 (2009).

14. Cornell, R. M. & Schwertmann, U. *The iron oxides: structure, properties,*

reactions, occurrences and uses. (John Wiley & Sons, 2003).

15. Kim, K. J. & Park, Y. R. Optical investigation of charge-transfer transitions in spinel Co_3O_4. *Solid State Commun.* **127,** 25–28 (2003).

16. Walsh, A. & Watson, G. W. Electronic structures of rocksalt, litharge, and herzenbergite SnO by density functional theory. *Phys. Rev. B* **70,** 235114 (2004).

17. Ismail, A. A. & Bahnemann, D. W. Photochemical splitting of water for hydrogen production by photocatalysis: A review. *Sol. Energy Mater. Sol. Cells* **128,** 85–101 (2014).

18. Ahmad, H., Kamarudin, S. K., Minggu, L. J. & Kassim, M. Hydrogen from photo-catalytic water splitting process: A review. *Renew. Sustain. Energy Rev.* **43,** 599–610 (2015).

19. Maeda, K. Z-Scheme Water Splitting Using Two Different Semiconductor Photocatalysts. *ACS Catal.* **3,** 1486–1503 (2013).

20. Reza Gholipour, M., Dinh, C.-T., Béland, F. & Do, T.-O. Nanocomposite heterojunctions as sunlight-driven photocatalysts for hydrogen production from water splitting. *Nanoscale* **7,** 8187–8208 (2015).

21. Zanatta, M. *et al.* Cu_2O/TiO_2 heterostructures on a DVD as easy&cheap photoelectrochemical sensors. *Thin Solid Films* **603,** 193–201 (2016).

22. Paz, D. S. *et al.* CuO/ZnO coupled oxide films obtained by the electrodeposition technique and their photocatalytic activity in phenol degradation under solar irradiation. *Water Sci. Technol.* **68,** 1031 (2013).

23. Wang, X., Liu, G., Lu, G. Q. & Cheng, H.-M. Stable photocatalytic hydrogen evolution from water over ZnO–CdS core–shell nanorods. *Int. J. Hydrogen Energy* **35,** 8199–8205 (2010).

24. Su, J., Guo, L., Bao, N. & Grimes, C. A. Nanostructured $WO_3/BiVO_4$ Heterojunction Films for Efficient Photoelectrochemical Water Splitting. *Nano Lett.* **11,** 1928–1933 (2011).

25. Pihosh, Y. *et al.* Photocatalytic generation of hydrogen by core-shell $WO_3/BiVO_4$ nanorods with ultimate water splitting efficiency. *Sci. Rep.* **5,** 11141 (2015).

26. Dubale, A. A. *et al.* Heterostructured Cu_2O/CuO decorated with nickel as a highly efficient photocathode for photoelectrochemical water reduction. *J. Mater. Chem. A* **3,** 12482–12499 (2015).

27. Tang, J., Cowan, A. J., Durrant, J. R. & Klug, D. R. Mechanism of O_2 Production from Water Splitting: Nature of Charge Carriers in Nitrogen Doped Nanocrystalline TiO_2 Films and Factors Limiting O2 Production. *J. Phys. Chem. C* **115,** 3143–3150 (2011).

28. Piskunov, S. *et al.* C-, N-, S-, and Fe-Doped TiO_2 and $SrTiO_3$ Nanotubes for Visible-Light-Driven Photocatalytic Water Splitting: Prediction from First Principles. *J. Phys. Chem. C* **119,** 18686–18696 (2015).

29. Jung, M. *et al.* Exploring Cu oxidation state on TiO_2 and its transformation during photocatalytic hydrogen evolution. *Appl. Catal. A Gen.* **521,** 190–201 (2016).

30. Tobaldi, D. M. *et al.* Effects of Cu, Zn and Cu-Zn addition on the microstructure and antibacterial and photocatalytic functional properties of Cu-Zn modified TiO_2 nano-heterostructures. *J. Photochem. Photobiol. A Chem.* **330,** 44–54 (2016).

31. Wang, H., Dong, S., Chang, Y. & Faria, J. L. Enhancing the photocatalytic properties of TiO_2 by coupling with carbon nanotubes and supporting gold. *J. Hazard. Mater.* **235–236,** 230–236 (2012).

32. Majeed, I. *et al.* On the role of metal particle size and surface coverage for photo-catalytic hydrogen production: A case study of the Au/CdS system. *Appl. Catal. B Environ.* **182,** 266–276 (2016).

33. Sreethawong, T. & Yoshikawa, S. Comparative investigation on photocatalytic hydrogen evolution over Cu-, Pd-, and Au-loaded mesoporous TiO_2 photocatalysts. *Catal. Commun.* **6,** 661–668 (2005).

34. Haider, Z. & Kang, Y. S. Facile Preparation of Hierarchical TiO_2 Nano Structures: Growth Mechanism and Enhanced Photocatalytic H_2 Production from Water Splitting Using Methanol as a Sacrificial Reagent. *ACS Appl. Mater. Interfaces* **6,** 10342–10352 (2014).

35. Tang, Y. *et al.* Ultrafast Synthesis of Layered Titanate Microspherulite Particles by Electrochemical Spark Discharge Spallation. *Chem. - A Eur. J.* **16,** 7704–7708 (2010).

36. Naik, B., Moon, S. Y., Kim, S. H. & Park, J. Y. Enhanced photocatalytic generation of hydrogen by Pt-deposited nitrogen-doped TiO_2 hierarchical nanostructures. *Appl. Surf. Sci.* **354,** 347–352 (2015).

37. Cen, J., Wu, Q., Liu, M. & Orlov, A. Developing new understanding of photoelectrochemical water splitting via in-situ techniques: A review on recent progress. *Green Energy Environ.* **2,** 100–111 (2017).

38. Klahr, B., Gimenez, S., Fabregat-Santiago, F., Hamann, T. & Bisquert, J. Water Oxidation at Hematite Photoelectrodes: The Role of Surface States. *J. Am. Chem. Soc.* **134,** 4294–4302 (2012).

39. Upul Wijayantha, K. G., Saremi-Yarahmadi, S. & Peter, L. M. Kinetics of oxygen evolution at α-Fe_2O_3 photoanodes: a study by photoelectrochemical impedance spectroscopy. *Phys. Chem. Chem. Phys.* **13,** 5264 (2011).

40. Le Formal, F. *et al.* Back Electron–Hole Recombination in Hematite Photoanodes for Water Splitting. *J. Am. Chem. Soc.* **136,** 2564–2574 (2014).

41. Yamakata, A., Vequizo, J. J. M. & Kawaguchi, M. Behavior and Energy State of Photogenerated Charge Carriers in Single-Crystalline and Polycrystalline Powder $SrTiO_3$ Studied by Time-Resolved Absorption Spectroscopy in the Visible to Mid-Infrared Region. *J. Phys. Chem. C* **119,** 1880–1885 (2015).

42. Yoshida, M. *et al.* In situ observation of carrier transfer in the Mn-oxide/Nb:$SrTiO_3$ photoelectrode by X-ray absorption spectroscopy. *Chem. Commun.* **49,** 7848 (2013).

43. Nakamura, R. & Nakato, Y. Primary Intermediates of Oxygen Photoevolution Reaction on TiO_2 (Rutile) Particles, Revealed by in Situ FTIR Absorption and Photoluminescence Measurements. *J. Am. Chem. Soc.* **126,** 1290–1298 (2004).

44. Esposito, D. V., Levin, I., Moffat, T. P. & Talin, A. A. H_2 evolution at Si-based metal–insulator–semiconductor photoelectrodes enhanced by inversion channel charge collection and H spillover. *Nat. Mater.* **12,** 562–568 (2013).

45. Bertoncello, P. Advances on scanning electrochemical microscopy (SECM) for energy. *Energy Environ. Sci.* **3,** 1620 (2010).

46. Zhao, M., Liu, M., Song, G. & Atrens, A. Influence of pH and chloride ion concentration on the corrosion of Mg alloy ZE41. *Corros. Sci.* **50,** 3168–3178 (2008).

47. Jin, J. *et al.* An experimental and modeling/simulation-based evaluation of the efficiency and operational performance characteristics of an integrated, membrane-free, neutral pH solar-driven water-splitting system. *Energy Environ. Sci.* **7,** 3371–3380 (2014).

48. Howl, J. D., Sicard, N. A. E., Publicover, S. J. & Anderson, M. A method for the manufacture of single barrel liquid ion-selective microelectrodes : an in situ study of ant venom pH. *Pflügers Arch. Eur. J. Physiol.* **411,** 212–215 (1988).

49. Elibol, R. B. Z. H. & Peppas, A. G. A. Micromechanical cantilever as an ultrasensitive pH microsensor. *Appl. Phys. Lett.* **81,** 3091–3093 (2002).

50. Bishnoi, S. W. *et al.* All-Optical Nanoscale pH Meter All-Optical Nanoscale pH Meter. *Nano Lett.* **6,** 1687–1692 (2006).

51. Kreft, O., Mun, A., Sukhorukov, B. & Parak, W. J. Polymer microcapsules as mobile local pH-sensors. *J. Mater. Chem.* **17,** 4471–4476 (2007).

52. Ndobo-Epoy, J.-P., Lesniewska, E. & Guicquero, J. Nano-pH Sensor for the Study of Reactive Materials. *Anal. Chem.* **79,** 7560–7564 (2007).

53. Chen, S., Bomer, J. G., Carlen, E. T. & Berg, A. Van Den. Al_2O_3/Silicon NanoISFET with Near Ideal Nernstian Response. *Nano Lett.* **11,** 2334–2341

(2011).

54. Chen, S., Yang, Q., Xiao, H., Shi, H. & Ma, Y. Local pH monitoring of small cluster of cells using a fiber-optic dual-core micro-probe. *Sensors Actuators B. Chem.* **241,** 398–405 (2017).

55. Chen, C.-C., Zhou, Y. & Baker, L. A. Scanning ion conductance microscopy. *Annu. Rev. Anal. Chem.* **5,** 207–28 (2012).

56. Comstock, D. J., Elam, J. W., Pellin, M. J. & Hersam, M. C. Integrated Ultramicroelectrode - Nanopipet Probe for Concurrent Scanning Electrochemical Microscopy and Scanning Ion Conductance Microscopy. *Anal. Chem.* **82,** 1270–1276 (2010).

57. Takahashi, Y., Murakami, Y., Nagamine, K. & Shiku, H. Topographic imaging of convoluted surface of live cells by scanning ion conductance microscopy in a standing approach mode. *Phys. Chem. Chem. Phys.* **12,** 10012–10017 (2010).

58. Nadappuram, B. P., McKelvey, K., Al Botros, R., Colburn, A. W. & Unwin, P. R. Fabrication and Characterization of Dual Function Nanoscale pH-Scanning Ion Conductance Microscopy (SICM) Probes for High Resolution pH Mapping. *Anal. Chem.* **85,** 8070–8074 (2013).

59. Morris, C. A., Chen, C. & Baker, L. A. Transport of redox probes through single pores measured by scanning electrochemical-scanning ion conductance microscopy (SECM-SICM). *Analyst* **137,** 2933–2938 (2012).

60. Takahashi, Y. *et al.* Simultaneous Noncontact Topography and Electrochemical Imaging by SECM/SICM Featuring Ion Current Feedback Regulation. *J. Am. Chem. Soc.* **132,** 10118–10126 (2010).

61. Thakar, R., Weber, A. E., Morris, C. A. & Baker, L. A. Multifunctional carbon nanoelectrodes fabricated by focused ion beam milling. *Analyst* **138,** 5973–5982 (2013).

62. Takahashi, Y. *et al.* Multifunctional Nanoprobes for Nanoscale Chemical Imaging and Localized Chemical Delivery at Surfaces and Interfaces. *Angew.*

Chemie Int. Ed. **50,** 9638–9642 (2011).

63. Le Formal, F. *et al.* Rate Law Analysis of Water Oxidation on a Hematite Surface. *J. Am. Chem. Soc.* **137,** 6629–6637 (2015).

3 – Fabrication and characterisation methods

This chapter is dedicated to the description of the fabrication and characterisation methods that have been used in the experimental part of this project, aiming to a much more easier and immediate understanding of the result that are displayed in chapter 4. In particular, the operative principles of scanning ion conductance microscopy is described: these features have been the main guideline of all applications and set-up configurations.

3.1 – Scanning Ion Conductance Microscopy (SICM)

SICM is a scanning probe technique useful for scanning of samples bathed in electrolytic solutions that utilizes a micro (or nano) pipette. The operation principle of SICM relies on an ion current that flows between an electrode in an external bath solution and another electrode inside a pipette: this ion current, which is highly dependent on the tip-sample separation, is utilized as a feedback signal to maintain the tip-sample separation and to allow the pipette to follow surface morphology, which generates topographic information.[1]

SICM was originally developed in 1989[2] to image nonconductive surfaces immersed in electrolytic solution. Improved feedback techniques further demonstrate the ability to image delicate structures without damaging the sample, allowing robust and high-speed scanning, advancing therefore significantly the opportunities for experimentation with SICM (Fig. 3.1).

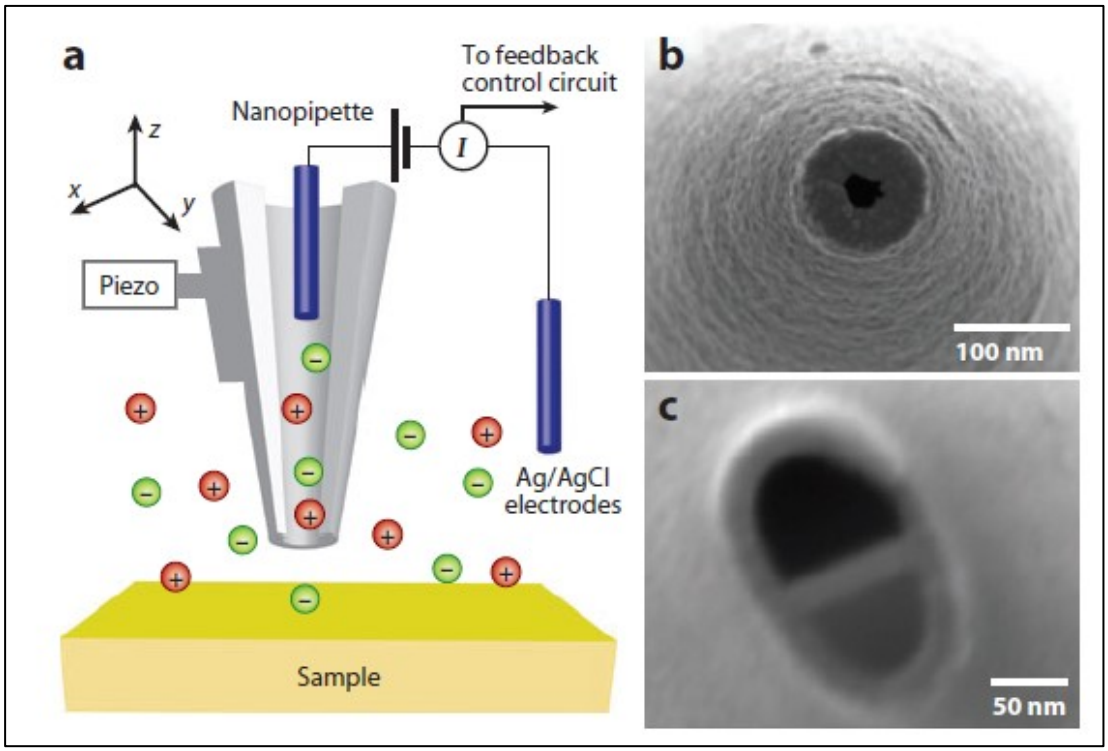

Figure 3.1- Illustration of a scanning ion conductance microscope (SICM). (a) A nanopipette filled with electrolyte is brought in proximity to a sample of interest. A bias applied between an electrode in the pipette and another electrode in the bulk solution generates an ion current, which can be used in feedback control. The nanopipette is mounted on a piezoelectric positioner, which controls the movement of the nanopipette. (b,c) Scanning electron micrographs of (b) a single-barrel nanopipette (~60 nm inner diameter) and (c) a θ pipette (~50 nm inner diameter in both barrels). Such pipettes can serve as probes in SICM.[1]

The SICM probe consists in an electrolyte-filled nanopipette with an Ag/AgCl electrode inserted from the back and is placed in an electrolyte solution: a bias is applied between the reference electrode in solution and the pipette electrode. When the bias is applied, ions flow through the pipette tip between the electrode inside the pipette and the reference electrode to generate an ion current (I). The magnitude of ion currents is determined by the total resistance of the pipette (R_T), that is a combination of the pipette resistance (R_p) and the access resistance between the pipette tip and the sample surface (R_{ac}), which can be described mathematically.[1] Pipette resistance can be calculated geometrically: r_i is the inner radius of the tip opening, r_p is the inner radius of the tip base, h is the tip length, and κ is the conductivity of the electrolyte in the pipette. Although pipette resistance is constant for pipettes with the same geometry, access resistance is strongly affected by the distance (d) between the tip and the sample. A mathematical description of R_{ac} includes the outer radius of the tip opening, r_o. The magnitude of ion currents can be determined from the applied potential (U) and the overall resistance of a pipette (R_T), demonstrating the dependence of ion currents on tip-sample distances:[1]

$$R_p = \frac{h}{\kappa \cdot \pi \cdot r_p \cdot r_i}$$

$$R_{ac} \approx \frac{\frac{3}{2}\ln\left(\frac{r_o}{r_i}\right)}{\kappa \cdot \pi \cdot d}$$

$$I(d) = \frac{U}{R_T} = \frac{U}{R_p + R_{ac}} \approx I_{MAX}\left(1 + \frac{\frac{3}{2}\ln\left(\frac{r_o}{r_i}\right) \cdot r_p \cdot r_i}{h \cdot d}\right)^{-1} \; ; \; I_{MAX} = \frac{U}{R_p}.$$

In an approach curve, when the pipette is far away from the sample surface the ion current is at the maximum value (I_{MAX}). Ion flow is hindered as the pipette approaches very close to the sample surface, and thus causes a rapid decrease in the ion current: therefore, feedback to control tip-sample distances using a piezoelectric positioner is provided by distance-dependent current measured with the pipette. A topographic image can be generated by recording the vertical motion of the pipette as it follows the sample surface. A current image can also be obtained by direct measurements of the ion current.

Three common methods of feedback modes have been developed for SICM: the nonmodulated (dc), distance-modulated (ac), and hopping modes.

3.1.1 – Nonmodulated mode

In dc feedback mode (Fig. 3.2-a), between electrode in the pipette and the one in the bath a constant potential difference is applied. The current-distance response for an SICM pipette approaching to a flat surface is illustrated by an approach curve (Fig. 3.2-d) in which d/r_i represents the tip-sample distance normalized to the pipette's inner radius.

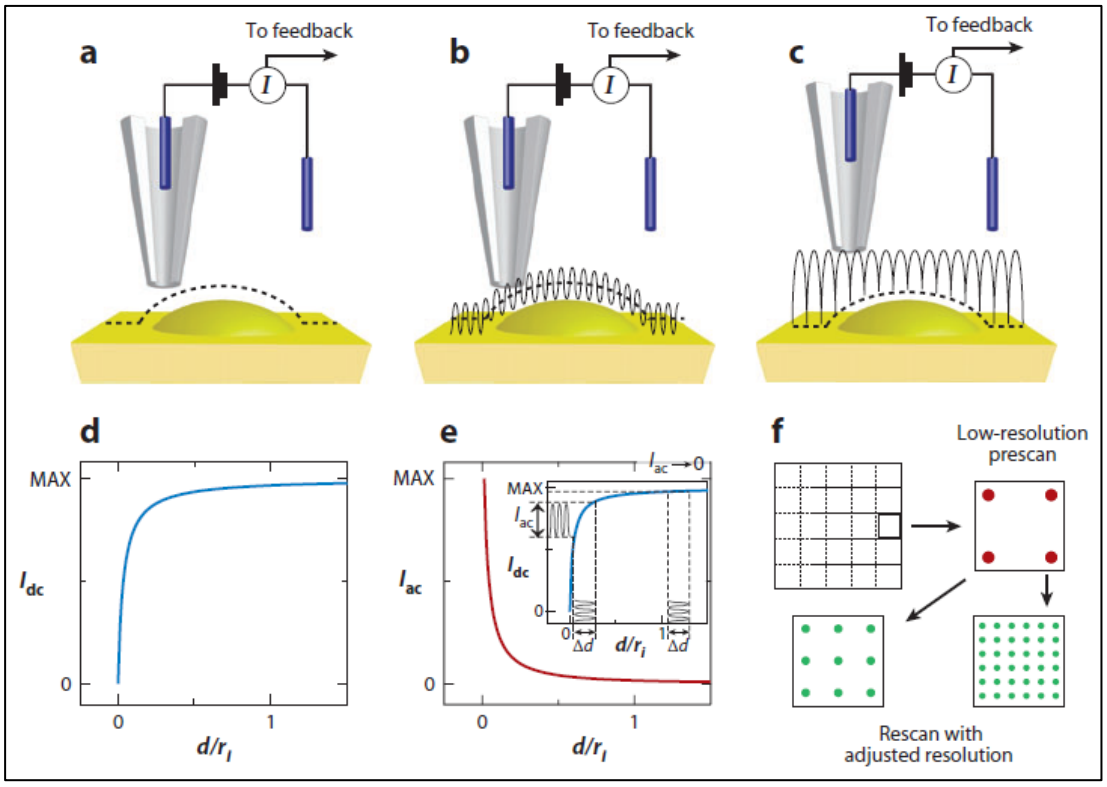

Figure 3.1 - (a–c) Schematic of nonmodulated (dc), distance-modulated (ac), and hopping feedback modes in scanning ion conductance microscopy. (a) Nonmodulated feedback control. In this mode, the dc ion current is sensitive to the tip-surface distance, as shown in (d) the dc approach curve, which is used directly to control the position of the pipette. d/r_i represents the tip-sample distance normalized to the pipette inner radius. (b) Distance-modulated feedback control. In this mode, the pipette is modulated with a constant distance (Δd), which results in a modulated ion current (I_{MOD}). In this mode, the ac component of I_{MOD} is used to maintain the tip-surface distance. Approach characteristics of a modulated pipette are shown in panel e, in which Idc represents the dc component of I_{MOD}, and Iac represents the ac component (peak-to-peak amplitude) of I_{MOD}. (c) Hopping feedback control. In this mode, the pipette approaches the sample and withdraws before touching the surface at each imaging point. A prescan is performed with a small number of imaging points to estimate surface roughness, as shown in panel f.[1]

There are two regions in the approach curve: (a) a steady-state region, in which the ion current is unaffected by tip-sample separations and remains close to the maximum current, and (b) another region, in which the ion current declines rapidly as the tip-sample distance decreases.[1] The pipette position, which provides a method of feedback and control of the pipette in the z dimension, strongly affects the ion current in this region near the surface. Could be difficult, for samples with high aspect ratio features, to collect images very close to the surface in the dc mode. For this reason, tip-sample distances on the order of the radius of the pipette opening have been proposed to prevent surface contact: in this case, the distances from the pipette tip centre to the nearest abrupt surface features and to the sample surface right under the pipette tip are similar.[1] Consequently, contact from all directions can be minimised.

To cite an application, SICM with nonmodulated feedback provides adequate control, which is needed to analyse biological samples: SICM can also detect submicrometer features of cell membrane surfaces and small membrane changes. However, in certain cases the response of dc feedback can be too slow, for example with living cells with rapid height changes of several micrometers, and is susceptible to changes in the ion current that result from dc drift, partial blockage of the pipette, or changes in the ionic strength of the solution: to overcome all these problems, a more reliable feedback control, distance-modulated (ac) mode, was introduced.

3.1.2 – Distance-modulated mode

The ac feedback mode was developed to improve pipette control: in this feedback mechanism (Fig. 3.2-b), the pipette position is modulated vertically at a fixed displacement.[1] An oscillation in the access resistance is produced as the probe tip approaches the vicinity of the sample surface with pipette modulation; this oscillation introduces an ac component to the pre-existing dc current of the pipette, generating a modulated ion current. A lock-in amplifier recovers the modulated current, using it as a feedback control signal. The approach curve for the ac feedback mode (Fig. 3.2-e) is obtained by plotting the ac component (peak-to-peak amplitude) of the modulated current as a function of normalized tip-sample distances (d/r_i).[1] The approach curve for the dc component of the modulated current illustrates how the amplitude of the modulated current changes with tip-sample distance.[1] In the case of nonmodulated feedback, when the pipette is located away from the sample a maximum current is observed, and it decreases as the pipette approaches the sample: however, in the case of the modulated current, only when the pipette is very close to the sample a signal is observed.

The surface sensitivity of the modulated current has significant advantages, with respect to the feedback loop, in comparison to the nonmodulated pipette current. Changes in the ion current that are not in phase with the modulation frequency do not affect control of the pipette position: this is indeed an advantage of modulated feedback mode. With the increased stability of modulated feedback, both long-term, continuous observation of delicate samples and the ability to maintain control during changes in the ionic strength of the bath solution have been realized.

3.1.3 – Backstep and Hopping approach modes

The necessity of imaging samples with highly complex surface features led to the development of backstep and hopping approach modes. These feedback modes employ a series of approach curves to determine sample topography: in these modes, the pipette approaches a surface to a defined distance, is withdrawn and repositioned, and then approaches the surface again at the new location (Fig. 3.2-c).[1] Both resolution and imaging time are determined by the number of imaging points. In hopping mode, to speed up image collection, the surface is imaged first at low resolution to determine sample complexity and estimate roughness: high-resolution imaging can thus be conducted in areas with more complex structures;[1] regions that are less interesting can be imaged with fewer points, and the distance of pipette withdrawal can also be adjusted to accelerate image collection according to sample roughness. The hopping mode has been used to image challenging samples with complex three-dimensional structures: the probe did not damage the sample and this demonstrates the ability of this mode to image samples with extremely convoluted surfaces.[1]

3.1.4 – SICM probes

Various geometrical and unique fluidic properties of scanned nanopipettes are of primary importance to the operation and development of SICM. In this section, the fabrication and characterization of nanopipettes commonly utilized in SICM will be briefly described.

SICM usually employs single-barrel nanopipettes as the scanning probe, which can be easily fabricated: to prepare a nanopipette, a heat source (filament, flame or laser) is used to soften a clamped capillary and then a mechanical pull separates the capillary to form a pair of pipettes. Through the adjustment of puller parameters, it is possible to obtain pipettes with different cone angles, taper lengths, and tip diameters. Quartz capillaries have been used to prepare small tips with reported diameters of ~8 nm.[3]

In addition to single-barrel nanopipettes, θ nanopipettes have also been utilized extensively in SICM applications:[1] such nanopipettes are pulled from θ capillaries to form pipettes and each barrel can be filled with different electrolyte solutions; when independent electrodes are placed inside of each barrel, it can be achieved electrical control of each individual barrel. These nanopipettes are used to deposit species onto a sample by voltage pulsing and capillaries with more than two barrels are also available; they potentially allow more reagents to be delivered independently from the same pipette.

3.1.5 – Resolution and theoretical models

The pipette tip geometry and tip-sample distance determine resolution in SICM, which is typically ∼10 nm vertically and ∼50 nm laterally.[1] The highest resolution reported is 3–6 nm[4] with a nanopipette whose tip was estimated to be 13 nm in inner diameter. Lateral resolution is defined as the smallest distance between two particles at which individual particles can be resolved in an image: this definition was used in simulations and the resolution determined was approximately three times the size of the inner radius of the pipette tip.[1]

Several models for SICM have been proposed to describe how ion current changes as a function of pipette geometry and surface topography as well as how tip-sample distances affect image resolution and lead to possible image artifacts.[1] For single-barrel nanopipettes, finite element models predict that ion current drops at larger tip-sample distances for pipettes with a larger tip diameter, a greater cone angle, or a higher ratio of outer radius to inner radius. In these models a cylindrical pit, a step and particles of different heights have been included in addition to flat surfaces, to study the current characteristics of a pipette as it interacts with different sample structures: image artifacts have been found in scans of structures with instantaneous steps, which can be explained by the different pathways ions may take when the pipette scans over a step. The models also predict that nonuniform electric fields at the pipette tip can lead to artifacts.[1]

3.1.6 – Attributes of SICM

The primary advantages of SICM include noncontact surface imaging and the ability to image with inert (e.g., not electrochemically or photonically active) ions.

Atomic force microscopy (AFM) is a good comparator for SICM: AFM can image with high resolution, but is a force-based technique and typically nonzero forces are involved during imaging, even in tapping mode. These forces increase the probability of damage to or deformation of soft and fragile features.[1] In contrast, SICM can perform noncontact imaging of fragile or highly convoluted surface features. As a comparison, alternating sequences of SICM and AFM images for small and loosely attached cellular extensions have been recorded:[1] images of cells obtained with AFM present obvious morphological distortions that result from the inherent imaging force, whereas no evident topographic deformation has been observed in SICM images. Anyway, the motions of the probe in close proximity to sample surfaces, or distortions of the local electric field from the pipette tip, can generate interactions with the specimen under study even though SICM is noncontact.[1]

Scanning electrochemical microscopy (SECM) is another powerful scanning probe technique for the study of electrochemical properties in versatile systems. An electron-transfer reactions of redox mediators at the probe tip is typically used to generate the feedback signal utilized in SECM: consequently, the capability of SECM for the investigation of particular specimens may be limited if the redox mediator interferes with the sample in some way (e.g., toxicity) or if the electrical properties of the tip are fouled during operation in biological media.[1] The same drawback, namely signal transduction that interferes with sample function, may also arise in the case of fluorescence microscopy, in which fluorescent dyes or fluorescently tagged proteins can alter the properties of the system under study.[1]

3.2 – Metal Organic Chemical Vapour Deposition (MOCVD)

Metal-organic chemical vapour deposition (MOCVD) consists in the growth of thin layers of compound semiconducting materials by the co-pyrolysis of various combinations of organometallic compounds and hydrides, and has assumed a great role of

technological importance in the fabrication of a number of optoelectronic and high speed electronic devices.[5] The initial demonstration of compound semiconductor film growth was first reported in 1968:[6] since then, both commercial and scientific interest has been largely directed toward epitaxial growth on semiconductor rather than insulator substrates. Readily transportable, high purity organometallic compounds can be prepared for most of the elements that are of interest in epitaxial deposition, one of the main reasons of the appeal of MOCVD technique: in addition, a large driving force (i.e., a large free energy change) exists for the pyrolysis of the source chemicals[5] and this means that a wide variety of materials can be grown using this technique, where with other epitaxial techniques that could be difficult.

Improving the quality of materials that can be grown by MOCVD while maintaining and improving inter and intrawafer uniformity on increasingly large substrates has been the main focus of recent research: this effort has led to great improvements in MOCVD equipment design and construction, particularly on the part of equipment vendors.[5] Early MOCVD equipment was designed to optimize either wafer uniformity, interfacial abruptness, or wafer area, depending on the device application intended: during the 1970s and early to mid-1980s there were few demonstrations of all three attributes (uniformity, abrupt interfaces, and large areas) in the same apparatus and most of all not a common vision on how MOCVD systems, particularly reaction chambers, should be designed.[5]

3.2.1 – Physical and chemical properties of sources used in MOCVD

Various combinations of organometallic compounds and hydrides are the sources that are used in MOCVD for both major film constituents and dopants. The III-V and II-VI compounds and alloys are usually grown using low molecular weight metal alkyls as the metal (Group II or Group III) source. The non-metal (Group V or Group VI) source is either a hydride or an organometallic.[5] The sources are introduced as vapour phase constituents into a reaction chamber at approximately room temperature and are thermally decomposed at elevated temperatures by a hot susceptor and substrate to form the desired film in the reaction chamber.[5] The chamber walls are deliberately not heated (it is called a “cold wall” process) and do not directly affect the

chemical reactions that occur in the chamber. The general overall chemical reaction that occurs during the MOCVD process can be written:[5]

$$R_nM(v) + ER'_n(v) \rightarrow ME(s) + nRR'(v)$$

where R and R′ represent a methyl (CH_3) or ethyl (C_2H_5) (or higher molecular weight organic) radical or hydrogen, M is a Group II or Group III metal, E is a Group V or Group VI element, n = 2 or 3 (or higher for some higher molecular weight sources) depending on whether II-VI or III- V growth is taking place, and *v* and *s* indicate whether the species is in the vapour or solid phase.

The vapour phase reactants R_nM and ER'_n are thermally decomposed at elevated temperatures, forming the non-volatile product ME which is deposited on the substrate and the susceptor, while the volatile organic product RR′ is carried away to the exhaust by an H_2 gas flow.[5] The MOCVD growth of mixed alloy can be described by substituting two or more appropriate reactant chemicals of the same valence in place of the single metal or non-metal species. Virtually all of the possible III-V and II- VI compounds and alloys have been grown by MOCVD.[5]

Generally, clear liquids or occasionally white solids around room temperature represent the organometallic compounds that are used for MOCVD: they are often pyrophoric or highly flammable and have relatively high vapour pressures in the range of 0.5-100 Torr around room temperature.[5] They can be readily transported to the reaction chamber as vapour phase species by bubbling a suitable gaseous carrier (generally H_2) through the compound as it is held in a container at temperatures near room temperature. The organometallic compounds are generally monomers in the vapour phase. As a general rule, the low molecular weight compounds tend to have higher vapour pressures at a given temperature than the higher molecular weight materials.[5]

The commonly used sources are generally thermally stable around room temperature: thus, the materials are expected, for the most part, to be stable under operative conditions even if stored for long, extended periods of time. As the reactant molecules encounter the hot susceptor, they will begin to thermally decompose in the MOCVD reaction chamber: the temperature at which an organometallic compound will begin to decompose is not particularly well defined, since it is a function of both the surfaces with which the organometallic comes in contact and the gas ambient.[5] Moreover, the

decomposition will be affected by the residence time of the chemical species near the hot pyrolysing surface, which implies a flow rate and perhaps a reactor geometry dependence of the thermal decomposition. Generally, however, the reported decomposition temperatures are in the range of 200 to 400°C for most of the metal alkyls.[5]

3.2.2 – Growth mechanisms, conditions and chemistry

As mentioned earlier, MOCVD takes place in a cold wall reactor in an environment of large thermal and compositional gradients: within this environment, many chemical reactions can take place, both in the vapour phase and at the growing surface, and many of these potential reactions can have extremely deleterious effects on the growing films. A general formalism to understand MOCVD growth chemistry was presented schematically in literature works[7] (Fig. 3.3).

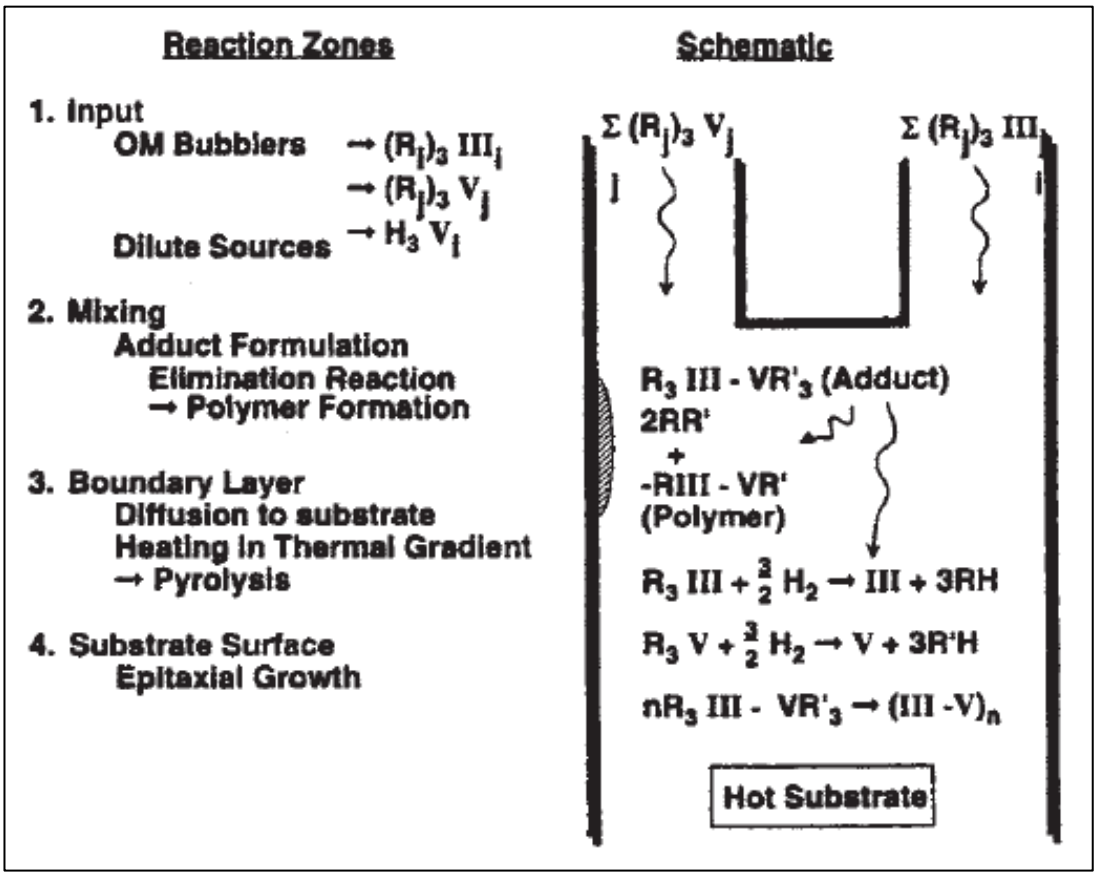

Figure 3.2 - Reaction regimes for the MOCVD process.[5,7]

The MOCVD growth process can be divided into four regimes: a reactant input regime, a reactant mixing regime, a boundary layer regime immediately above the substrate, and the growth on the substrate surface, itself. Gas phase reactions during reactant mixing, reactant diffusion and/or pyrolysis in the boundary layer above the substrate, and thermodynamic or kinetic rejection of species from the substrate are some of the growth complications that can occur in these regimes. Anyway, through the use of appropriate equipment design and process conditions, the worst of these effects can be reduced or eliminated.[5]

3.2.3 – System design and construction

A block diagram of an MOCVD system, in which functional subsystems are defined, is depicted in Fig. 3.4. Subsystems consist of: reactant storage (hydrides, organometallics and H_2); a gas manifold in which flows are metered, controlled and directed to the proper locations; a reaction chamber in which deposition takes place; an exhaust, which generally includes a pump for low pressure operation and evacuation of the chamber for substrate loading and unloading and a scrubber.[5]

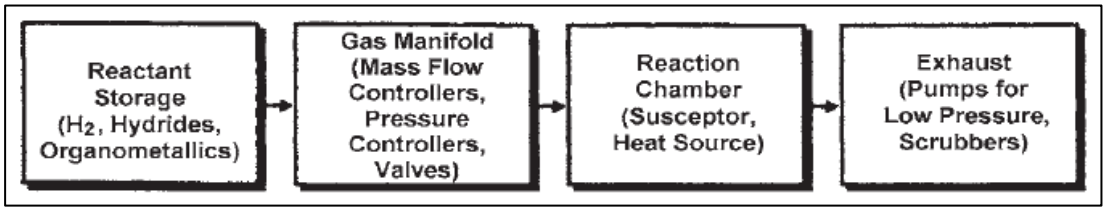

Figure 3.3 - Schematic block diagram of an MOCVD system showing functional subsections.[5]

Considering this general set-up, the classic procedure of MOCVD can be summed up in the following steps. At first there is the generation of volatile chemical compounds, which are used as "carrier" to transport materials which are much less volatile: in some cases a simple sublimation of the precursor will give the desired effect, while other procedures contemplate the reaction between the precursor and a reacting gas to generate the volatile compound; a third case is that of a gaseous precursor. In every case, subsequently to the generation inside a "pre-chamber" the volatile compound is transported inside the reactor using a stream of an inert gas. The third and final step is the chemical reaction to form a solid product: reactions used in this final

step are thermal decomposition, reduction of a halide by hydrogen, reduction of a halide to give refractory compound (carbide, nitride, oxide), disproportion reaction.

It is not the aim of this dissertation to look too much in detail on single components of the MOCVD set-up, therefore we will focus only on the reaction chamber, where the thermal decomposition reaction and deposition occurs. The abruptness of interfaces is largely controlled by the reaction chamber of an MOCVD system because this section contains the longest time constant for reactant flushing: in addition, reaction chamber design controls almost entirely the lateral uniformity of material grown. Chambers are cold wall, therefore the susceptor upon which the substrate sits is the only part of the reactor that is deliberately heated: the cold wall design reduces the probability that competing chemical reactions at the walls (such as thermal decomposition) will interfere with film growth.[5] Of course, the establishment of thermally driven natural convection in the chamber is favoured by cold wall designs because of the large temperature gradients present: this natural convection can lead to recirculation cells in the chamber, which in turn result in non-abrupt interfaces and reactor non-uniformities; these can be eliminated by reactor design and growth conditions. Often, reaction chambers are provided with a vacuum and/or N_2 flushed load lock, which keeps ambient air from entering the chamber and provides an additional level of safety during sample loading and unloading. The chamber walls can be either water or ambient-air cooled: latter systems can have wall temperatures of 200°C for susceptor temperatures of 650°C. Unintentional changes in wall temperatures can have significant effects on the composition of films grown.[5]

3.3 – Dip coating

Sol-gel dip coating consists in the withdrawal of a substrate from a fluid sol: deposition of a solid film is the result of gravitational draining and solvent evaporation, accompanied by further condensation reactions. Compared with conventional thin film forming processes (such as MOCVD, evaporation or sputtering), sol-gel dip coating requires considerably less equipment and is potentially less expensive: however, the most important advantage of sol-gel over conventional coating methods is the ability to tailor the microstructure of the deposited film.[8]

The sol-gel process uses inorganic or metal organic compounds as raw ingredients and in aqueous (or organic) solvents these compounds are hydrolysed and condensed to form inorganic polymers composed of M--O--M bonds. For inorganic compounds, hydrolysis proceeds by the removal of a proton from an aquo ion $[MO_NH_{2N}]^{z+}$ to form a hydroxo (M–OH) or oxo (M=O) ligand.[8] Condensation reactions involving the hydroxo ligands result in inorganic polymers in which metal centres are bridged by oxygens or hydroxyls. The most commonly used metal organic compounds are metal alkoxides $M(OR)_z$, where R is an alkyl group C_xH_{2x+1}.[8] Normally the alkoxide is dissolved in alcohol and the addition of water hydrolyses it under acidic, neutral, or basic conditions. Hydrolysis results in the replacement of an alkoxide with a hydroxyl ligand:

$$M(OR)_z + H_2O \rightarrow M(OR)_{z-1}OH + ROH$$

In dip coating, the substrate is normally withdrawn vertically from the liquid bath at a speed U_0. The moving substrate entrains the liquid in a fluid mechanical boundary layer that splits in two above the liquid bath surface, the outer layer returning to the bath. Since the solvent is evaporating and draining, the fluid film terminates at a well-defined drying line (x = 0 in Fig. 3.5). When the receding drying line velocity equals U_0, the process is steady state with respect to the liquid bath surface.[8] A non-constant evaporation rate close to the drying line (due to geometrical factors affecting the diffusion of solvent vapour from the liquid surface) results in a parabolic thickness profile:

$$h(x) \propto x^{1/2}$$

where h(x) is the film thickness as a function of position x below the drying line.

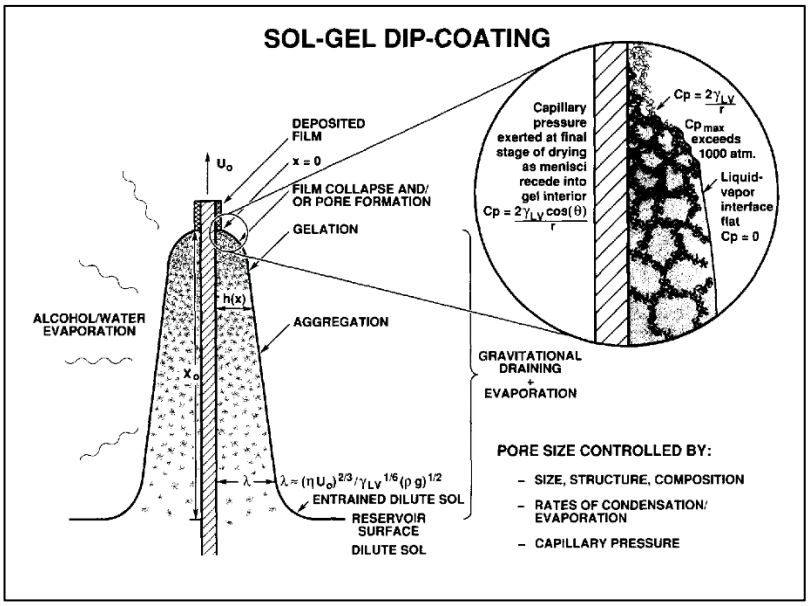

Figure 3.4 - Schematic diagram of the steady-state dip coating process, showing the sequential stages of structure development that result from draining accompanied by solvent evaporation and continued condensation reactions. Adapted from ref. 8.

Competition between as many as six forces in the film deposition region governs the film thickness and position of the stream line.[8] When the liquid viscosity η and substrate speed U_0 are high enough to lower the curvature of the meniscus, the deposited film thickness h is that which balances the viscous drag (proportional to μ U_0/h) and gravity force (ρgh):

$$h = c_1(\eta\, U_0/\rho g)^{1/2}$$

where the constant c_1 is about 0.8 for newtonian liquids. When the substrate speed and viscosity are low (often the case for sol gel film deposition), this balance is modulated by the ratio of viscous drag to liquid-vapour surface tension γ_{LV} according to the relationship derived by Landau and Levich:[8]

$$h = \frac{0.94(\eta U_0)^{2/3}}{\gamma_{LV}{}^{1/6}(\rho g)^{1/2}}$$

Gravitational draining and evaporation, often accompanied by continued condensation reactions, rapidly concentrate on the substrate surface the entrained inorganic precursors (polymers or particles), causing therefore the deposition of the inorganic film. The increasing concentration forces the precursors into close proximity, causing reactive species to aggregate and gel, while repulsive particles appear to assemble into liquid- or crystal-like structures, depending on the withdrawal rate. Using

reactive precursors there is a competition between solvent evaporation, which compacts the structure, and continuing condensation reactions, which stiffen the structure increasing its resistance to compaction. Unlike conventional bulk gel formation, the drying stage overlaps the aggregation-gelation stages, establishing only a brief time span (several seconds) for condensation reactions to occur.[8] A common result is rather compliant structures that are collapsed at the final stage of drying by the capillary pressure P created by the liquid-vapour menisci as they recede into the film interior:

$$P = \frac{2\gamma_{LV}\cos\theta}{r}$$

where θ is the wetting angle and r is the hydraulic radius of the pore at the moment the meniscus recedes into the gel interior. Because r may be very small (less than 1.0 nm), *P* may exceed 60 MPa even for liquids with low surface tensions such as ethanol. Different pressure values between adjacent pores may therefore cause cracking during the evaporation of the solvent.[8]

3.4 – Electrochemical methods

It is well known that electrochemistry is one of the most powerful tools available to a scientist, for both deposition of chemical species over a surface and for many kinds of chemical analysis (of substrates, solutions, reaction mechanism, etc.). Considering the work performed for this project, electrochemical methods constitute the backbone of the experimental part.

In electrochemical systems, we are concerned with the processes and factors that affect the transport of charge across the interface between chemical phases, for example between an electronic conductor (an electrode) and an ionic conductor (an electrolyte). The movement of electrons (and holes) allows charge transport through the electrode. Typical electrode materials include solid metals (e.g., Pt, Au), liquid metals (Hg, amalgams), carbon (graphite), and semiconductors (indium-tin oxide, Si). In the electrolyte phase, charge is carried by the movement of ions: the most frequently used electrolytes are liquid solutions containing ionic species, such as H^+, Na^+, Cl^-, in either

water or a nonaqueous solvent. To be useful in an electrochemical cell, the solvent/electrolyte system must have a sufficiently low resistance (i.e., be sufficiently conductive) for the electrochemical experiment in exam. Less conventional electrolytes include fused salts (e.g., molten NaCl-KCl eutectic) and ionically conductive polymers (e.g., Nation). Solid electrolytes also exist (e.g., sodium β-alumina, where charge is carried by mobile sodium ions that move between the aluminium oxide sheets).[9]

In general, in an electrochemical cell it is possible to measure a difference in electric potential between the electrodes: typically, this is done with a high impedance voltmeter. This cell potential, measured in volts (V, where 1 V = 1 joule/coulomb (J/C)), is a measure of the energy available to drive charge externally between the electrodes: it is a manifestation of the collected differences in electric potential between all of the various phases in the cell.[9] The sharpness of the transition implies that a very high electric field exists at the interface, which it is supposed to affect the behaviour of charge carriers (electrons or ions) in the interfacial region. Also, the magnitude of the potential difference at an interface affects the relative energies of the carriers in the two phases; hence it controls the direction and the rate of charge transfer. Thus, the measurement and control of cell potential is one of the most important aspects of experimental electrochemistry.[9]

The overall chemical reaction taking place in a cell could be represented by two independent half-reactions, which describe the real chemical changes at the two electrodes. Each half-reaction (and, consequently, the chemical composition of the system near the electrodes) responds to the interfacial potential difference at the corresponding electrode. Usually, an electrochemical experiment is focused in only one of these reactions and the electrode at which it occurs is called the working (or indicator) electrode, WE. Using an electrode (called a reference electrode, RE) made up of phases having essentially constant composition, it is possible to standardize the other half of the cell.

The internationally accepted primary reference is the standard hydrogen electrode (SHE), or normal hydrogen electrode (NHE), which has all components at unit activity:

$$Pt/H_2\ (a = l)\ /H^+\ (a = 1, \text{aqueous})$$

Potentials are often measured and quoted with respect to RE other than the NHE, which is not very practical from an experimental point of view: a common reference is the saturated calomel electrode (SCE), which is

$$Hg/Hg_2Cl_2/KCl\ (\text{saturated in water})$$

and its potential is 0.242 V vs. NHE. Another is the silver-silver chloride electrode,

$$Ag/AgCl/KCl\ (\text{saturated in water})$$

with a potential of 0.197 V vs. NHE. It is common to see potentials identified in the literature as "vs. Ag/AgCl" when this electrode is used.

Since the structure and composition of the RE is held constant, its potential is fixed: therefore, any changes in the cell are imputable to the WE. Every electrochemical experiment consists in the observation or control of the potential of the WE with respect to the RE, equivalent to observing or controlling the energy of the electrons within the WE. In this typical experiment, a WE and a RE are immersed in a solution and the potential difference between the electrodes is varied: this variation in potential, *E*, can produce a current flow in the external circuit because electrons cross the electrode/solution interfaces as reactions occur. Recall that the number of electrons that cross an interface is related stoichiometrically to the extent of the chemical reaction (i.e., to the amounts of reactant consumed and product generated). The number of electrons is measured in terms of the total charge, Q, passed in the circuit and charge is expressed in units of coulombs (C), where 1 C is equivalent to $6.24 \cdot 10^{18}$ electrons. The relationship between charge and amount of product formed is given by Faraday's law; that is, the passage of 96485.4 C causes 1 equivalent of reaction (e.g., consumption of 1 mole of reactant or production of 1 mole of product in a one-electron reaction). The current, *i*, is the rate of flow of coulombs (or electrons), where a current of 1 ampere (A) is equivalent to 1 C/s.[9] Plotting the current as a function of the potential, a current-potential (*i* vs. *E*) curve is obtained: such curves can be quite informative about the nature of the solution and the electrodes and about the reactions that occur at the interfaces.

3.4.1 – Electrochemical cells and cell resistance

As introduced before, the main interest in an electrochemical experiment is focused towards reactions that occur at only one electrode. An experimental cell could be therefore composed of the electrode system of interest, the WE, coupled with an electrode of known potential that approaches ideal nonpolarisability (such as an SCE with a large-area mercury pool), the RE. Under conditions when voltage drop due to the resistance of solution (iR_S) is small (less than 1-2 mV), this two-electrode cell can be used to determine the *i*-*E* curve, with *E* either taken as equal to E_{appl} or corrected for the small potential drop.

With more highly resistive solutions, such as those based on many nonaqueous solvents, a very small electrode (an ultra micro electrode, UME) must be used if a two-electrode cell is to be employed without serious complications from the ohmic drop in solution. With such electrodes, currents of the order of 1 nA are typical; hence R_S values even in the MΩ range can be acceptable.[9]

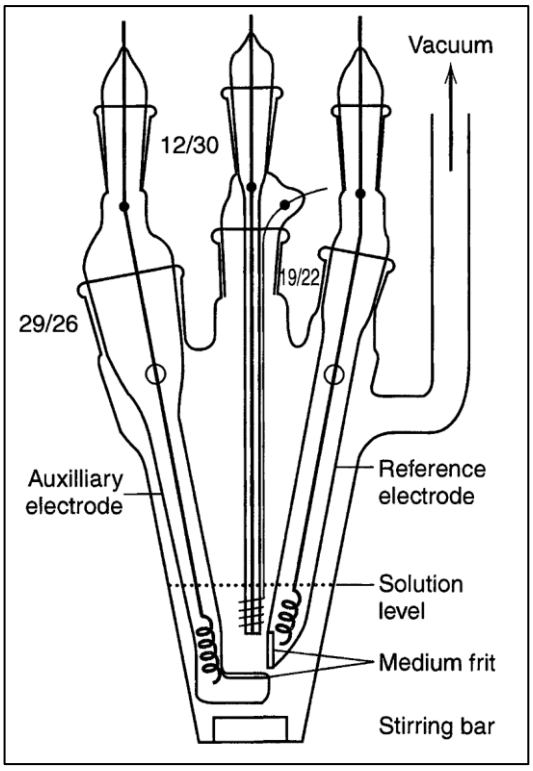

Figure 3.5 – Practical example of a three-electrode electrochemical cell. Adapted from ref. 9.

In experiments where iR_S may be high (e.g., in large-scale electrolytic or galvanic cells or in experiments involving nonaqueous solutions with low conductivities),

a three-electrode cell (Fig. 3.6) is preferable: in this arrangement, the current is passed between the WE and a counter (or auxiliary) electrode, CE. Since its electrochemical properties do not affect the behaviour of the electrode of interest, the auxiliary electrode can be any convenient one: it is usually chosen to be an electrode that does not produce substances by electrolysis that will reach the surface of the WE causing interfering reactions there; it is frequently placed in a compartment separated from the WE by a sintered-glass disk or other separator. The potential of the WE is monitored relative to a separate RE, positioned with its tip nearby: the device used to measure the potential difference between the two electrodes has a high input impedance, so that through the reference electrode flows a negligible current.[9] Consequently, the potential of the RE will remain constant and equal to its open-circuit value: this three-electrode arrangement is used in most electrochemical experiments.

Even in this arrangement, not all of the iR_S term is removed from the reading made by the potential-measuring device. Consider the potential profile in solution between the WE and CE: the solution between the electrodes can be regarded as a potentiometer (but not necessarily a linear one). If the RE is placed anywhere but exactly at the electrode surface, some fraction of iR_S, (called iR_U, where R_U is the uncompensated resistance) will be included in the measured potential. Even when the tip of the RE is designed for very close placement to the working electrode by use of a fine tip called a Luggin-Haber capillary, some uncompensated resistance usually remains. This uncompensated potential drop can sometimes be removed later, for example, from steady-state measurements by measurement of R_U and point-by-point correction of each measured potential. Modern electrochemical instrumentation frequently includes circuitry for electronic compensation of the iR_U term.[9]

3.4.2 – Cyclic voltammetry

Useful information on the electrochemical behaviour of a system can be obtained in a single experiment by sweeping the potential with time and recording the *i*-*E* curve directly. Usually the potential is varied linearly with time (i.e., the applied signal is a voltage ramp) with sweep rates v ranging from 10 mV/s (1 V traversed in 100 s) to about 1000 V/s with conventional electrodes and up to 10^6 V/s with UMEs.[9] In this experiment, it is common practice to record the current as a function of potential,

which is equivalent to recording current versus time. The formal name for the method is linear potential sweep chronoamperometry, but it is preferable to refer to this as linear sweep voltammetry (LSV). What happens if the potential scan is reversed? This experiment, which is called cyclic voltammetry (CV), is a reversal technique. Cyclic voltammetry has become a very popular technique for initial electrochemical studies of new systems and has proven very useful in obtaining information about fairly complicated electrode reactions.[9]

By switching the direction of the scan at a certain time $t = \lambda$ (or when the switching potential, E_λ, is reached), the potential is given at any time by

$$(0 < t < \lambda) \qquad E = E_i - vt$$

$$(t > \lambda) \qquad E = E_i - 2v\lambda + vt$$

While it is possible to use a different scan rate (v') on reversal, this is rarely done, and only the case of a symmetrical triangular wave is considered here.

Without going too deep into details, this section will describe only systems with Nernstian behaviour. The shape of the curve on reversal depends on the switching potential, E_λ, or how far beyond the cathodic peak the scan is allowed to proceed before reversal. However, if E_λ is at least 35/n mV (with n the number of electrons involved) past the cathodic peak, the reversal peaks all have the same general shape, basically consisting of a curve shaped like the forward *i*-*E* curve plotted in the opposite direction on the current axis, with the decaying current of the cathodic wave used as a baseline[9] (Fig. 3.7).

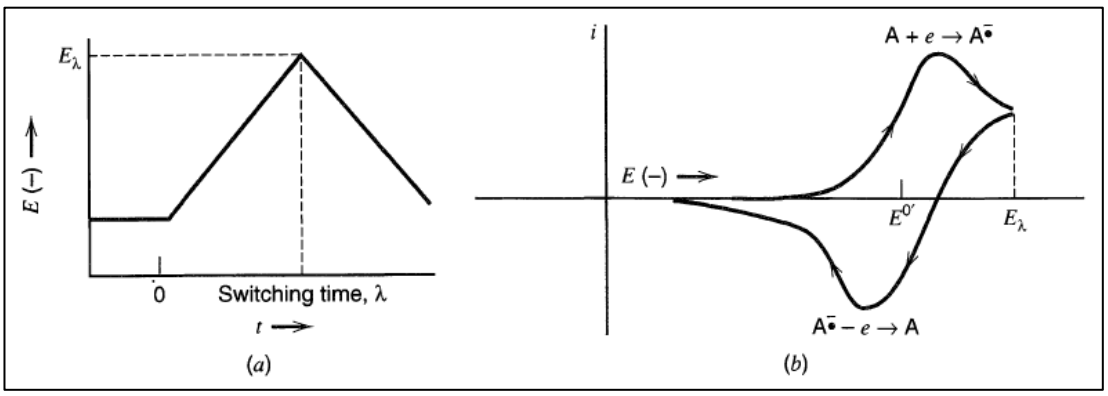

Figure 3.6 - (a) Cyclic potential sweep, (b) Resulting cyclic voltammogram.[9]

Two measured parameters of interest on these *i-E* curves (cyclic voltammograms) are the ratio of peak currents, i_{pa}/i_{pc}, and the separation of peak potentials, E_{pa} - E_{pc}. For a Nernstian wave with stable product, $i_{pa}/i_{pc} = 1$ regardless of scan rate E_λ (for $E_\lambda > 35/n$ mV past E_{pc}) and diffusion coefficients.[9]

In real cyclic voltammograms, the faradaic response is superimposed on an approximately constant charging current. Upon reversal, the magnitude of dE/dt remains constant, but the sign changes: hence the charging current is also of the same size, but opposite in sign. It forms a baseline for the reversal response just as for the forward scan, and both i_{pc} and i_{pa} must be corrected correspondingly.[9]

Concluding, the potentiality of CV as electroanalytical method lies in its diagnostic strength, which is derived from the ease of interpreting qualitative and semi-quantitative behaviour of the system under analysis.

3.5 – Photolitography

Microfabrication technique consists in fabricating miniature structures of micrometre scales and smaller. During this process, photosensitive polymers are used to form fine-line stencil masks thin, called photoresists or resists, which selectively protect an underlying wafer substrate against chemical or physical attack. In particular, optical lithography involves the use of radiation in the optical region of the electromagnetic spectrum as a mean for patterning the resist.

A generalised photolithographic system is depicted in Fig. 3.8. The information to be replicated is delineated on a thin, optically opaque layer supported by a transparent substrate: this pattern, called mask, is transferred or imaged by a lithographic exposure system to form an aerial image, which consists of a spatially dependent light intensity pattern in the vicinity of the wafer.[10] In most cases, the resist becomes more soluble to a chemical developer when the resist-coated wafer is exposed to the aerial image (if the photoresist has a positive tone; cf. section 3.5.2): this allows an easy removal of the exposed regions. The resist image remaining on the wafer behaves as a stencil for subsequent processing, such as etching or metallization.[10]

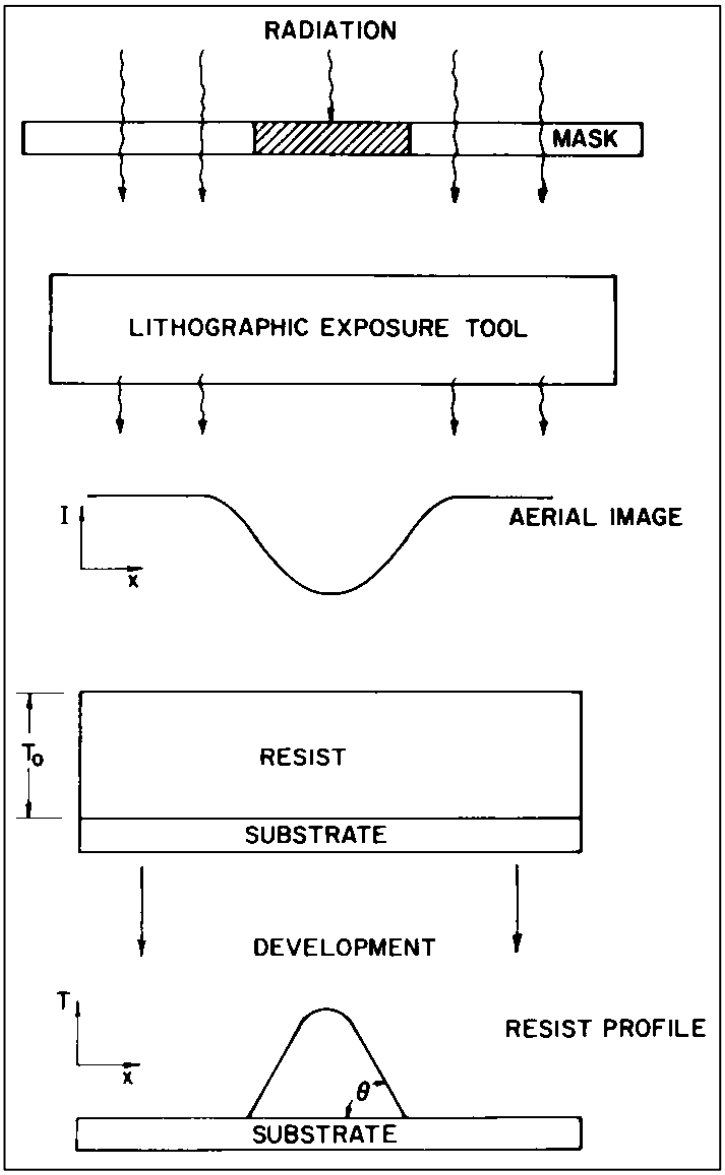

Figure 3.7 – Idealised photolithographic system.[10]

Ideally, when the aerial image duplicates the mask pattern without loss of information or distortion a perfect lithographic process is achieved. Similarly, the perfect resist process responds with full resist thickness for an exposure intensity below a threshold value and with complete removal of the resist for exposures above the threshold.[10] Anyway, in real applications it is in the nature of the physical and chemical processes that such a perfect lithographic system is never realized: the lithographic system behaves less ideally as the minimum geometries on the mask get smaller.

3.5.1 – Optical exposure techniques

Contact printing, as the name suggests, simply consists in bringing the resist-coated wafer in physical contact with the mask and illuminating the back of the mask with actinic radiation. Procedure consists in holding the wafer flat against a vacuum chuck, then the back of the chuck swivels in a spherical socket: contact is achieved by vertically transporting the wafer chuck assembly until the wafer is in intimate contact with the mask surface. In order to achieve planarity with the mask, the socket allows the chuck to tilt. To align the mask pattern to the wafer, a high-powered microscope objective is brought behind the mask, allowing the operator to view the mask and wafer patterns simultaneously. With the microscope in position, the wafer chuck assembly is withdrawn to provide an air gap between the mask and wafer surfaces; alignment is achieved by translating or rotating the wafer until its pattern overlays the mask pattern. When the wafer is brought back into contact, the microscope is moved away and an exposing source of illumination is brought into position. Exposure is achieved using a highly collimated source of ultraviolet light originating from a high-pressure mercury arc lamp.[10]

Contact printing refers to the situation when the mask and wafer are in intimate contact during exposure: on the other hand, in proximity printing exposure takes place with a finite gap between the substrates. In practice, neither condition is completely achieved. In its chucked state, the wafer does not assume a flat surface: this limits the total wafer area that can achieve perfect contact; in addition, the resist gives off nitrogen gas during exposure, which further separates the mask and wafer.[10] During proximity printing, in the exposure phase the mask and wafer are separated by about 10 μm: this is done to reduce mask and wafer damage that results during contact. Unfortunately, the same wafer surface irregularities that prevent perfect contact also inhibit a clean separation, and it is still possible to observe damages on the mask. This situation is also aggravated by the need for some physical contact to achieve mask-to-wafer parallelism.

The advantages inherent in contact/proximity printing are the simplicity of the system and the relatively small capital investment. These techniques are capable of producing good l.0-μm features in the contact mode and approximately 4.0-μm in the

proximity mode.[10] They are capable of very high exposure rates since they incorporate a minimal number of optical elements and broadband illumination.

The usefulness of contact/proximity printing is, however, limited by many difficulties: depending on the severity of the contact and the size of each die, induced mask defects limit the mask life from ten to a few hundred exposures. As a consequence, the economics of using a disposable mask dictate the use of an inexpensive mask: this is usually a photographic emulsion, which imparts an additional limitation on practical feature size and overall yield. Moreover, the process of clamping the wafer between two substrates also distorts the wafer surface in an unpredictable and non-repeatable fashion: overlay errors as large as 1 μm are easily produced.[10] To limit penumbra effects, contact printers use a highly collimated source of illumination. The coherency tends to accentuate diffraction effects in the imagery. A practical solution is to decollimate the illumination by a few degrees, with a subsequent loss in minimum feature size.[10]

Proximity printers operate in the region of Fresnel diffraction, where the smallest achievable feature is proportional to $(\lambda y)^{1/2}$: λ is the exposing wavelength, y the mask-to-wafer separation. y can be increased without loss in resolution by decreasing the wavelength. In recent years there has been a renewed interest in proximity printing using deep UV (2000 to 2600 Å) illumination, since reducing the wavelength from 4000 to 2000 Å and doubling the mask-to-wafer separation a marked improvement in yield in provided.[10] Another benefit of proximity printing is that it provides considerable improvement in linewidth control compared to projection printing. By decreasing the wavelength, the improvement is even greater.

3.5.2 – General properties of photoresists

In order to achieve good lithographic performance, it is important to consider the properties of photoresists are as much as the properties of the exposure tool used. Photoresists can be divided into the broad classes of positive and negative resists, depending on how they respond to radiation. In a positive resist system, the exposed areas become more soluble than the unexposed regions, as seen in the example shown at the

beginning of this paragraph. Most commercial positive resists are composed by a photosensitive dissolution inhibitor, an alkaline-soluble base polymer (usually a novolac resin) and a solvent.[10] The dissolution inhibitor prevents the base polymer from dissolving in the alkaline developer: the dissolution inhibitor concentration is reduced in the selected areas that have been exposed to light, leading to an increased solubility. A second type of positive resist action takes place when a positive electron or x-ray resist is exposed to deep UV radiation: in this situation, the radiation has enough energy to cause main-chain fissions in the base polymer; the lower molecular weight in the exposed regions leads to greater solubility during development.[10]

On the other hand, negative resists become less soluble in the regions exposed to light: the cross-linking of the polymer is at the base of the mechanism that leads to this decrease in solubility and this cross-linking increases the molecular weight in the exposed areas.[10] Exclusively negative resists were used in the beginning of the development of photolithographic technique: their principal characteristic was a high degree of process latitude and they provided excellent secondary properties; unfortunately, negative resists present other features that limit their usefulness. First, in the process of development, the developer permeates both the exposed and unexposed areas, causing therefore a swelling in the resist profile: this action limits the useful feature size to about 2.0 μm.[10] Second, a finite level of background light that originates from light scattered off the projection optics will always be present when using a projection printer: with positive resists the background light simply reduces the height of the resist profile and, consequently, has little effect on the overall quality of the produced structure; with a negative resist, the effect is more serious. The background light cross-links a thin film in the top surface of the resist: this film usually becomes punctured and falls down between the features and results in a "scumming" effect. Experiments conducted to measure the effect of background light on scumming have concluded that as little as 1% scattered light can ruin the imagery of 1.0-μm lines and spaces.[10] Third, standing-wave phenomena can produce an inadequate exposure at the resist-wafer interface. If this occurs and the features are small, the developed pattern will often wash away.

3.6 – Scanning Electron Microscopy (SEM)

Albeit first developed in the early 1930's and perfected to a high degree in the late 1950's, the scanning electron microscope and scanning beam equipment based on its principle found quite lately their proper fields of application, probably due to the great impact of transmission electron microscopy in almost every field of research. The void between the transmission electron microscope and the light microscope, plus the limitations and disadvantages of each, apparently had to be more fully appreciated before SEM could find its proper place. In 1965 the scanning electron microscope became commercially available, and since then there has been a great outburst in use of this equipment as a research tool.

3.6.1 – Principles of SEM

The two major components of an SEM are the electron column and the control console (Fig. 3.9). The electron column consists of an electron gun and two or more electron lenses, which influence the paths of electrons travelling down an evacuated tube. Vacuum pumps usually create a vacuum of about 10^{-4} Pa at the base of the column. The control console consists of a cathode ray tube (CRT) viewing screen and the knobs and computer keyboard that control the electron beam.

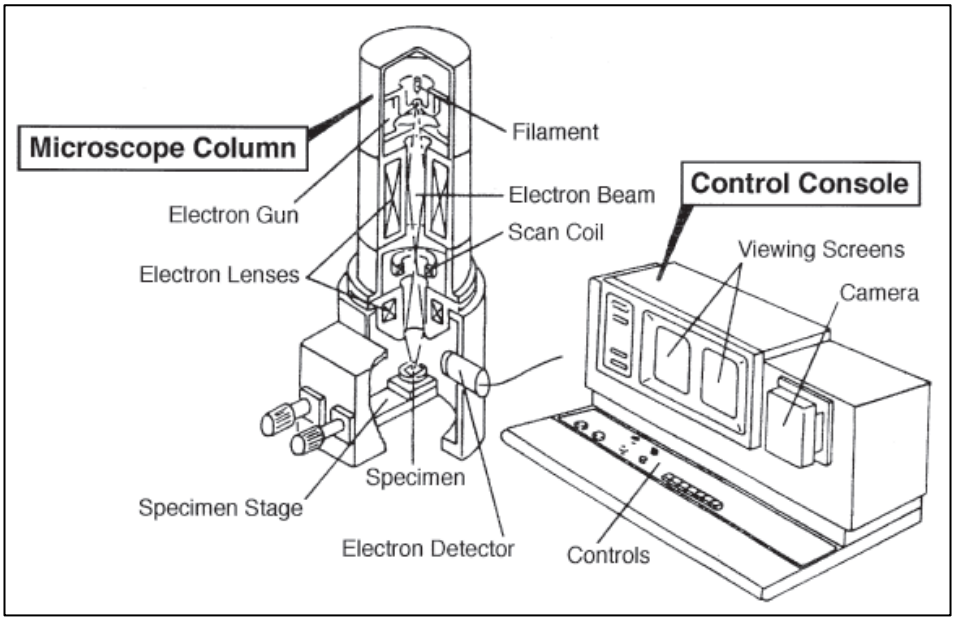

Figure 3.8 - The two major parts of the SEM, the electron column and the electronics console.[11]

The electron gun generates electrons and accelerates them to an energy in the range 0.1–30 keV (generally, operation is around 20 keV).[12] The spot size from a tungsten hairpin gun is too large to produce a sharp image unless electron lenses are used to demagnify it and place a much smaller focused electron spot on the specimen, as shown schematically in Fig. 3.10. Most SEMs can produce an electron beam at the specimen with a spot size less than 10 nm (100 Å) that contains sufficient probe current to form an acceptable image.[11] At this point, the beam arrives into the specimen chamber from the final lens and interacts with the specimen to a depth of approximately 1 μm, generating the signals used to form an image.

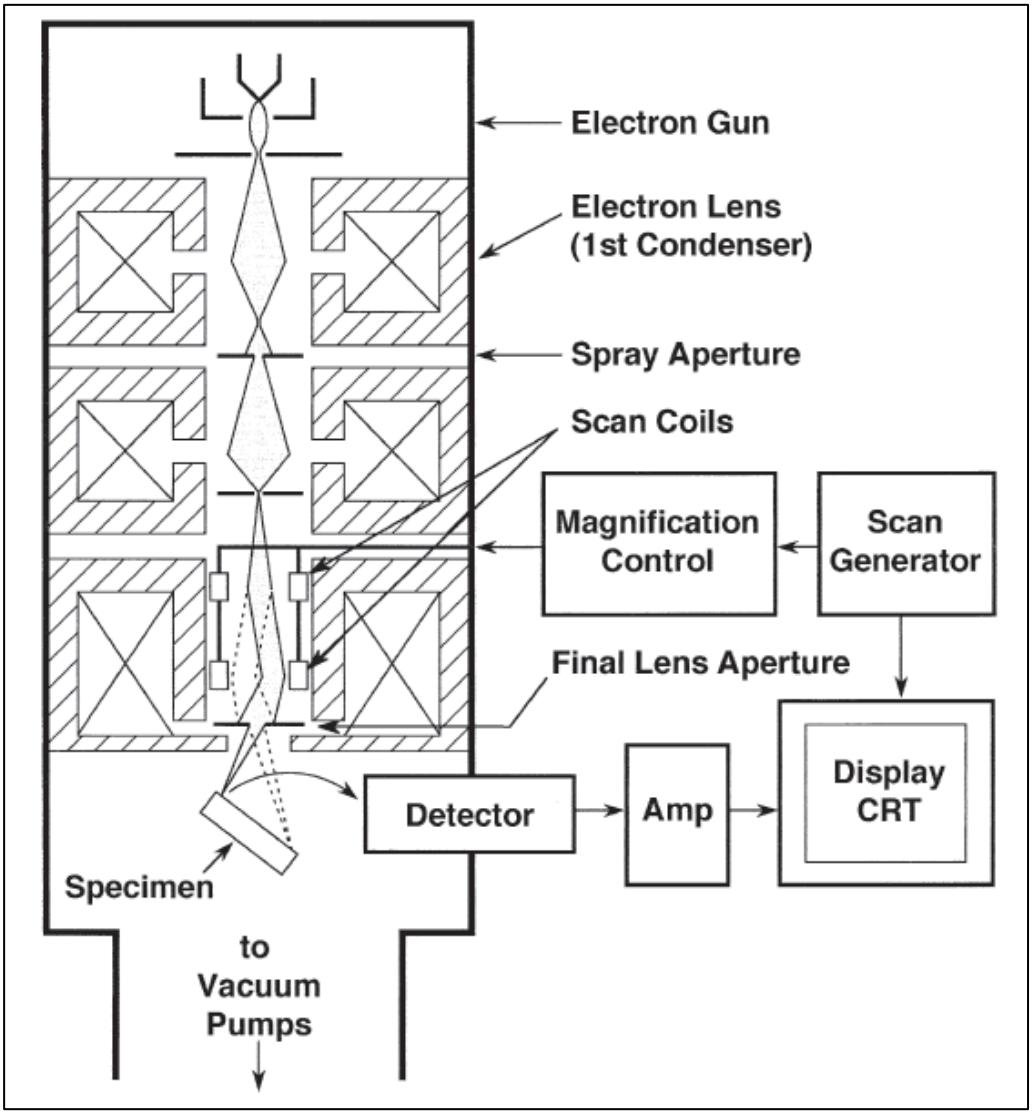

Figure 3.9 - Electron column: the electron gun, lenses, the deflection system and the electron detector are shown.[11]

The scanned image is formed point by point: the deflection system causes a spot movement at a well-defined velocity and in a well-defined, rectangular pattern of lines

(termed the "raster"). Line by line this rectangular raster is swept out, each line being built up of a large number of picture elements, each one of which is the size of the electron-spot diameter. Simultaneously, the same scan generator creates a similar raster on the viewing screen. To sweep the beam across the specimen, two pairs of electromagnetic deflection coils (scan coils) are used: the first pair of coils deflects the beam off the optical axis of the microscope and the second pair bends the beam back onto the axis at the pivot point of the scan (Fig. 3.10).

Magnification in SEM is simply the ratio of the length of the raster on the viewing screen to the corresponding length of the raster on the specimen (the ratio of the size of the two synchronous rasters). As in the other imaging systems, useful magnification is determined by resolution. In a modern SEM the magnification is automatically compensated for each working distance to assure that the indicated magnification is correct.[11] Theoretical magnifications of 10^5 are possible, but in practice about 50000 is the maximum.[12]

When the signal collected from the beam-specimen interaction varies from one location to another, contrast is involved. Many types of signal are generated as the electron beam impacts on the specimen and any of these can be displayed as an image: the signals is converted by the electronics of the detector system to point-by-point intensity changes on the viewing screen, producing an image. The two signals most often used to produce SEM images are secondary electrons (SE) and backscattered electrons (BSE).[11] The standard Everhart-Thornley (E-T) detector collects both secondary and backscattered electrons (Fig. 3.11). When a positive voltage is applied to the collector screen in front of the detector, both SE and BSE signals are collected. On the other hand, when a negative voltage is applied on the collector screen a pure BSE signal is captured, because the low-energy SEs are repelled. Electrons captured by the scintillator/photomultiplier are then amplified for display on the viewing CRT.

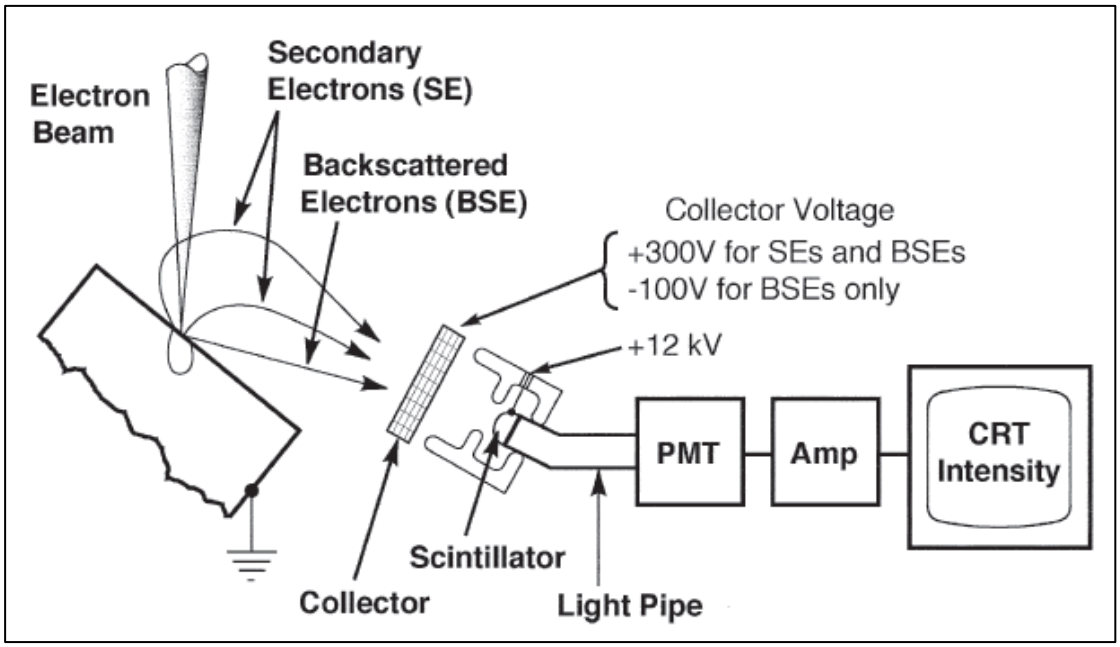

Figure 3.10 - Backscattered and secondary electron collection of these signals by the E-T detector.[11]

Older SEMs have a separate CRT for slow-scan recording of images onto photographic film or, alternatively, a video printer to produce a hard copy of the CRT image. Modern SEMs store their images in digital form in a computer for processing and printing at a later time.

The detection modes described above indicate the great versatility of the electron beam principle. However, the most used detection mode is the secondary electron mode for its greatest potential as a microscope and will be described in the next session. When secondary electrons are collected, amplified, and used to modulate the brightness of the CRT spot, a three-dimensional image of the object surface is built up.

3.6.2 – The secondary-electron detection mode

SEM finds its greatest use as a microscope in the study of solid specimen surfaces and materials with rough topography are particularly well suited for SEM investigation because of its great depth of field capabilities. This potential is primarily due to the secondary electron detection mode. There are two types of electrons leaving a surface as a consequence of interaction of the primary beam with that surface: slow-moving, low-energy (less than 50 eV) electrons, called secondaries; electrons with energies ranging from 50 eV up to the energy of the primary beam (usually about 20

keV.[12] Latter ones are called reflected electrons: because of their high energy, they travel straight paths from surface to detector, but a loss of detail may result in the image since surface irregularities may block the path. Thus, even though the reflected electron image may have high clarity, depth of field is lacking.[12]

The positive potential of the accelerating electrode causes secondary electrons to travel curved paths from surface to detector: this potential attracts the slow-moving, low-energy particles. Placement of the detector to take advantage of this results in an illuminating effect in which secondaries are gathered from areas obscured by surface irregularities: this phenomenon is the base of the great depth of field capabilities of SEM with secondary electron imaging. Secondaries arising from obscured areas are collected, and the information they carry is reproduced in the image build-up.[12]

The secondary electron detection mode has been the object of much research ever since the scanning beam principle found wide use in microscopy. Variations between the angle of incidence of the primary beam and the local normal to the surface of the specimen have great influence on secondary electron yield, a factor highly dependent on surface topography. Because of this, most objects are tilted at an angle of 15 to 45° from the horizontal, but the resultant "foreshortening" in the image or photomicrograph is not serious from the standpoint of interpretation.[12]

Two factors peculiar to secondary electron imaging are related to their action at the specimen surface. First, the image build-up gains a contribution only from secondaries arising at the specimen surface: those arising below the surface (the maximum depth of penetration is only about 100 Å) weaken resolution and make changes to contrast.[12] Second, variation in electron density of the surface material (i.e. atomic weight differences) have a very small influence on secondaries with respect to contrast formation: this is in contrast to higher energy reflected and transmitted electrons.

3.6.3 – Energy-dispersive X-ray spectroscopy

One of the first and most practical uses of the scanning beam principle resulted from image build-up using the X-rays emitted from the specimen surface. This is termed "electron-probe microanalysis", or “energy-dispersive X-ray spectroscopy”

(EDX) and is used in studying elemental composition distributions. The operating principles of a solid state detector system are illustrated in Fig. 3.12.

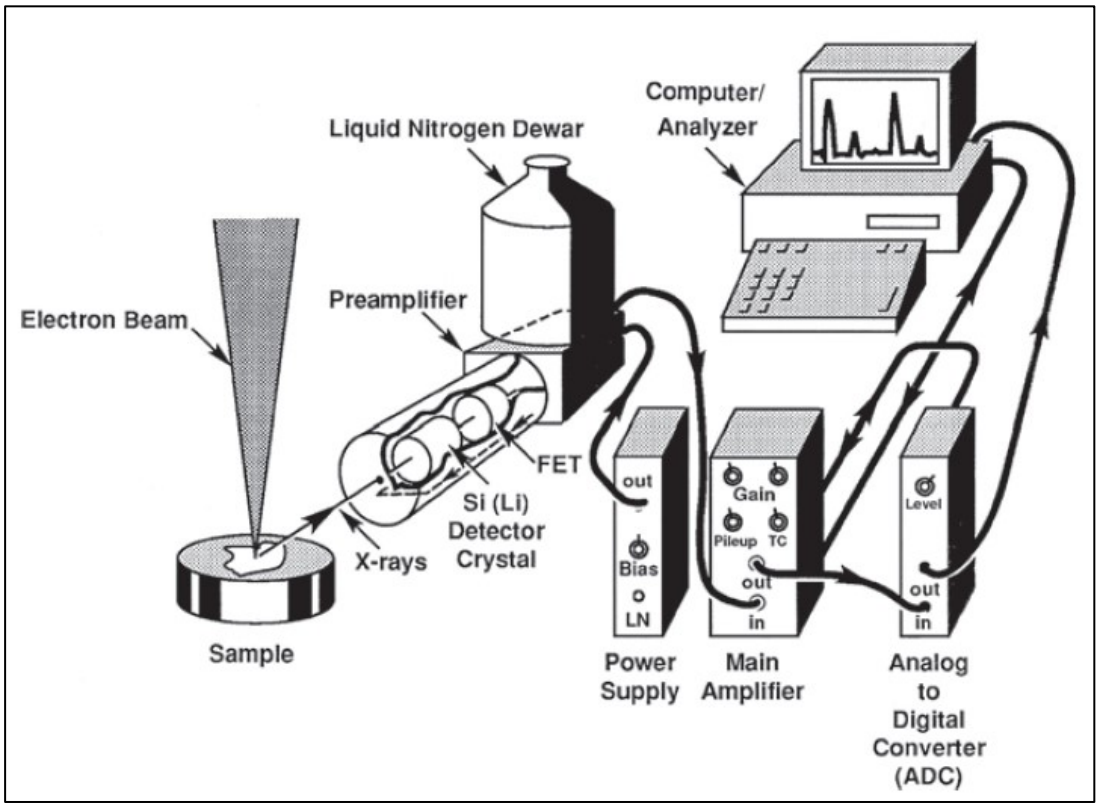

Figure 3.11 - Schematic representation of an energy-dispersive spectrometer and associated electronics.[11]

X-ray photons emitted from the sample pass through a thin window, isolating the specimen chamber environment from the detector, into a cooled, reverse-bias p-i-n (p-type, intrinsic, n-type) Si(Li) crystal. Here, absorption of each individual x-ray photon generates the ejection of a photoelectron, which gives up most of its energy to the formation of electron-hole pairs: they are swept away by the applied bias to form a charge pulse, which is then converted into a voltage pulse by a charge-to-voltage converter (preamplifier).[11] A linear amplifier further shapes and amplifies the signal, which is finally passed to a computer x-ray analyser (CXA) where the data are shown as a histogram of intensity by voltage. The contents of the CXA memory in all recent instruments either reside directly in a computer or can be transmitted to a computer for further processing, such as peak identification or quantification: the key to understanding how an EDX works is to recognize that each voltage pulse is proportional to the energy of the incoming x-ray photon. The role of the CXA is to establish this relationship and to present it in a form understandable to the operator.[11]

Bibliography

1. Chen, C.-C., Zhou, Y. & Baker, L. A. Scanning Ion Conductance Microscopy. *Annu. Rev. Anal. Chem.* **5,** 207–228 (2012).

2. Hansma, P. K., Drake, B., Marti, O., Gould, S. A. C. & Prater, C. B. The Scanning Ion-Conductance Microscope. *Science (80-.).* **243,** 641–643 (1989).

3. Takahashi, Y. *et al.* Topographic imaging of convoluted surface of live cells by scanning ion conductance microscopy in a standing approach mode. *Phys. Chem. Chem. Phys.* **12,** 10012 (2010).

4. Shevchuk, A. I. *et al.* Imaging Proteins in Membranes of Living Cells by High-Resolution Scanning Ion Conductance Microscopy. *Angew. Chemie* **118,** 2270–2274 (2006).

5. Zilko, J. L. Metal-Organic Chemical Vapor Deposition. in *Encyclopedia of Inorganic Chemistry* 151–203 (John Wiley & Sons, Ltd, 2006). doi:10.1002/0470862106.id515

6. Manasevit, H. M. Single-crystal gallium arsenide on insulating substrates. *Appl. Phys. Lett.* **12,** 156–159 (1968).

7. Stringfellow, G. B. A critical appraisal of growth mechanisms in MOVPE. *J. Cryst. Growth* **68,** 111–122 (1984).

8. Brinker, C. J. *et al.* Fundamentals of sol-gel dip coating. *Thin Solid Films* **201,** 97–108 (1991).

9. Bard, A. J. & Faulkner, L. R. *Electrochemical Methods - Fundamentals and Applications*. *John Wiley & Sons, Inc.* (2001). doi:10.1016/B978-0-12-381373-2.00056-9

10. Michael C. King. *VLSI Electronics - Microstructure Science, Vol. 1 Chapt. 2: Principles of Optical Lithography*. *Academic Press Ltd.* (1990).

11. Goldstein, J. I. *et al. Scanning Electron Microscopy and X-Ray Microanalysis*. *Springer Science + Business Media New York* (2003).

12. Collett, B. M. Scanning electron microscopy: A review and report of research in wood science. *Wood Fiber Sci.* **2,** 113–133 (1970).

4 – Results and discussion

4.1 – Pipette design and fabrication

As already said in the previous chapter, the operative principle of SICM relies on ionic conductance of the solution inside the glass pipette. In this paragraph, design and fabrication of the integrated SICM-EC device are described in detail; a further look will guide us through the characterisation of this electrodes and their integration inside the SIC microscope.

4.1.1 – From capillary to pipette

Literature on SICM-EC technique presents two schools of thought: the first one uses a θ-pipette, with one of the barrels filled with various materials, from pristine carbon to iridium oxide-coated carbon, and this filled barrel acts as chemical detector while the "free" barrel is used for recording the topography of the sample and for precise spatial positioning. The second one uses electrodes fabricated on the side of the glass pipette, with different techniques (thermal deposition, electron-beam evaporation), different shapes (crescent, concentric circle) and different insulators (electrophoretic paint, Al_2O_3, polymeric insulators), leaving the opening clear and allowing ionic solution flow through. Our strategy focused on the second path, therefore borosilicate capillaries were used as raw material. Our choice was based on the assumption that manufacturing a single barrel glass pipette is much easier and more reproducible: less breaks occur due to the thicker wall of the single barrel pipette.

To transform capillaries into pipettes, a heater capillary puller was used. Several parameters and working conditions were tested until we were able to obtain a reproducible fabrication procedure, with pipettes having an opening diameter of ≈ 25 μm (Fig. 4.1).

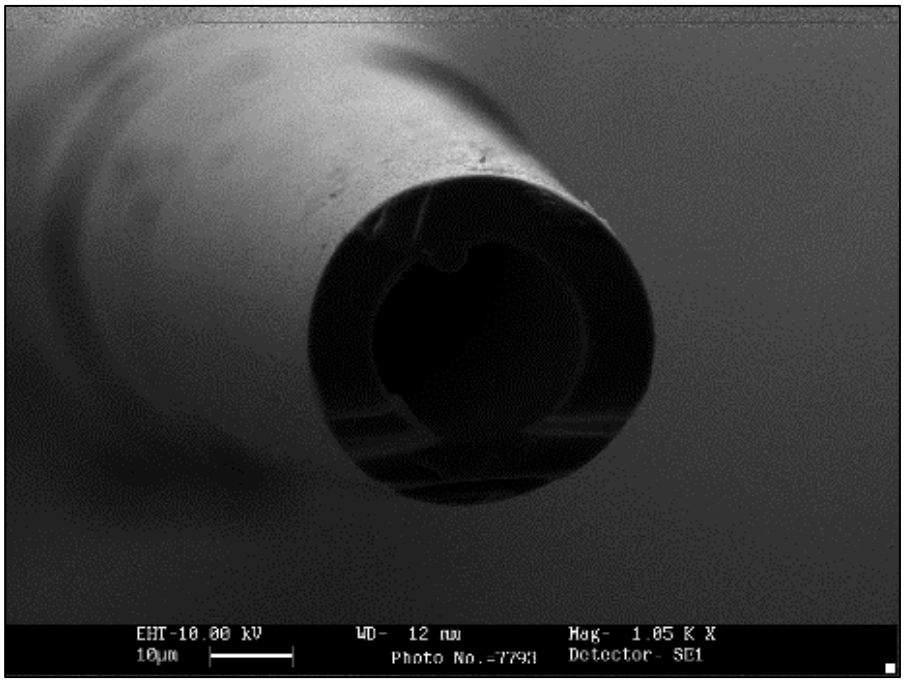

Figure 4.1 - SEM image of pipette opening.

4.1.2 – MOCVD coating

After tuning the fabrication procedure of glass pipettes, next step was the deposition of a conductive layer on the outer side of the pipette. First, it was necessary to choose a material suitable to perform as WE in the integrated device: our choice went on platinum after bibliographic research on this topic, thanks to its chemical affinity to hydrogen (for direct sensing applications: cf. chapter 2 and section 4.2.1), its excellent conductivity and its resistivity to corrosion and oxidation as a noble metal. Moreover, the most used material as electrode for pH sensing is IrO_2, which is more expensive: therefore, Pt stood as a valid and more convenient alternative.

Literature offered many options for the deposition procedure of Pt; MOCVD was chosen for its peculiar property, which is the generation of uniform and homogeneous metallic films. Furthermore, platinum-based precursors for MOCVD were a way cheaper option respect to other technique, e.g. Pt target for magnetron sputtering deposition. We managed to produce a final and functional protocol of deposition, using $Pt(acac)_2$ as precursor, H_2O as co-reagent and N_2 and O_2 as carrier for $Pt(acac)_2$ and H_2O, respectively: Pt layer grew at 285 °C and 100 Pa. With this procedure, a 150 nm

thick, metallic electrode on the outer side of the glass pipette was obtained. This protocol showed good conductivity of the layer and reproducible results (Fig. 4.2).

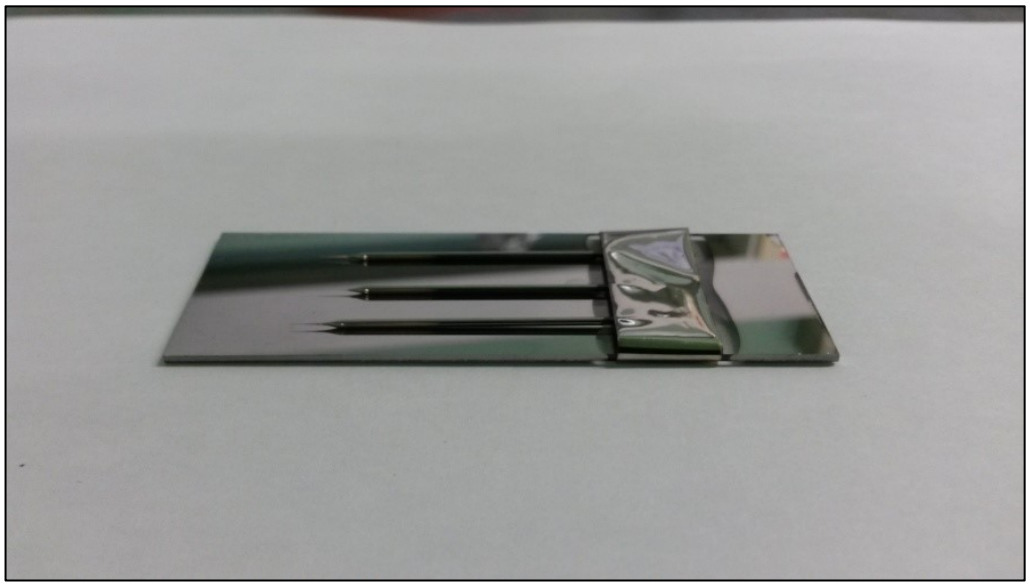

Figure 4.2 - Pt-covered pipettes after MOCVD.

MOCVD is a technique that affects the entire surface that is exposed to vapour: this means not only the outer surface of the pipette, but also the walls of the reactor and the inner surface of the pipette. While the deposition of Pt on the walls of the reactor did not affect the final product, the presence of platinum in the inner surface of the pipette could be an issue for electrochemical measurement, since the electrodical surface involved in the electrochemical process was different from what is expected to be (it is important to remember that in operative conditions the pipette is immerged, therefore there is solution inside the pipette). To avoid this problem, after deposition the pipette is filled with aqua regia, a mixture of nitric acid and hydrochloric acid in 1:3 molar ratio well known for dissolving noble metals, to eliminate the inner platinum film.

4.1.3 – Insulating layer

In order to achieve maximum resolution for the simultaneous topography and electrochemical measurements, just a small area of the coated surface must be in contact with the electrolyte: it was then necessary to study, realise and test a fully insulating coating.

Different coating materials were deposited on a gold substrate covered by a dip-coating procedure and tested. A previous CV in $K_3Fe(CN)_6$ 10 mM and 0.1 M KCl solutions was conducted on the pure-gold surface, then coating was performed and finally a new CV was done. Results showed a significant drop in the signal intensity, meaning that the analysed surface was insulated. First attempts saw the sol-gel deposition of traditional inorganic insulants, such as Al_2O_3 and SiO_2, but the performed experiments were unsuccessful, even increasing the thickness of the coating film by using the dip-coating procedure multiple times: the gold substrate was not sufficiently insulated, giving unsatisfactory results (Fig. 4.3).

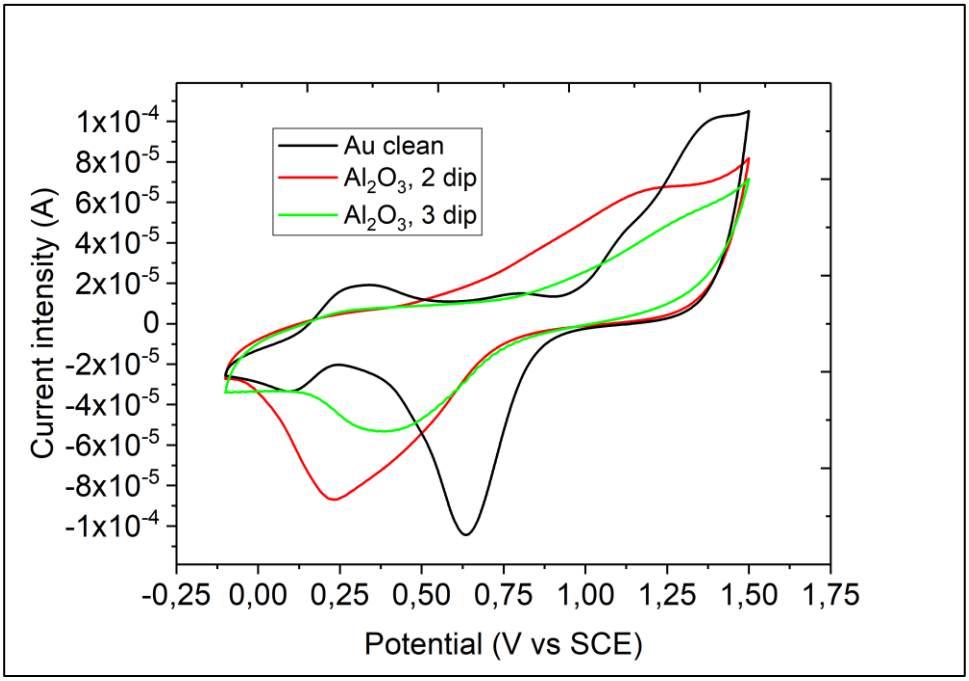

Figure 4.3 - Characterisation of allumina coating over Au substrate in $K_3Fe(CN)_6$ 10 mM.

In addition, ALD was tested for the deposition of alumina, but subsequent characterisation of the sample stated that the layer was not insulating. The problem was solved using an industrial spray paint (Fig. 4.4). The selected product provided excellent results, with a signal intensity lying just above the noise region (about 10^{-9} A) thus keeping the integrity of the gold coating (Fig. 4.5). Moreover, it is very cheap.

Figure 4.4 - Insulating industrial spray paint.

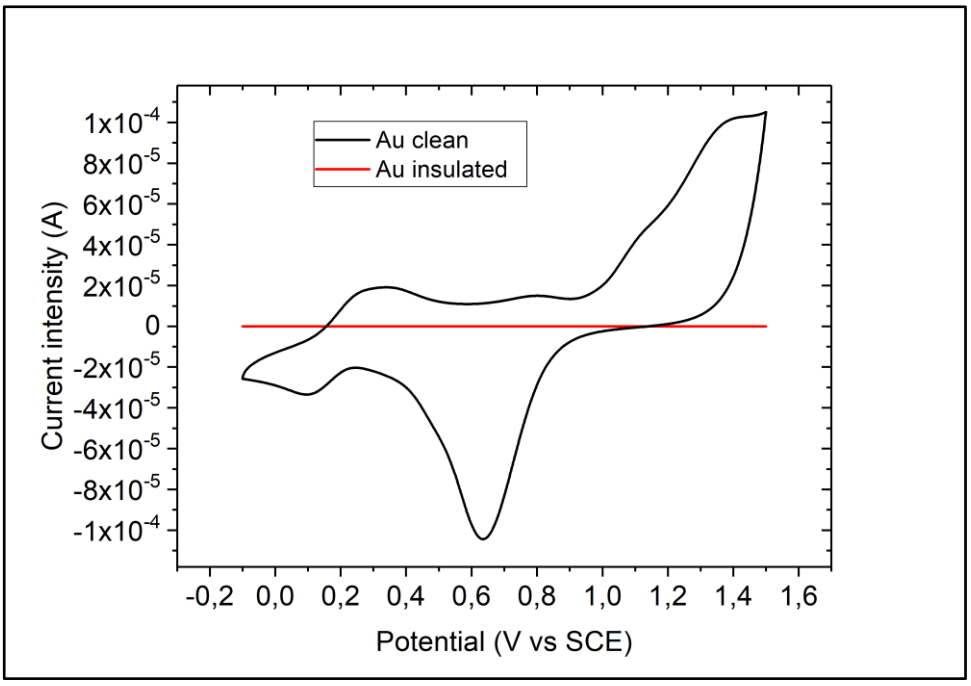

Figure 4.5 - Characterisation of insulating coating in $K_3Fe(CN)_6$ 10 mM. Overlapped CVs show the insulating performance of the industrial spray paint.

Since one of the main advantages of the integrated EC-SICM technique is the high spatial and lateral resolution, just a very small conductive region of the WE should be exposed to the solution: the conductive layer ring-shaped that surrounds the pipette tip. In order to achieve this goal, it was necessary to "re-open" the pipette from the insulating layer, so to expose the metallic film and remove any hindrance at the

opening of the pipette for the control of the Z-axis movement. As seen in paragraph 2.6, current literature on this topic suggested the use of FIB but we looked for a different, more economically affordable way. We tested several solvents to eliminate the polymeric resin via dissolution, from acetone to dichloromethane etc., and the best one turned out to be xylene. Fig. 4.6 resumes the fabrication process.

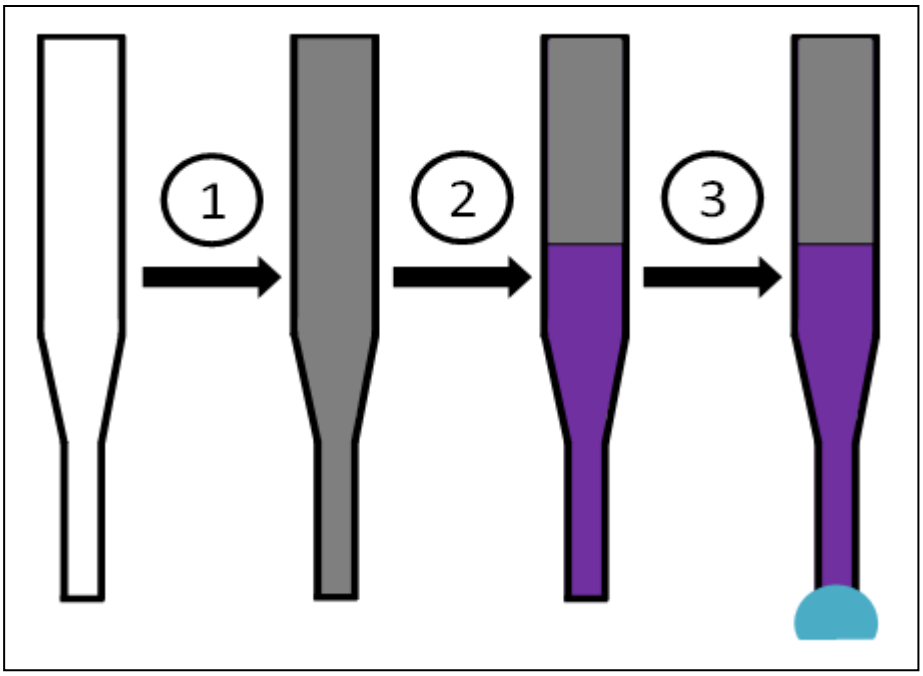

Figure 4.6 - Design and production of integrated probes. ① Pt deposition via MOCVD; ② insulation via dip coating; ③ tip opening with xylene.

Based on these results, we fixed a manufacturing protocol for pipette insulating coating and re-opening. The insulating layer was deposited by dip coating the lower half of the pipette inside the liquid resin: after 30 minutes, the pipette was removed from the resin and heated at 60 °C for 30 minutes in order to dry the polymeric resin and to increase cross-linking, obtaining a more homogeneous coating. Profilometric measurement allowed estimating the thickness of the coating in 25-40 µm (Fig. 4.7). After this procedure, the coated pipette was ready for re-opening: the very tip was put in contact with a small drop of xylene using a micromanipulator for 60 minutes, so to be sure to dissolute all the polymerised resin from the ring-shaped platinum layer.

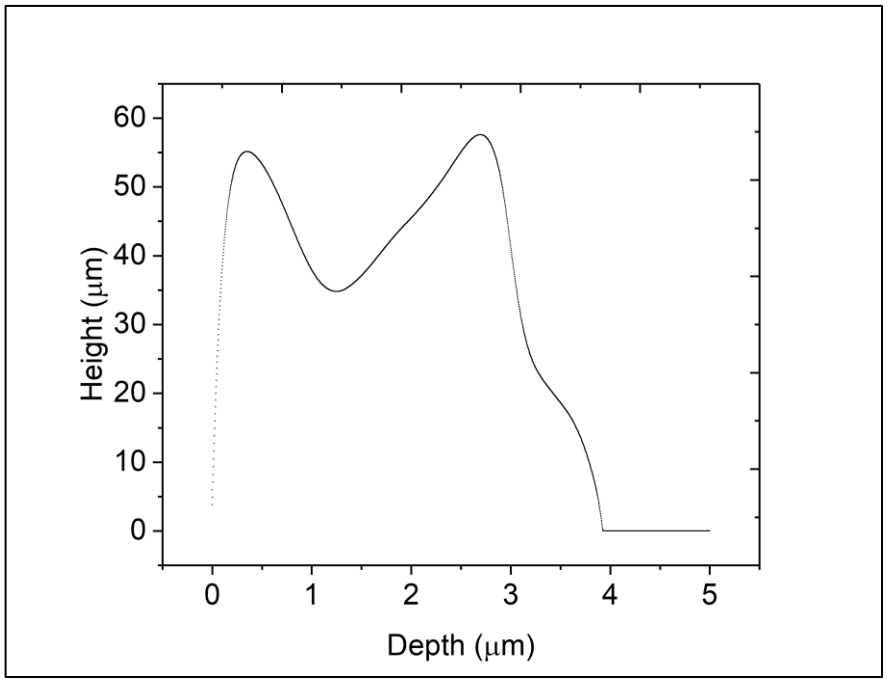

Figure 4.7 - Profilometric characterisation of insulating coating. The re-opening procedure is considered to dissolve ≈ 1 μm of coating.

4.1.4 – Characterisation

After the insulation step, the coated pipette was electrochemically characterised in order to verify its range of application for detection of chemical species. At first we pointed out a methodology for the realization of a calibration curve for each pipette: the intent was to use an electrochemical standard specie like potassium hexacyanoferrate(III), with a well-known and reversible one-electron redox mechanism which undergoes at tabulated potentials, in growing concentrations (from 2 to 10 mM). For this first set of experiments, we used SCE as RE, a Pt ring as CE and another Pt wire as WE instead of pipettes to prevent eventual damages to the insulating coating or the Pt layer: the wire was chosen for its cylindrical geometry, very similar to that of the pipette. Anyway, the obtained results were not useful since the increasing concentration did not provided a corresponding increase in the intensity of the electrochemical signal (Fig. 4.8).

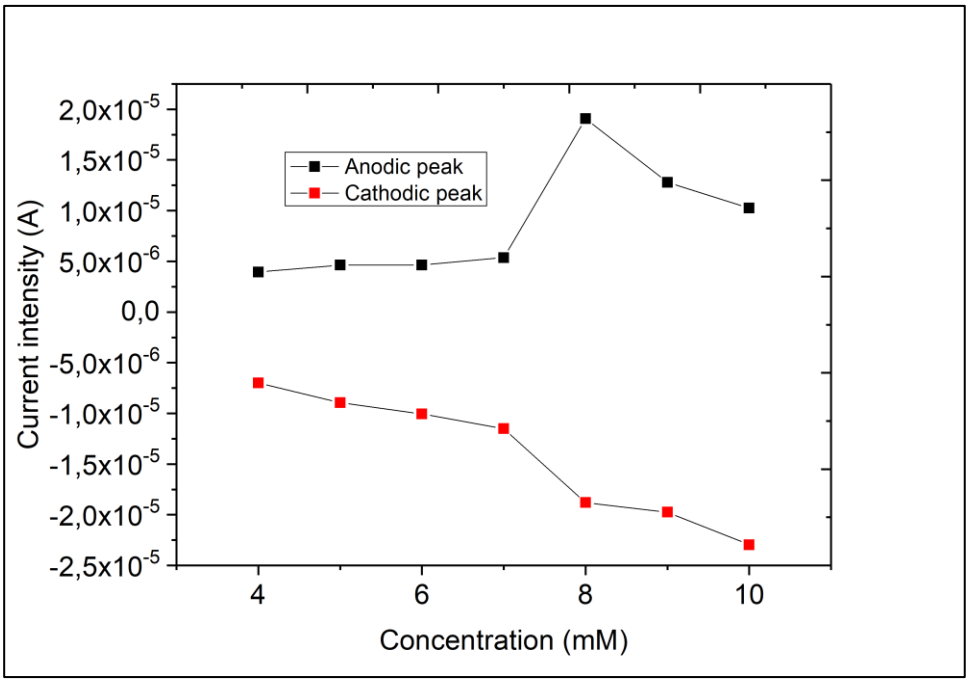

Figure 4.8 - Current vs Concentration plot of Pt wire: in black current intensity of anodic peak of CVs, in red current intensity of cathodic peak. Standard specie is $K_3Fe(CN)_6$.

This behaviour was considered as the consequence of a chemisorption of the standard on the platinum surface, creating a thin film that killed the sensibility of the electrode, as confirmed by literature studies. A first solution was to clean mechanically the WE after each measurement to remove that film, but the application of cleaning procedure to the Pt-coated pipette ruined the electrode, detaching the platinum coating from the glass substrate (Fig. 4.9).

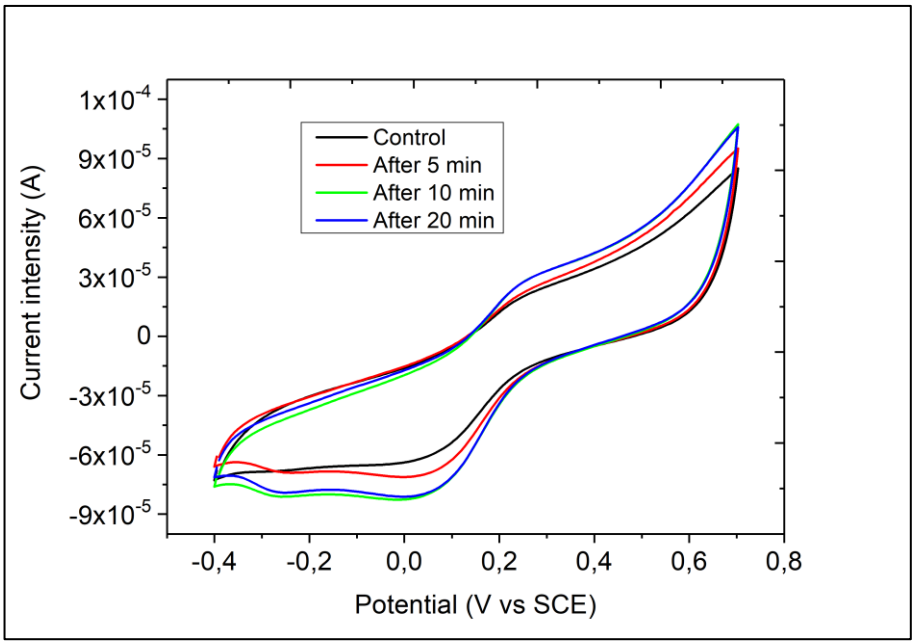

Figure 4.9 - Effect of sonication in acetone to remove the poisonous layer from platinum. Even if the surface seems cleaner from CV analysis, the Pt layer was detached from glass substrate.

For this reason, we changed chemical standard to hexaammineruthenium(III) chloride $Ru(NH_3)_6Cl_3$, which presented all the useful features of the previous one without the highlighted drawbacks. Preliminary tests were carried out in order to optimize characterisation parameters. In particular, Fig. 4.10 shows the effect of the riequilibration step on the response of the electrode: using 5 minutes as riequilibration time for the WE decreases the variability of data.

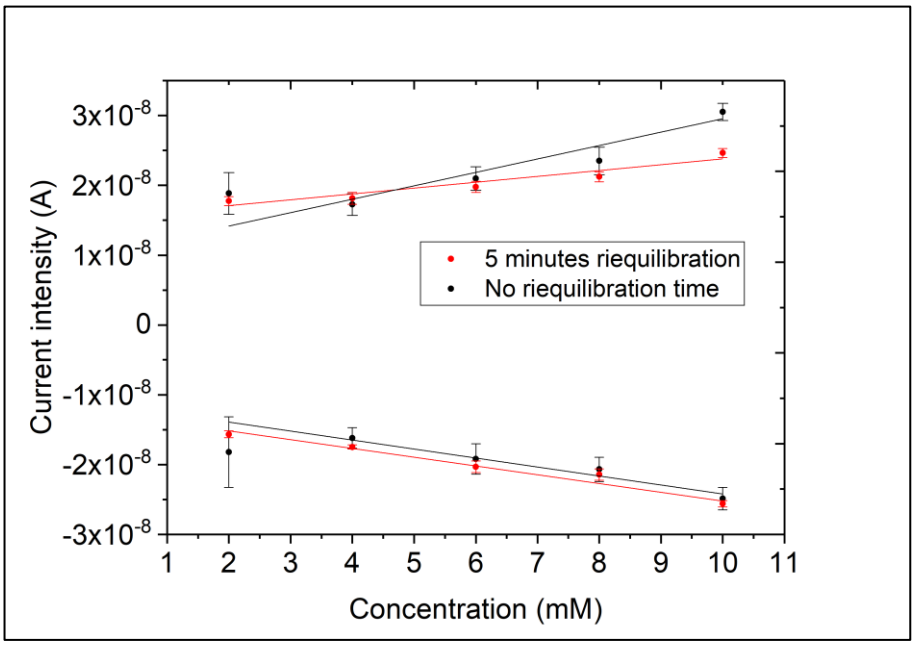

Figure 4.10 - Effect of riequilibration time on WE response.

Then, CVs were performed in 0.1 M KCl solutions, with standard concentration ranging from 2 to 10 mM $Ru(NH_3)_6Cl_3$, at 20 mV/s, biasing potential from - 450 mV to 55 mV vs SCE and using Pt wire as CE. We performed five measurements for each concentration value; each measurement consisted of two cycles and the results of the second cycle were used for subsequent data analysis. Current values of anodic and cathodic peaks were plotted versus the standard concentration to verify the linear trend theoretically predicted (Fig. 4.11).

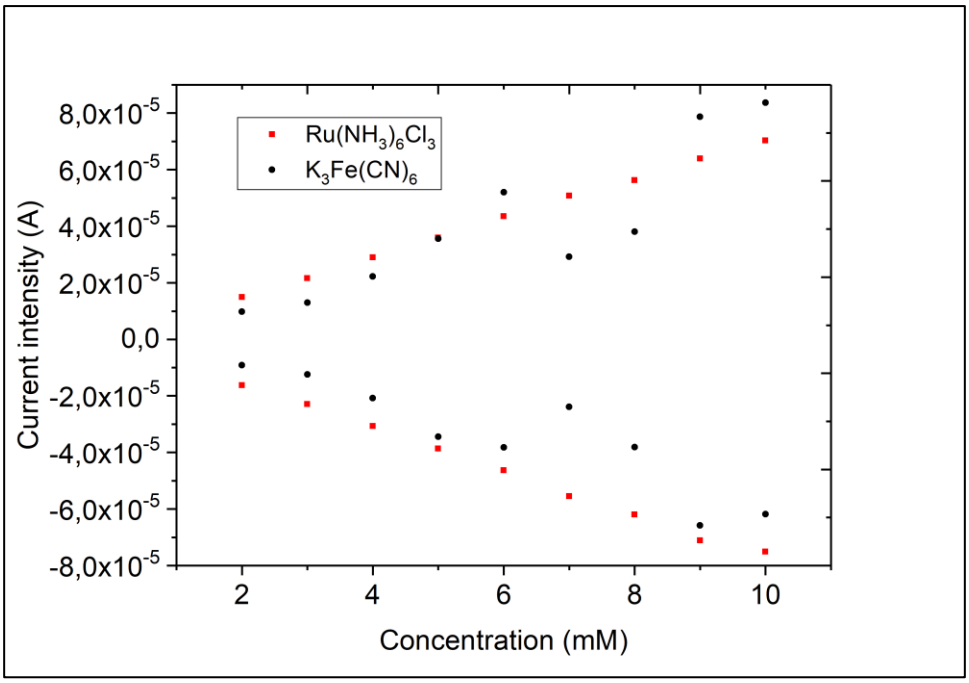

Figure 4.11 - Comparison between $K_3Fe(CN)_6$ and $Ru(NH_3)_6Cl_3$.

After the verification of the suitability of our standard, we moved to the characterisation of insulated pipettes maintaining the same operative parameters used for the platinum wire. In Fig. 4.12 we show an example of this Current vs Concentration plot.

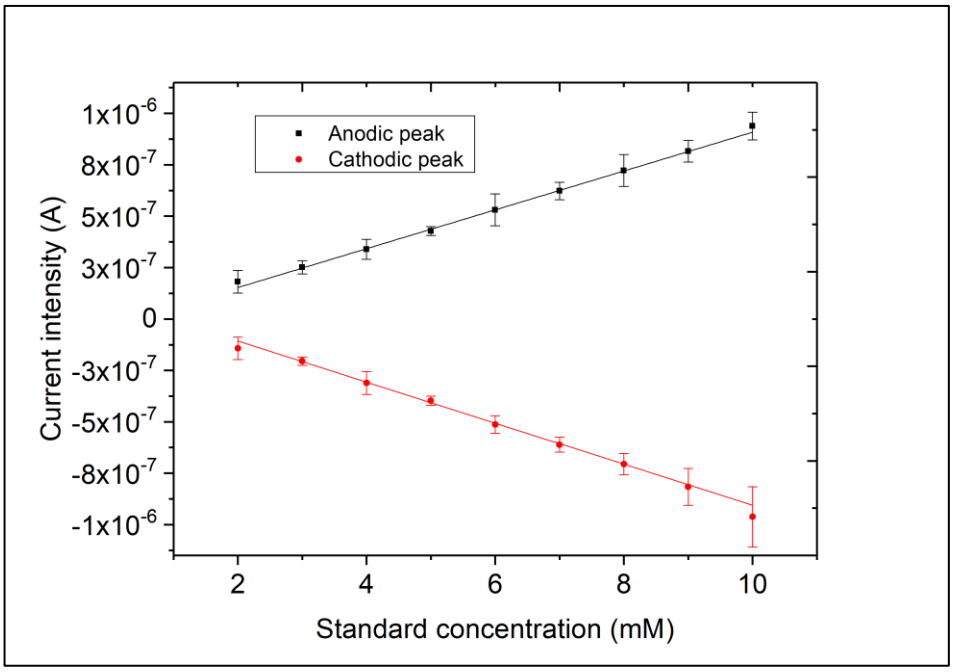

Figure 4.12 - Current vs Concentration plot of an insulated pipette: in black current intensity of anodic peak of CVs, in red current intensity of cathodic peak. Standard specie is $Ru(NH_3)_6Cl_3$.

Fig. 4.13 shows Current vs Concentration plot related to different pipettes. It was clearly visible that each plot was different from the others, even if the current intensity values for each pipette were in the same order of magnitude: our assumption is therefore that every pipette was "self-standing" and must be calibrated before use, with dip coating as critical cause in the non-replicability of the fabrication procedure.

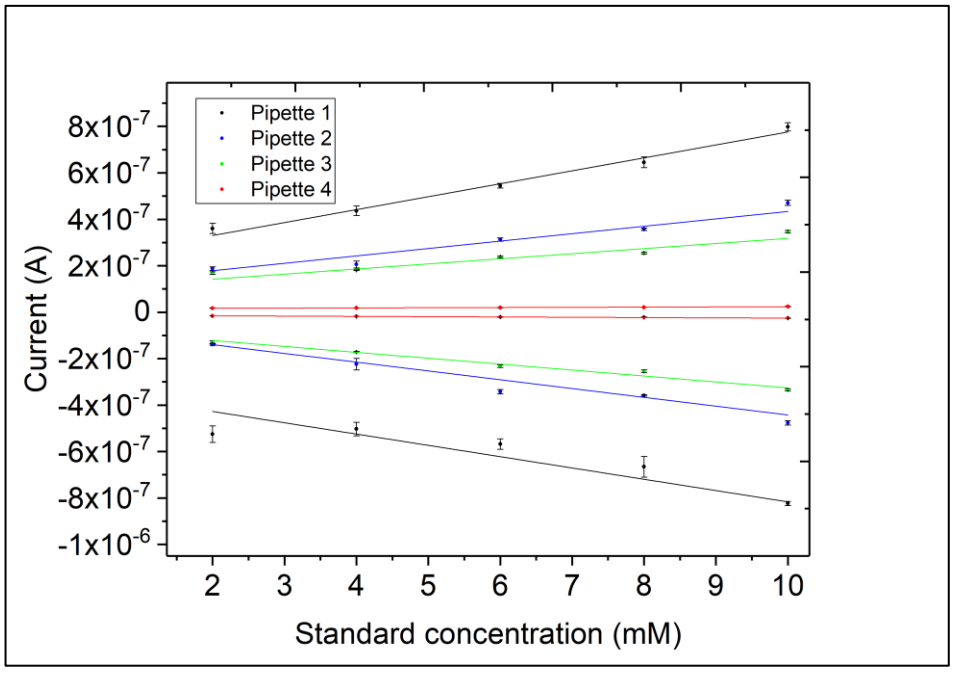

Figure 4.13 - Overlap of Current vs Concentration plot for 4 different pipettes: pipette 1 (black), pipette 2 (blue), pipette 3 (green), pipette 4 (red).

To confirm this hypothesis, we started a campaign of experiments aimed to compare the behaviour of different pipettes, both "used" and regenerated ones. The regeneration process consists in the complete dissolution of the insulating coating in xylene followed by a new dip coating and re-opening according to the standard protocol. This procedure was performed in the last months of the three-year project, to maximise the aging effect and to compare the behaviour of pipettes before and after regeneration. For this reason, the comparison was based on OCP vs pH curves, described in section 4.2.2, but data are shown in this section to conclude the characterisation part. Fig. 4.14 shows the compared OCP vs pH curves of a used pipette before and after regeneration. Data related to regeneration were performed 9 months later than the previous ones. As we can see, regeneration did not affect the probe sensitivity towards different pH. This confirmed the important role of Pt as reliable and long lasting electrodic material, with dip coating as the main cause in different behaviour of different pipettes.

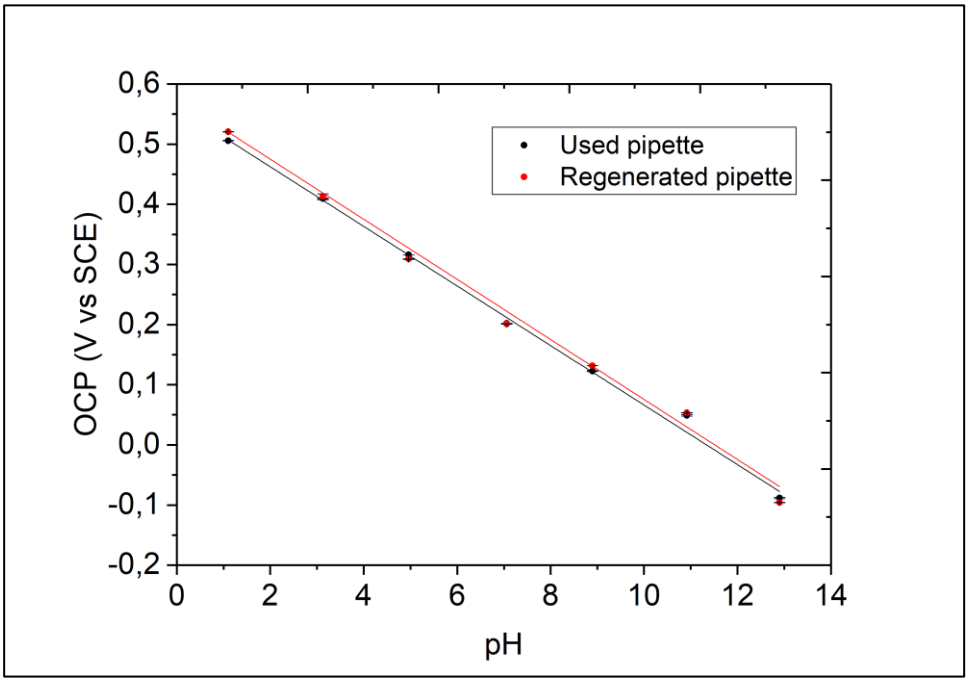

Figure 4.14 – Overlap of OCP vs pH trend for a single pipette. In black are shown data before regeneration, in red data recorded after 9 months of use and after regeneration process.

4.1.5 – Integration in SICM

All previous characterisation part was carried out inside a standard three-electrode electrochemical cell: however, since all potentiometric pH-sensing experiments were scheduled to be performed within the SICM-integrated set-up, we replicated the

same characterisation experiments inside this integrated set-up, maintaining Pt wire as CE. The redox standard used was the same of previous CVs with the same range of concentrations, but this time we worked inside a 35x10 mm plastic petri dish instead of a 50 mL electrochemical cell. Due to short operative volume and reduced spaces of this new set-up, the SCE was substituted with an AgCl coated Ag wire, a quasi-reference electrode (QRE): this innovation allowed to preform experiments in reduced spaces without using porous membranes or Luggin capillary, with just a calibration of the QRE vs a SCE as a preliminary step. Connection with potentiostat was provided using crocodile clips for RE and CE and a hook connector for WE that grips to the uninsulated upper part of the metallic film (Fig. 4.15).

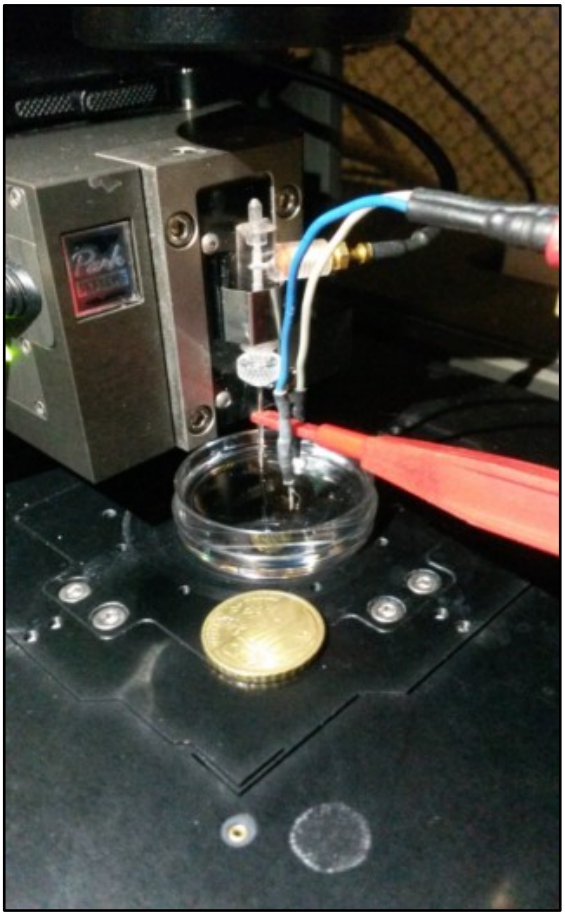

Figure 4.15 - Integrated SICM-EC set-up: RE (blue) is AgCl coated Ag wire; CE (grey) is Pt wire; WE is coated pipette linked to potentiostat with an hook (red). (10 eurocent coin for scale).

As shown in Fig. 4.16, the new SICM-integrated set-up confirms the results obtained with previous, standard three-electrode set-up, though there was an increase in the experimental error: this increase was probably due to electrical issues in the con-

nection of electrodes to potentiostat. What above written is confirmed by a good overlap of CVs (Fig. 4.17). Therefore, we can state that a good grade of integration of the new device inside the SICM-modified set-up was achieved.

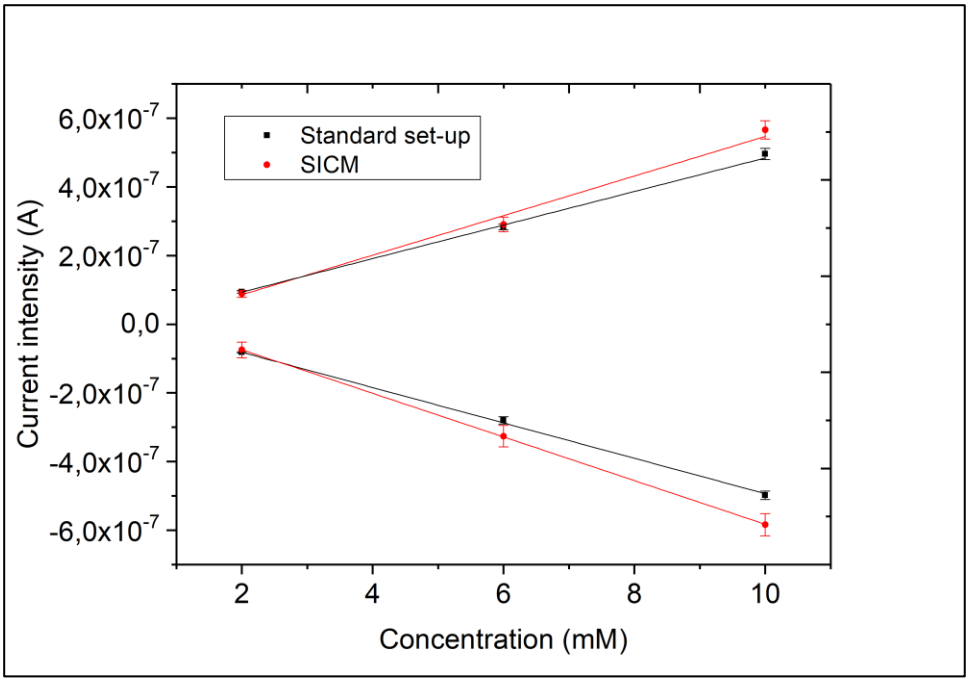

Figure 4.16 - Overlap of Current vs Concentration plot for a single pipette using standard 3-electrodes set-up (black) and integrated SICM set-up (red).

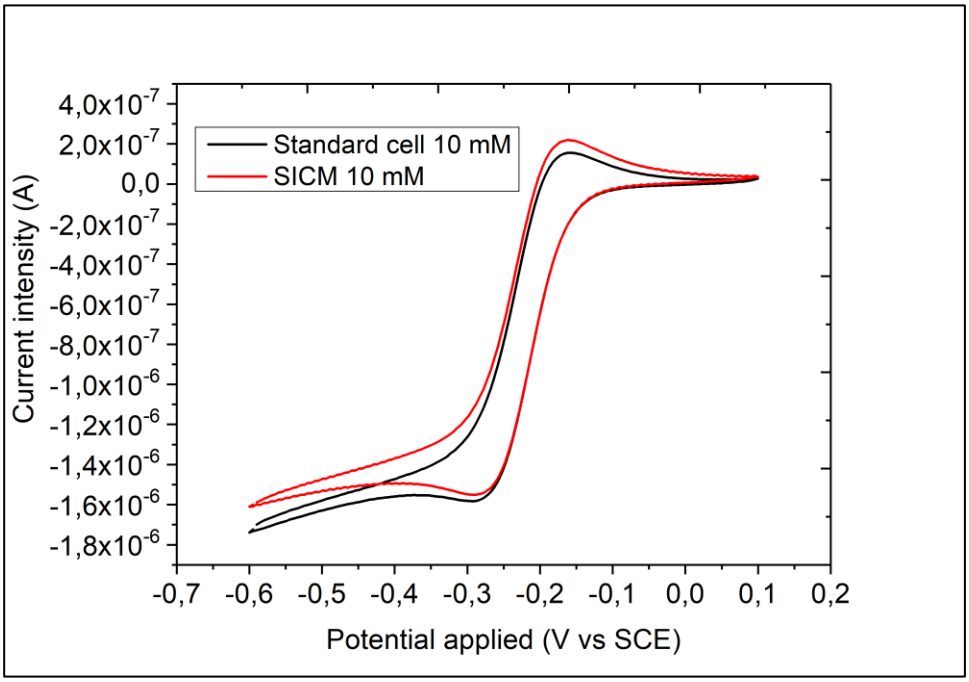

Figure 4.17 - Overlap of CVs in 10 mM $Ru(NH_3)_6Cl_3$: insulated pipette was tested with standard set-up (black) and integrated SICM set-up (red).

4.2 – Approach to sensing

When creating a new device for scientific analysis, a strict control of fabrication and characterisation is mandatory. When the necessary requirements had been satisfied, it was time to move on testing the sensing power of our device. In this paragraph, we describe the sensing experiments performed and we illustrate the results obtained.

4.2.1 – Direct sensing

As stated above, the SICM-EC probe was ready to be tested. At first a direct approach was applied, with the intent of measuring the current derived from the direct oxidation of molecular hydrogen to H^+ ions: several experiments were performed in different aqueous media, including PBS 0.1 M, H_2SO_4 0.5 M and K_2SO_4 0.5 M, and the potential window of analysis ranged from - 200 mV to 1400 mV vs SCE. These experiments featured CV analysis on a single solution: as it is; saturated with H_2; stripped with inert gas (Ar); stripped & saturated; saturated, stripped & saturated. This procedure was useful to see if the stripping step was effective and, most of all, if there was an oxidation peak disappearing after stripping that could be unequivocally labelled to hydrogen oxidation reaction. Hydrogen was introduced into solution in two different ways, by bubbling pure H_2 into the solution and by producing it *in situ* by electrolysis. In this way it was possible to evaluate the presence of possible contaminations or false positive signals during the sensing.

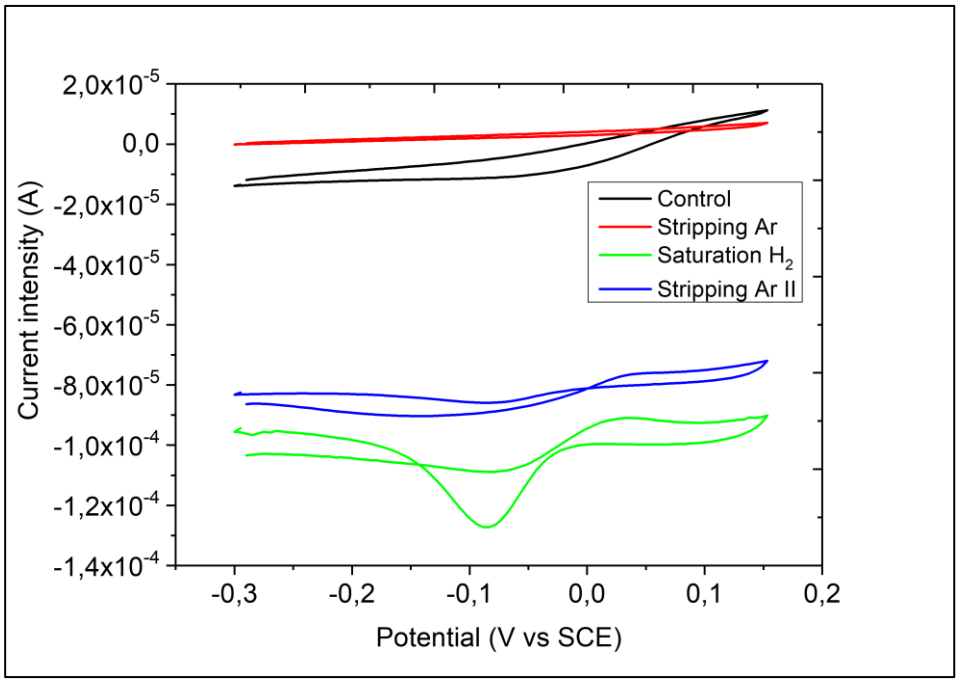

Figure 4.18 - Overlap of CVs in 0.1 M PBS. The control solution (black) is stripped with Ar (red), then electrolysis is performed in situ (green) for 30 minutes to reach saturation and finally the solution is stripped again with Ar (blue). WE is Pt wire, RE is SCE and CE is Pt wire.

Fig. 4.18 shows CVs performed in 0.1 M PBS; hydrogen was produced *in situ* via electrolysis. At first, looking at this graph we supposed to find at about - 100 mV a peak assignable to hydrogen dissolved in solution, maybe related to a reduction reaction helped by H_2. To verify this hypothesis, we performed experiments with pure molecular hydrogen provided by a cylinder and the results are shown in Fig. 4.19. Moreover, to inhibit hydrogen dissociation into H^+ ions, we changed solution to H_2SO_4 1 N.

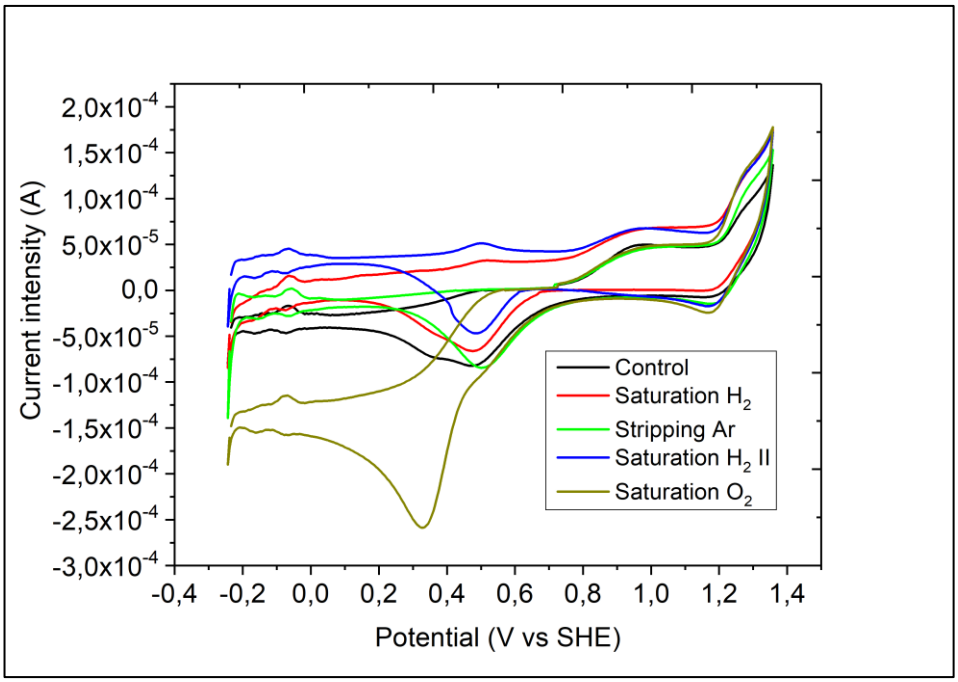

Figure 4.19 - Overlap of CVs in H_2SO_4 1 N. The control solution (black) is saturated with H_2 from the cylinder (red), then the solution is stripped with Ar (green), then saturated again with H_2 from the cylinder (blue). Finally, the solution in saturated with O_2 from the cylinder (gold). WE is Pt wire, RE is SCE and CE is Pt wire.

As we can see, previous peak (now at 350 mV due to pH change) not only was barely affected from saturation with hydrogen, but also after stripping with inert gas and subsequent re-saturation with H_2 there was no change in the intensity of this signal. For this reason, the hypothesis of a role of H_2 in this faradic contribution was denied. Then, we saturated again the solution but with O_2 from cylinder: the dramatic increase in the 350 mV peak told us that this peak is related to a reduction reaction of molecular hydrogen, probably the formation of hydrogen peroxide in acid environment ($O_2 + 2H^+ + 2e^- \rightarrow H_2O_2$). Oxygen was present in the experiment described in Fig. 4.18 due to the *in situ* gas production: if electrolysis is performed to generate H_2 at the WE, at the CE O_2 will be generated as well, affecting results which we would expected from theoretical basis.

Anyway, these experiments were useful since they allowed us to identify four peaks directly related to H_2, in particular to the phenomena of adsorption and desorption of hydrogen on Pt surface, and two more related to formation and reduction of Pt oxides.[1] Unfortunately, this information was not useful for our purposes. The adsorption/desorption peaks described above were present also in stripped solution, in which the flow of inert gas was supposed to carry away any gaseous specie dissolved. So, they were not related to the effective presence of introduced molecular hydrogen, since

these peaks were known to be related to H_2 electrolitically produced *in situ* and immediately adsorbed (and then desorbed) on the surface. Moreover, previous works[1] stated that the presence of introduced hydrogen gas could affect the formation and dissolution peaks of platinum oxides. Since the absorption and desorption of gas molecules on a solid surface was known to be a surface-dependent phenomenon, and since the electrodically active surface involved was small (about 10^{-4} cm^2), this kind of electrochemical influence to the Pt oxidation and reduction peaks was barely observable (Fig. 4.20).

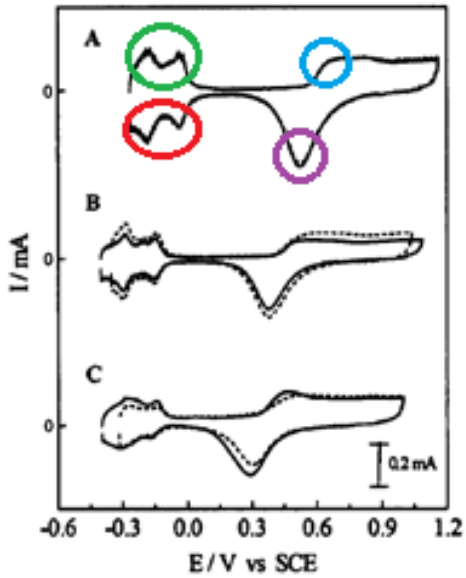

Fig. 1. Cyclic voltammograms obtained for the bare Pt (—) and Pt/PE (···) electrodes in (A) 0.5 M H_2SO_4, (B) 0.05 M H_2SO_4 + 0.45 M K_2SO_4, and (C) 0.50 M K_2SO_4 solutions saturated with N_2.

Figure 4.20 - Adsorption (red) and desorption (green) of H_2; formation (blue) and reduction (purple) of Pt oxides.

4.2.2 – Indirect sensing via OCP

A new approach was therefore necessary: since the direct approach was not useful to get short-term results, we shifted to an indirect detection. During the electrolysis of water, the following reactions occur at the cathode (reduction) and at the anode (oxidation):

$$2\,H_2O(l) + 2e^- \rightarrow H_2(g) + 2\,OH^-(aq)$$

$$4\,OH^-(aq) \rightarrow O_2(g) + 2\,H_2O(l) + 4\,e^-$$

These equations show how at the gas-evolving electrodes there are OH^- consumption and production phenomena, which involves necessarily a change in pH at the surroundings of the electrode. Previous works[2] stated the influence of pH gradients in fuel cells efficiency and described the maximum distance of this effect from the electrodical surface: our goal was therefore to see if our electrode was eligible for pH-sensing applications and if there was a Nernstian response to pH change. We assumed that a change in local pH should have led to a change in charge distribution at the electrodical surface, therefore we should have experienced a change in open circuit potential (OCP) at the WE as well. To verify experimentally this assumption, we proceeded with OCP measurements in buffered solutions with different pH. This calibration was carried out using SCE as RE and Pt wire as CE, in 0.1 M KCl solutions, pH adjusted with 1 M potassium hydroxide and 1 M hydrochloric acid: however, these solutions were not suitable for the creation of a standard calibration method since their pH was not constant and gave results with high standard deviation (Fig. 4.21).

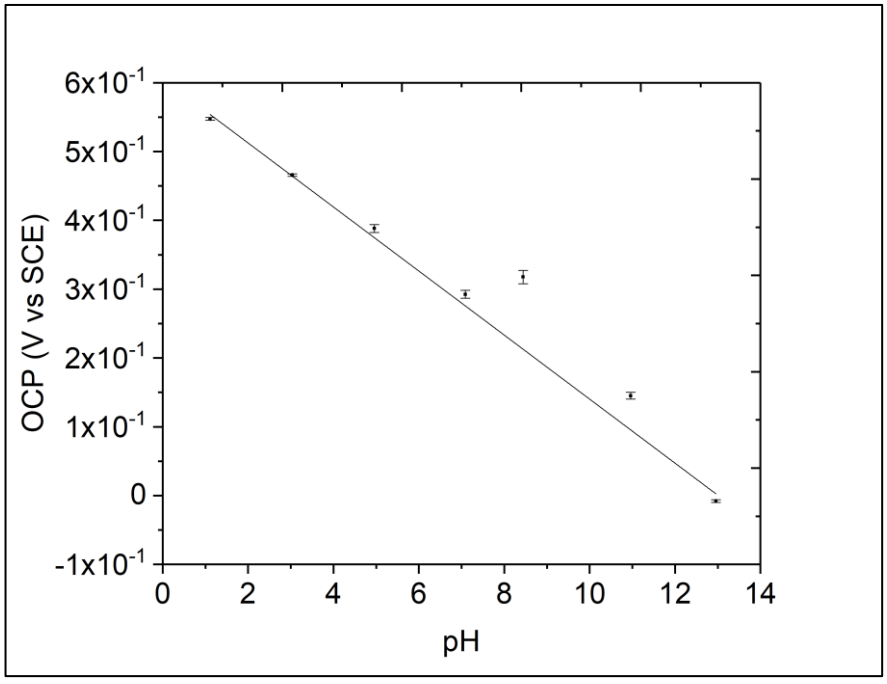

Figure 4.21 - Calibration of OCP response to change in pH without using pH buffer, ranging from pH 1 to 13.

For this reason, we created buffer solutions with 25.0 mM sodium diphosphate / 3.0 mM sodium orthoborate / 6.7 mM sodium citrate / 0.1 M KCl solutions and pH was adjusted with 1 M KOH and 1 M HCl. From the experience of characterisation with $Ru(NH_3)_6Cl_3$, before each OCP measurement the electrode was kept in contact

with solution for five minutes to have a stable and more affordable signal and we performed five measurements for each pH value. Final calibration curve OCP vs pH is shown in Fig. 4.22: a linear response of OCP vs pH with near-Nernstian slopes (- 52 mV/pH) over a pH range of 1-13 was obtained. The slope obtained was probably related to the material used as WE (Pt) that was not as suitable for pH sensing as other materials (e.g. IrO_2), therefore this trend implied a probe calibration prior to pH sensing.

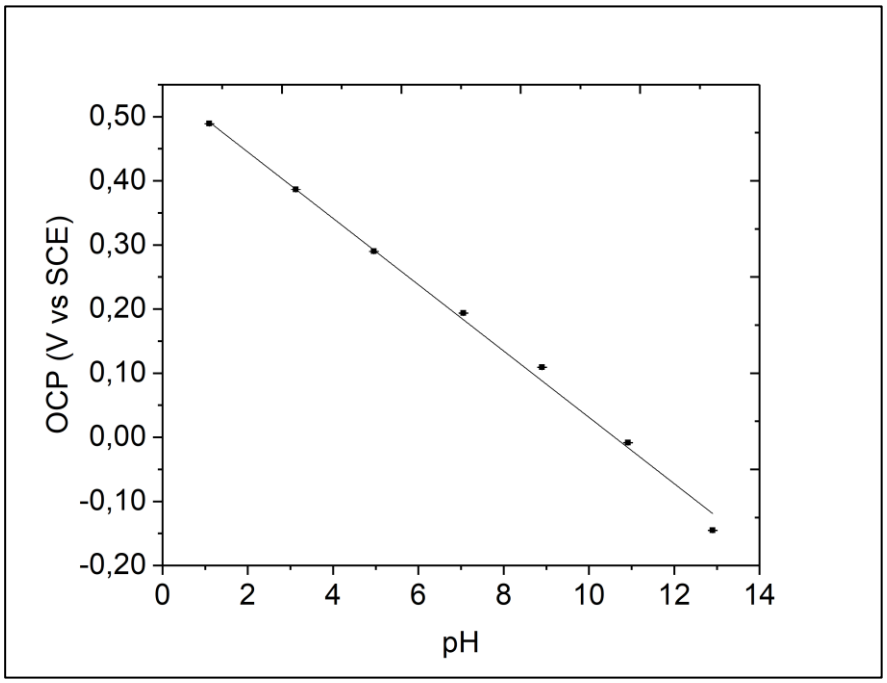

Figure 4.22 - Calibration of the OCP response to change in pH using different pH buffered solutions, ranging from pH 1 to 13.

Anyway, it was still necessary to confirm the assumption of a change in OCP of the probe as consequence of water splitting reaction. To verify the promising behavior of the data previously obtained into operative conditions, we performed the following experiment as a first approach to pH sensing. We took a soda lime microscope glass slide and half-covered it with a 150 nm thick Au layer by magnetron sputtering (a 10 nm layer of Ti was previously deposited on glass in order to have a better adhesion of the gold layer to the substrate). Then, we put this slide in the SICM-integrated set-up and connected the gold-coated layer to potentiostat as WE: a Pt wire was used as CE. As previously, for the sensing set-up of the experiment we used AgCl coated Ag wire as QRE and Pt wire as CE. According to previous literature works on microfabrication of electrodes for water splitting, we submerged the glass slide into 1 N H_2SO_4 and

applied a potential of 1755 mV vs SCE so to evolve O_2 gas: we measured OCP before and after electrolysis for both sides (coated and uncoated) with the probe placed 100 µm over the sample surface. Results obtained on each side before application of electrolysis potential were coherent within themselves, while the registered values after electrolysis over the two sides were different from each other. In particular, OCP measured after electrolysis over the pristine glass side was comparable with the values registered before, while over the gold-coated side OCP measured after electrolysis was much different (about 350 mV) from the one measured before bias application but in few seconds OCP tended to settle back to the initial value (Fig. 4.23).

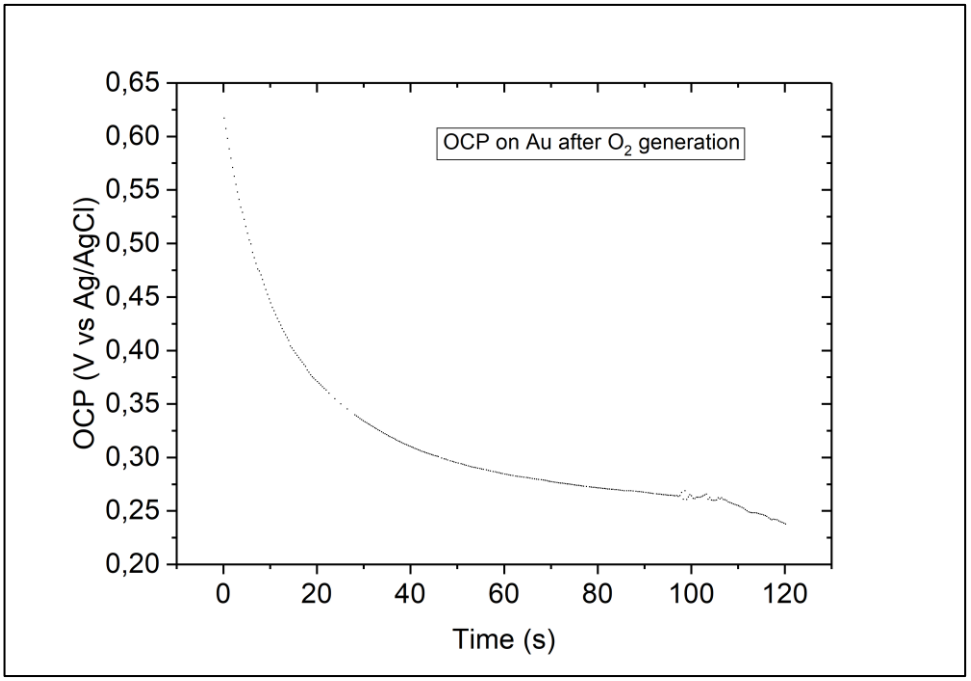

Figure 4.23 - OCP trend measured over Au-coated glass slide in 1 N H_2SO_4 solution after O_2 generation.

During electrolysis the pH around the gold electrode was different from the pH of the bulk solution; therefore once the oxygen evolution process was interrupted, the environment close to the electrode surface tended to equilibrate with the bulk solution, causing a change in pH and so forth for OCP at the sensing electrode. Moreover, starting value of OCP in Fig. 4.23 was much higher than final value, implying that corresponding pH was much more acid than bulk value as consequence of OH^- consumption.

4.2.3 – Microelectrodes: characteristics and production

As we proceeded with the work, it was important to maintain the focus on the final goal of the project: to develop a tool for EC analysis of microstructured devices at local scale. Thus, after successfully creating a certification protocol for recording OCP vs pH curves and confirming the correlation between OCP change and water splitting reaction, we started designing and fabricating a microstructured electrode for hydrogen/oxygen evolution, so to provide spatial information on the behavior of OCP before, during and after the electrolytic water splitting.

We created the microelectrode pattern on a soda lime microscope glass slide (25 mm x 25 mm x 1 mm) using photolitographic technique. We studied the design of a chrome photomask in order to fabricate four arrays of three microelectrodes (Fig. 4.24) that features different dimensions (from 100 to 250 µm) and different separation width (from 100 to 250 µm).

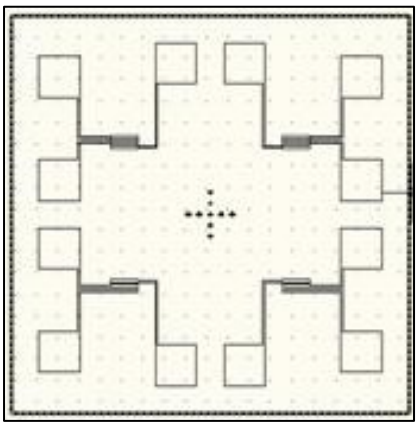

Figure 4.24 - Design of array of microelectrodes. Four arrays of three microelectrodes 100 µm wide, separated by 100 µm.

We used SU-8-2005 as photoresist and PGMEA as developer, and then we sputtered a 10 nm thick film of titanium as adhesion layer, followed by a 150 nm gold layer: as we can see from Fig. 4.25, the Au layer has no superficial cracks.

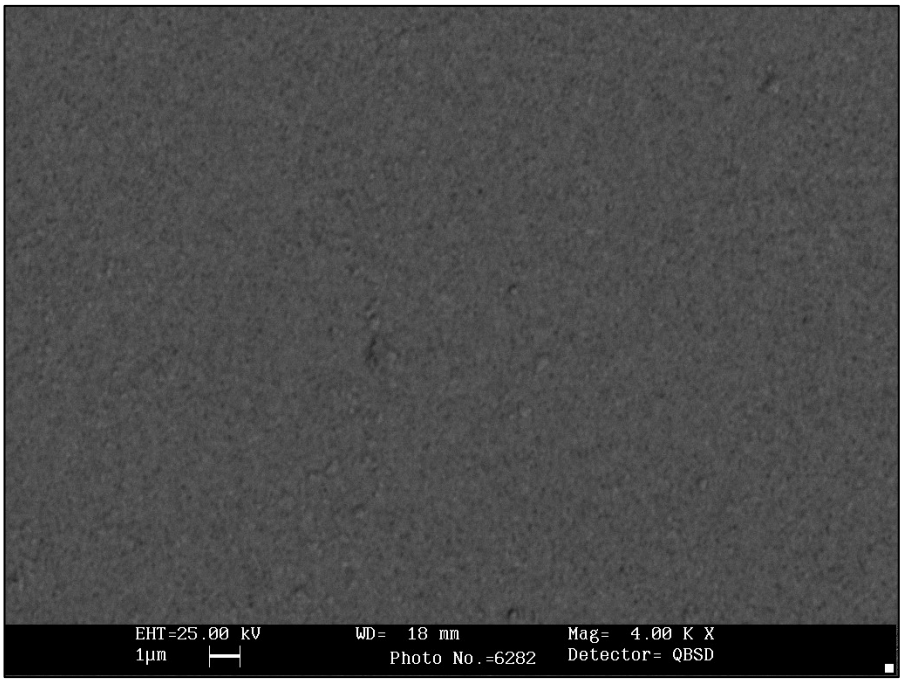

Figure 4.25 - SEM image of Au microelectrodes.

To reveal the pattern and remove the polymerized SU-8, we used SU-8 remover. Therefore, we electrochemically cleaned the Au microelectrodes by cycling between 200 and 1450 mV vs Ag/AgCl at 25 mV/s in 1 N H_2SO_4.[3] After cleaning, our effort were focused on obtaining platinum-coated electrodes suitable for both H_2 and O_2 evolution. At first we chose to follow a recent literature work recipe[3] for electrochemical platinisation using 3 wt. % $H_2PtCl_6 \cdot 6H_2O$ + 0.03 % wt. lead acetate solution and applying a potential of 500 mV vs Ag/AgCl for 30 s. Results obtained were not satisfying since we were not able to deposit a coherent, homogeneous Pt layer over the Au substrate: in fact, we observed the progressive disintegration of the micropattern by applying the desired potential. We were then forced to conduct studies and experiments on the formulation of a customised deposition procedure, based on different previous literature.[4] First step was performing a CV in the solution containing the platinum precursor (hexachloroplatinic acid) in a range from - 300 to 1300 mV vs Ag/AgCl to unequivocally identify a reduction potential for platinum deposition, that was found at - 100 mV (Fig. 4.26).

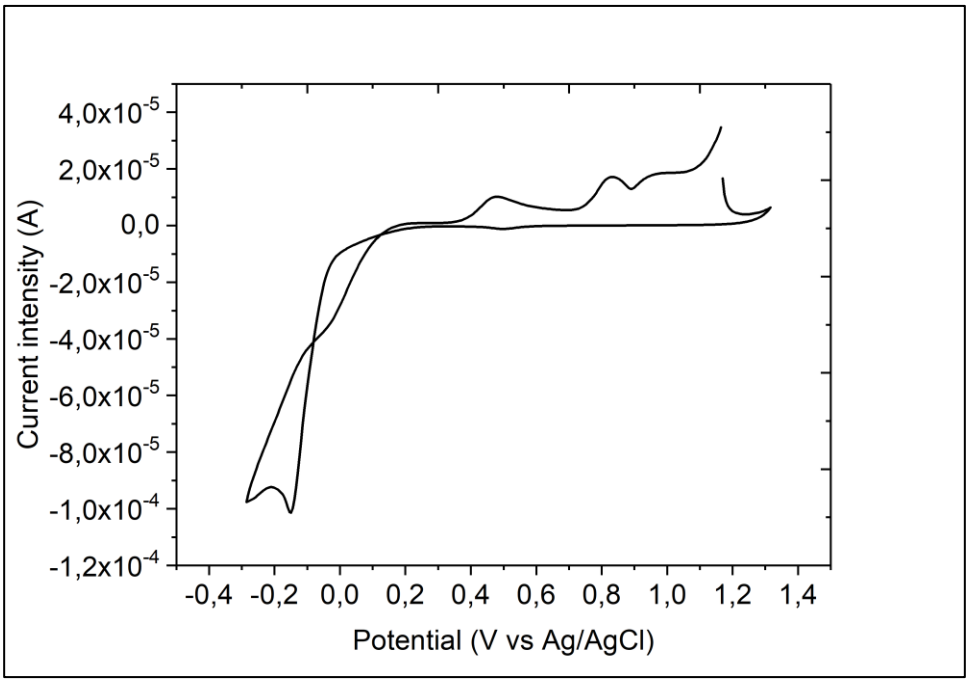

Figure 4.26 - CV over Au microelectrodes in 3 wt. % $H_2PtCl_6 \cdot 6H_2O$ + 0.03 % wt. lead acetate solution.

To confirm this hypothesis, we performed a series of CVs in that potential range (Fig. 4.27) and the results obtained show the appearance of peaks clearly assignable to the increasing presence of platinum (as seen in section 4.2.1).

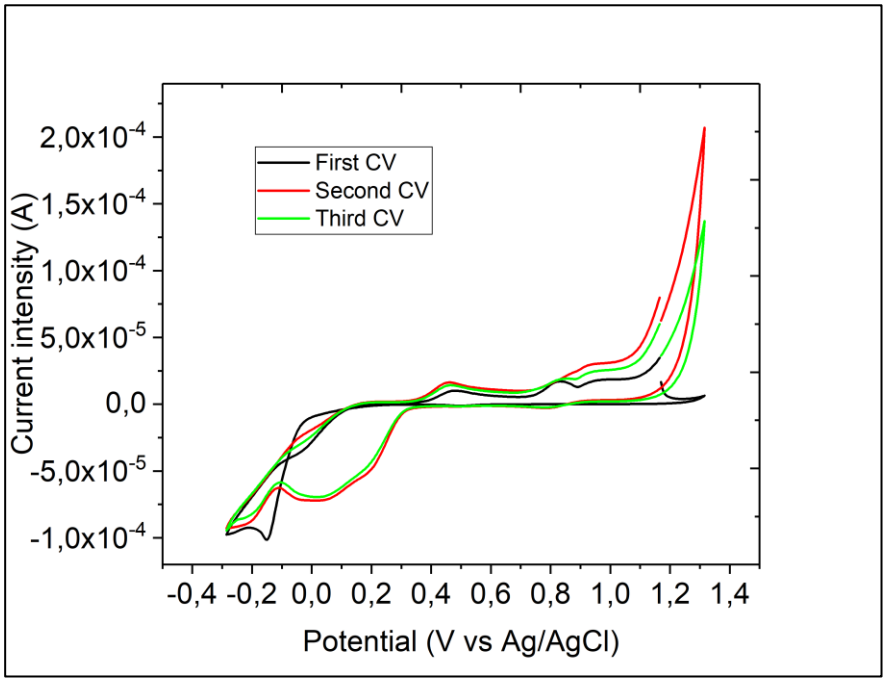

Figure 4.27 - Serie of CVs over Au microelectrodes in 3 wt. % $H_2PtCl_6 \cdot 6H_2O$ + 0.03 % wt. lead acetate solution.

After the deposition step, we thoroughly rinsed the electrodes with Milli-Q water and electrochemically cleaned them by cycling from – 400 to 1200 mV vs SCE at 50 mV/s in 1 N H_2SO_4.[3]

4.2.4 – OCP over microelectrodes

When the microfabrication of Pt microeletrodes procedure was satisfactory developed, we were ready to test our device on the challenging field of pH sensing at local scale. Several experiments were carried with H_2 and O_2 evolution, in various aqueous media and at different buffered pH. The experimental condition of previous tests were adopted, so to compare the data with the results of the preliminary experiment on the macro substrate.

Sensing set-up was the same of previous experiments, while the gas-evolving part of the experiment was modified (Fig. 4.28). In fact, the Pt/Au microelectrodes were connected to the potentiostat through connective tape (Fig. 4.29): the array of electrodes provided the WE and the CE, both platinised.

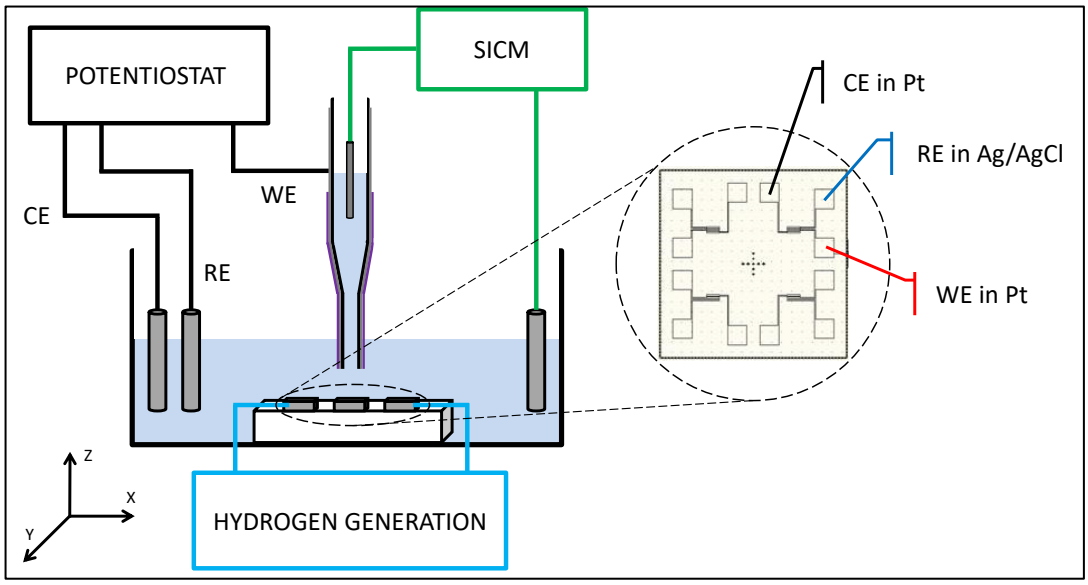

Figure 4.28 - Global overview of the experimental set-up.

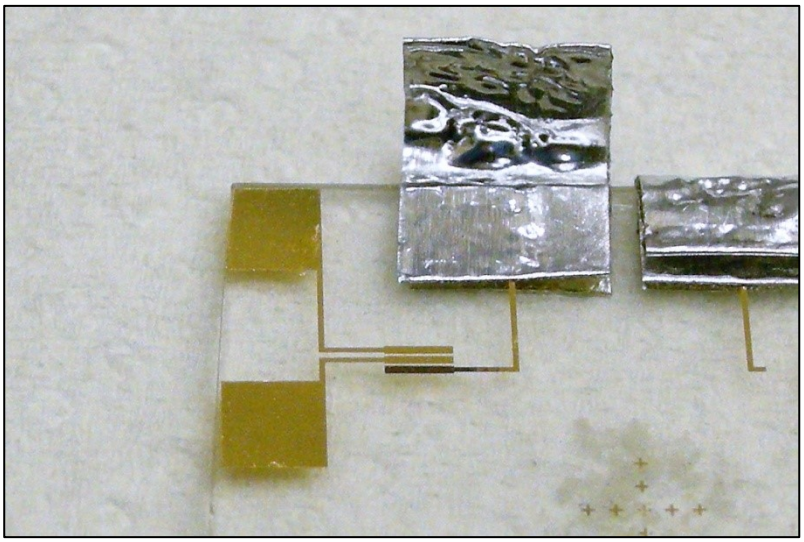

Figure 4.29 - Array of platinized microelectrodes.

The working "cell" was no longer the standard one or the petri dish, but it was made out of a silicon gasket (diameter 2.5 cm) that covered both CE and WE; in this gasket, filled with selected solution, the wires and pipette constituting sensing set-up (WE, RE and CE) are plunged.

At first, we chose to switch from acid to basic solution for oxygen detection to promote the O_2 evolution process, so we performed electrolysis in a carbonate-bicarbonate (CB) buffer (0.25 M, pH 10.1) applying 1224 mV vs SCE at WE.

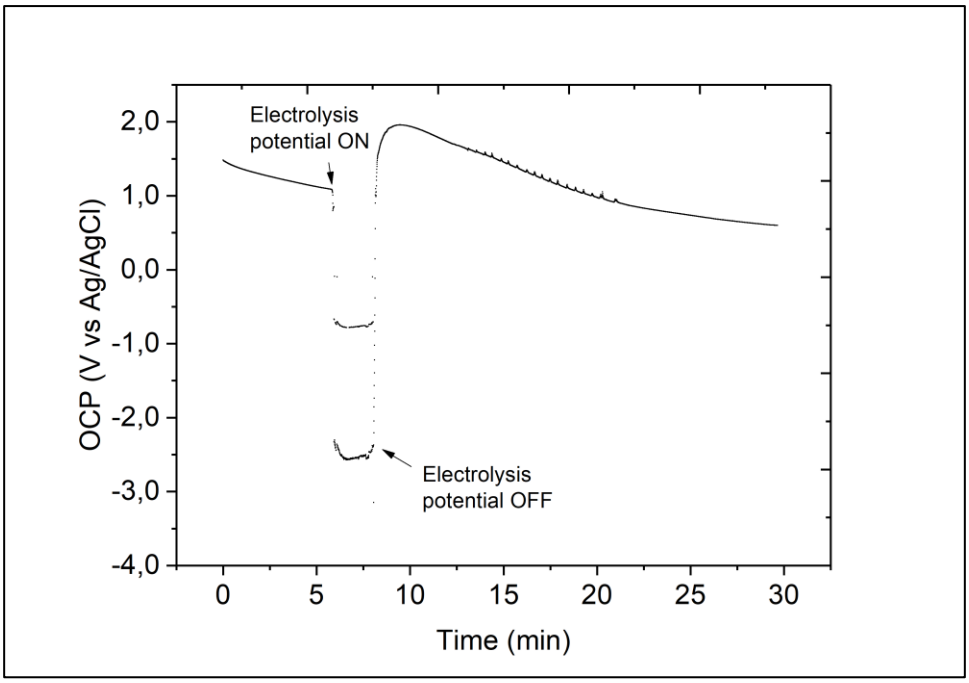

Figure 4.0.30 - OCP trend measured over microelectrode in CB buffer solution before, during and after O_2 generation.

Results, shown in Fig. 4.30, feature an increasing OCP value as consequence of the electrolysis phenomenon and a decreasing when potential is no longer applied to WE, in an attempt to restore equilibrium (starting) value of OCP. These results confirmed the OH^- consumption after O_2 evolution, supporting our starting assumption.

The following step was to perform test of our probe during H_2 production. In Fig. 4.31 we show a dynamic OCP measurement of H_2 evolution in 1 N H_2SO_4 applying – 449 mV vs SCE at WE, complete of preliminary probe equilibration time (about 500 s).

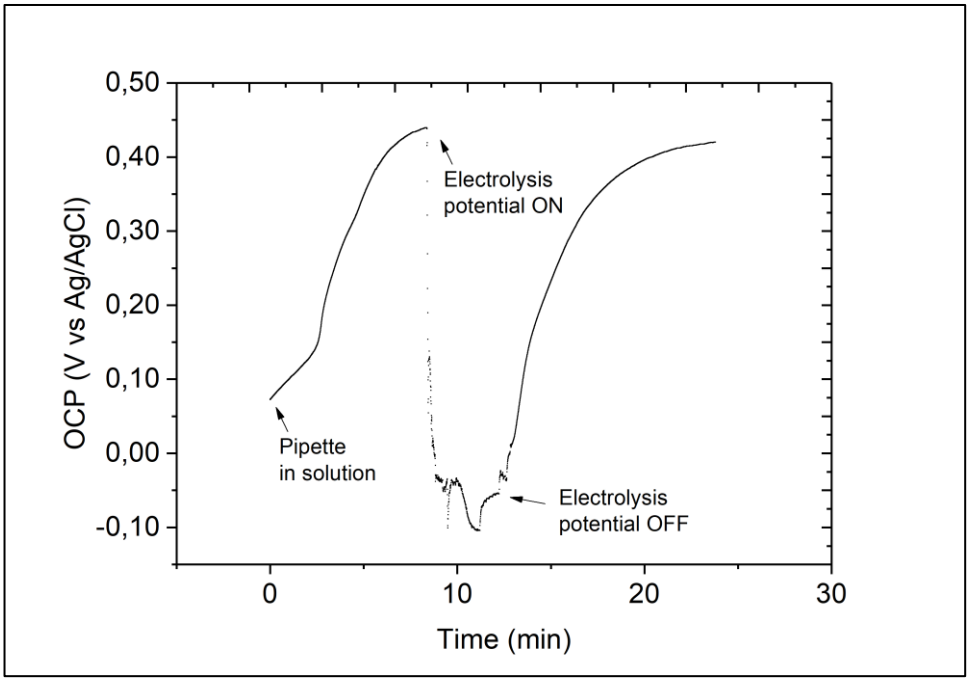

Figure 4.31 - OCP trend measured over μ-electrode in 1 N H_2SO_4 solution before, during and after H_2 generation

The system tended to restore its OCP equilibrium value, see Fig. 4.31; in particular, the value measured immediately after electrolysis resulted much lower than the final value because of OH^- production after hydrogen evolution (as stated before, lower OCP is related with higher pH). This result demonstrated that our device was suitable for pH measurement after both H_2 and O_2 evolution, that the trend of OCP was coherent with OCP vs pH calibration curves shown in Fig. 4.22. Moreover, these OCP-evolution curves allowed evaluating probe equilibration time and its impact on the measurement.

We planned a final experiment, comparing OCP trends after H_2 and O_2 evolution, respectively, in the same solution. To achieve this result, we chose to operate in

1 M KOH solution applying 1024 mV vs SCE at WE; for the oxygen curve measurement, the probe was placed 100 µm over the WE, for the hydrogen curve the probe was moved over the CE, maintaining the same distance from the electrode. We show the overlay of these plots in Fig. 4.32: it was noticeable how curves had different trends after electrolysis potential was switched off, validating results obtained in previous experiments and showing how our probe was suitable for OCP measurements in any pH condition and for evolution of both H_2 and O_2.

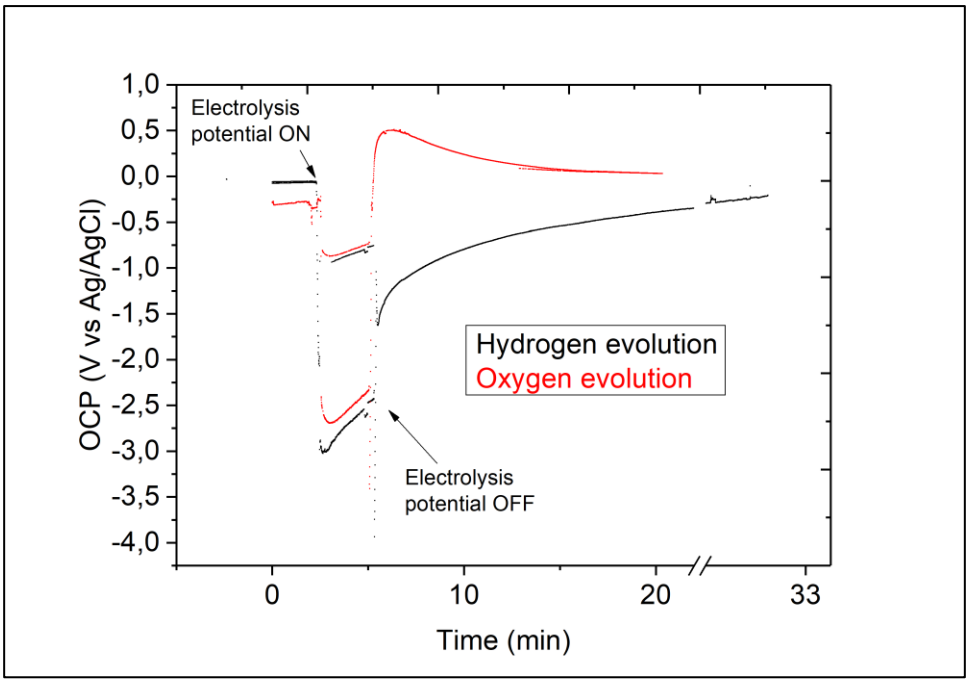

Figure 4.32 - Overlap of OCP vs t curves measured over microelectrode in 1 M KOH solution before, during and after H_2 (black) and O_2 (red) generation.

4.3 – Study of Co-Pi photoelectrocatalyst

Among the many photoelectrocatalysts, during the part of the project described in this paragraph we chose to analyse an oxygen-evolving catalyst well known for its reliability and its nominal faradaic efficiency of 100 %: a Co-Pi electrode, also known as Nocera's catalyst from the scientist who discovered it. The ground-breaking work that featured this catalyst[5] raised a great interest due to the properties of this material. It was formed *in situ* from earth-abundant metal ions (Co^{2+}) in aqueous solution; was self-repairing since the work potential is the same of cobalt deposition; allowed the

generation of O_2 at low overpotentials, neutral pH, 1 atm and room temperature (many elements of natural photosynthesis).

4.3.1 – OCP over ITO-based photoelectrocatalyst

After last OCP sensing experiments, our device was now ready to be used as sensor for a catalysed water splitting process. The goal of this experiment was to see if our probe was potentially suitable for pH sensing in a different buffered media (PBS 0.1 M, pH 7.4) and to set the Co-Pi catalyst as a standard for future measurements on other catalysts due to its faradic efficiency. At first, we analysed O_2 evolution over a sample of Co-Pi catalyst deposited over an ITO-covered glass slide electrode (Fig. 4.33).

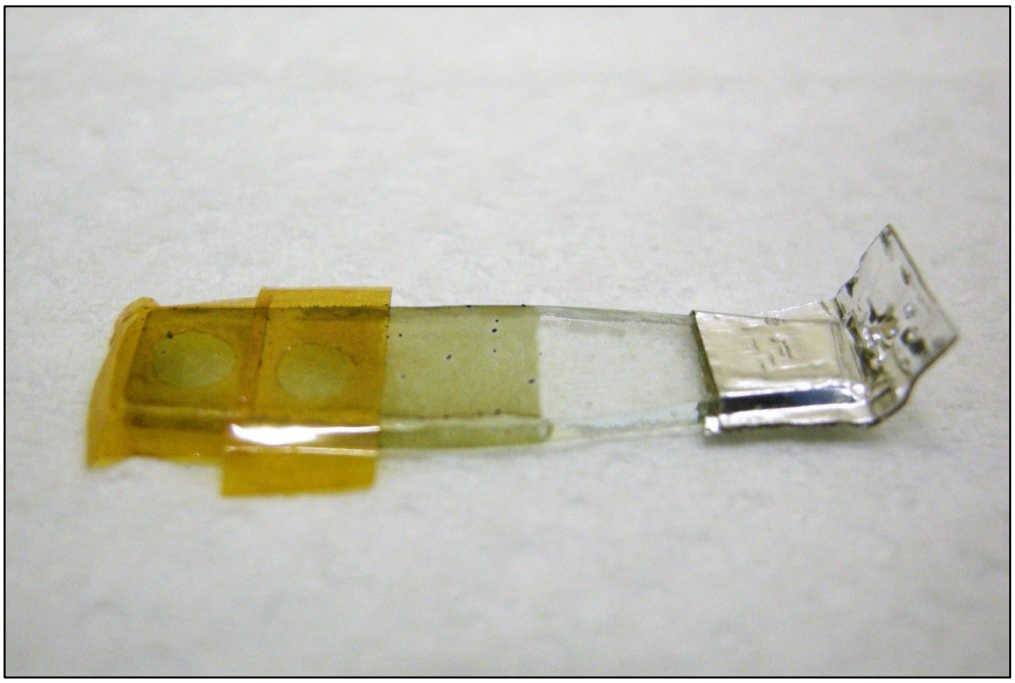

Figure 4.33 – Co-Pi catalyst (in brown) over ITO. Conductive tape provided electrical connection.

ITO was chosen as substrate for deposition of photoelectrocatalysts thanks to its transparency and conductivity. Experiments were performed with the same set-up of the gold-coated glass slide sensing tests (cf. section 4.2.2), while there was a change in the aqueous buffered solution and in the voltage applied to the electrode (1046 mV vs SCE) to generate oxygen. Results obtained (Fig. 4.34) were consistent with the output of previous experiment and comparing the OCP vs time curves with the OCP vs

pH calibration we were able to estimate a pH ≈ 1 in the environment surrounding the probe, a significant drop with respect to the bulk pH. After some minutes, OCP tended to go back to the starting value.

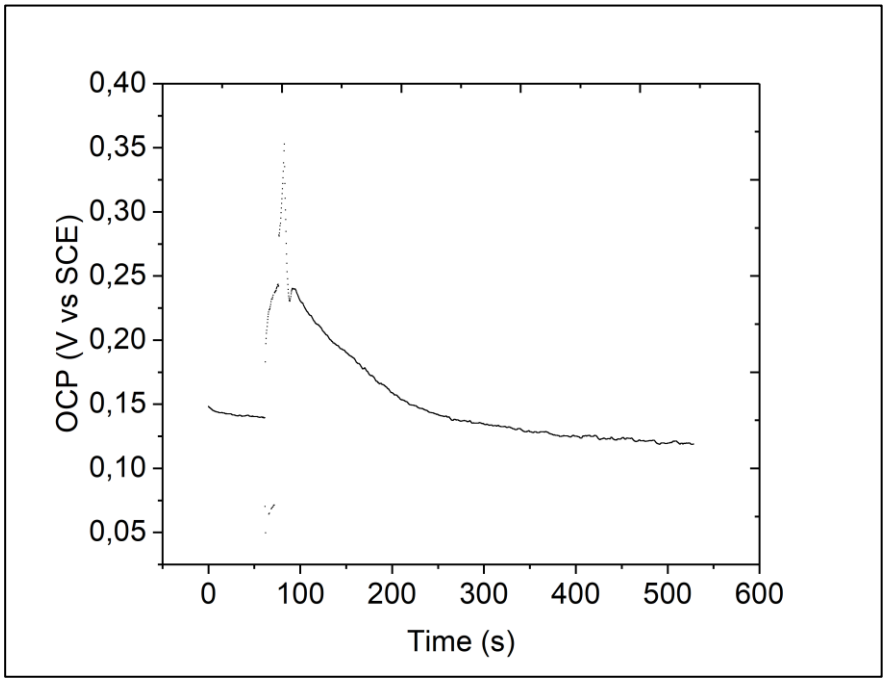

Figure 4.34 – OCP vs Time curve for oxygen evolution over ITO-based Co-Pi catalyst.

4.3.2 – Deposition over Au microelectrodes

According to the main aim of this project - the development of a device useful for pH mapping at local scale of microstructured samples - the following step was to perform pH sensing over microstructured Co-Pi catalyst. For this reason, we developed a protocol for deposition of Co-Pi over micro-Au electrodes. Gold was chosen as substrate for its excellent electrical conductivity and because it was relatively easy to create a micropattern using photolithography in Au rather than in ITO.

Following the experimental indication of Ref. 5, we performed a chronoamperometric deposition at a potential of 1046 mV vs SCE in a 0.5 mM $Co(NO_3)_2$, 0.1 M PBS solution. First attempt of deposition was carried out for 8 hours without stirring and Fig. 4.35 shows the Current vs Time curves obtained: the presence of steps in the curve was a consequence of a lower current intensity that passes through the WE. This was a consequence of the reduction in electrodical area due to the formation of oxygen

bubbles at the surface, since the deposition potential was the same that was applied for O_2 evolution (this condition gave the self-repairing feature to the catalyst).

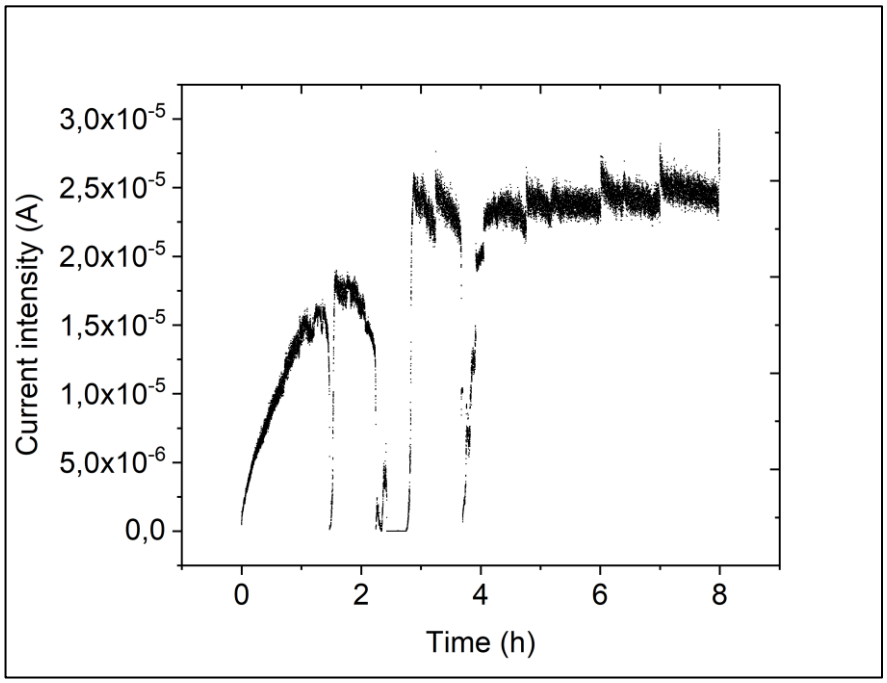

Figure 4.35 – Deposition of Co-Pi catalyst without stirring the solution. Steps in the curve are representative of strong bubble formation at the surface of the electrode.

In order to eliminate this drawback and to provide a continuous feed of Co^{2+} ions at the surface, we tried stirring the solution during the 8 hours of deposition: results are shown in Fig. 4.36.

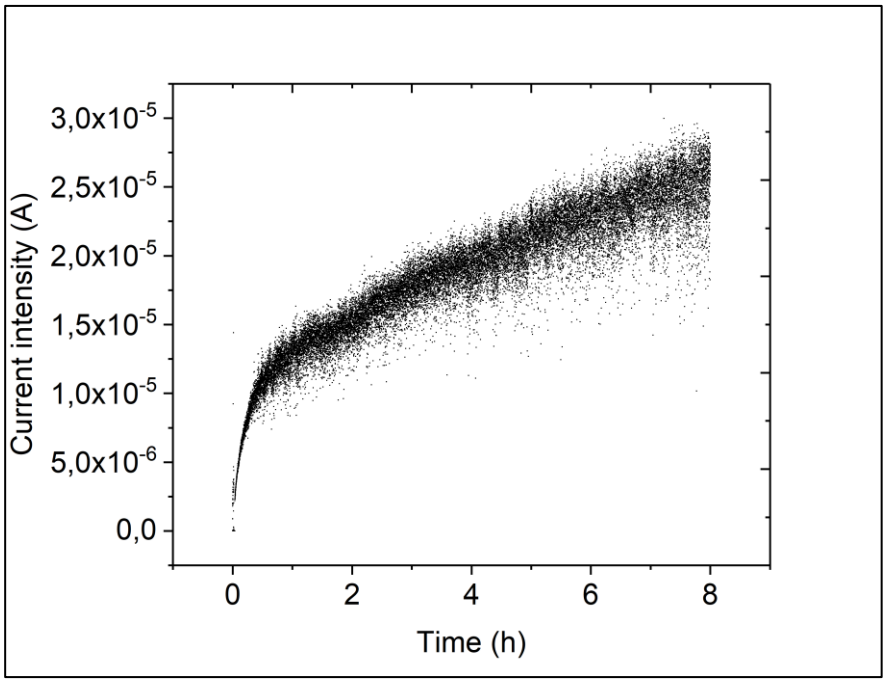

Figure 4.36 - Deposition of Co-Pi catalyst with stirring introduced.

From these data we could state how the stirring influenced deposition, since the huge scattering of points derived from a non-optimized stirring speed: a deposition with variation of stirring frequency is depicted in Fig. 4.37. We were therefore able to choose the ideal stirring value and to integrate it in this brand-new deposition protocol.

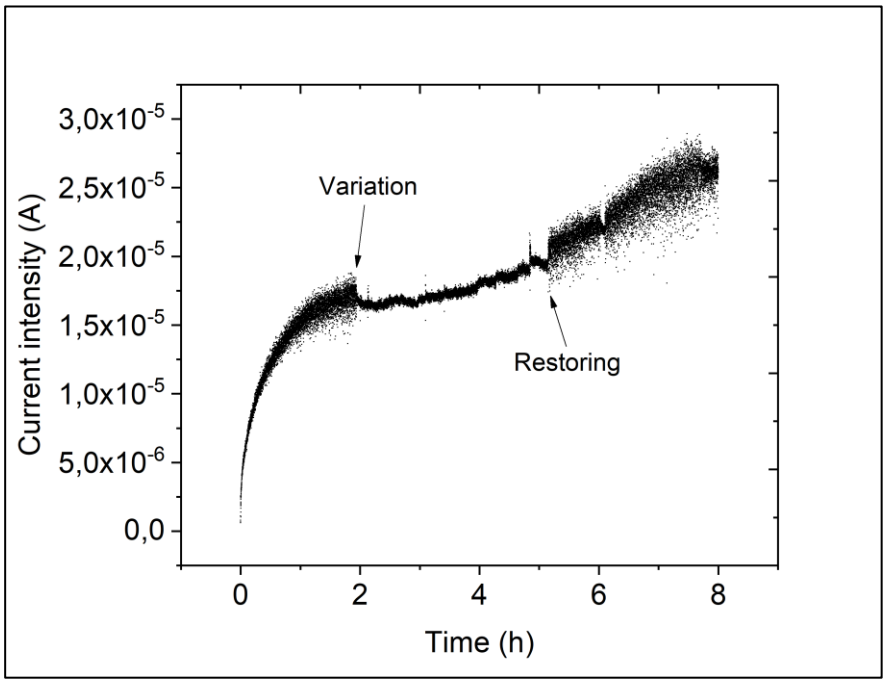

Figure 4.37 - Deposition of Co-Pi catalyst with variable stirring frequency. Ideal frequency was 2500 rpm.

To confirm the successful deposition of Co-Pi catalyst, pictures at optical microscope were taken (Fig. 4.38) to identify the area where deposition took place.

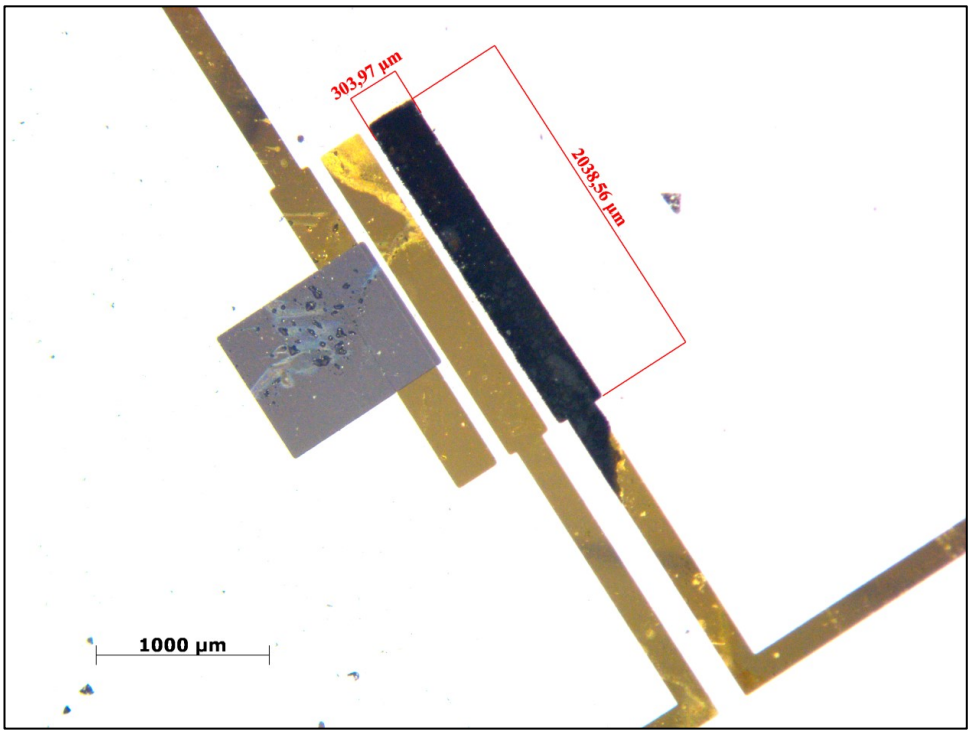

Figure 4.38 - Optical image of microelectrodes array. It is observable the Co-Pi catalyst (black) deposited over one gold microelectrode.

It is interesting to see how the microelectrodes were darker compared to the catalyst deposited over ITO (Fig. 4.39).

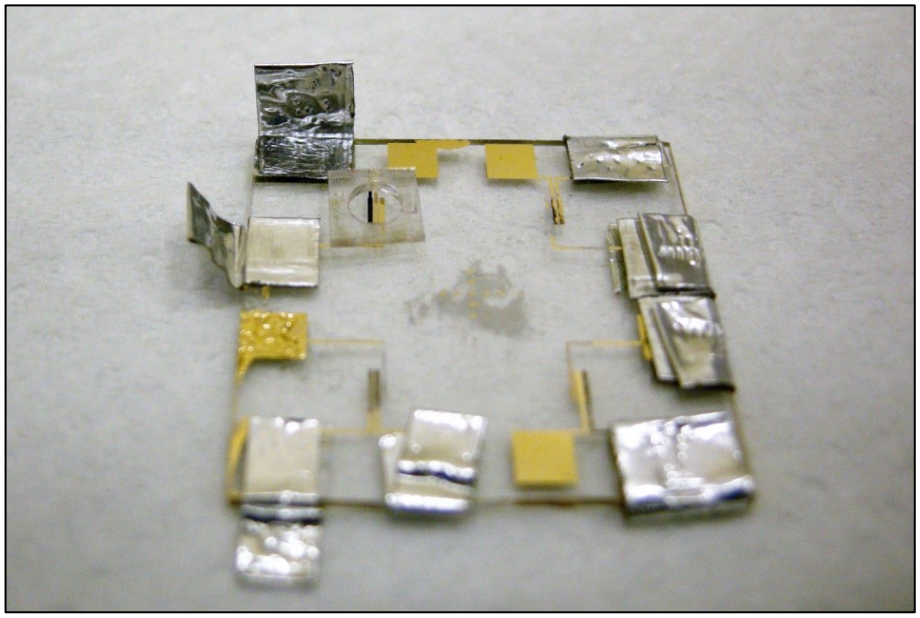

Figure 4.39 - Array of microelectrodes with Co-Pi catalyst (in black). It is visible the silicon gasket that defines the volume of the electrochemical cell.

This result could be just a feature due to the different conductive substrate (gold). In order to state if there is also a difference in the catalyst deposited, an EDX analysis was performed on the deposited substrate; results, shown in Fig. 4.40, confirm the presence of cobalt and phosphorus with a spectrum equivalent to that of reference work.

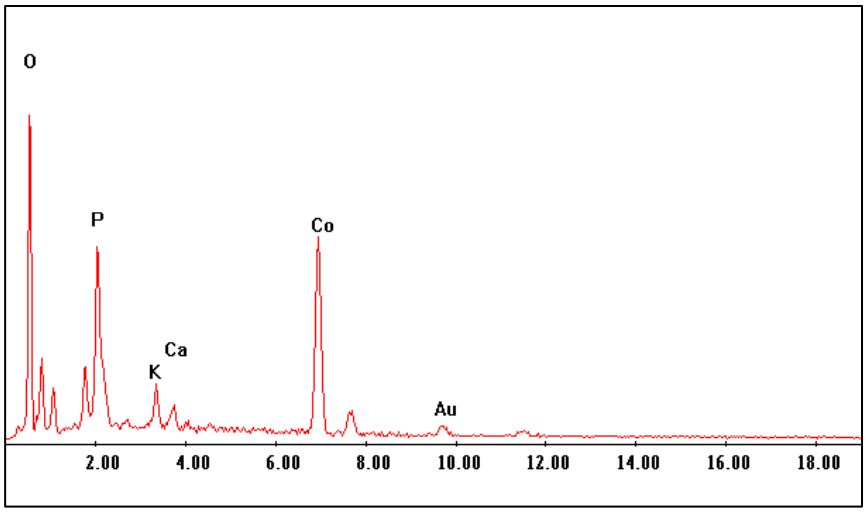

Figure 4.40 - EDX spectrum of deposited catalyst. The Co and P peaks are noticeable and related to the presence of Co-Pi catalyst.

SEM images were taken simultaneously to EDX, showing a cracked structure very similar to Nocera's main work[5] (Fig. 4.41).

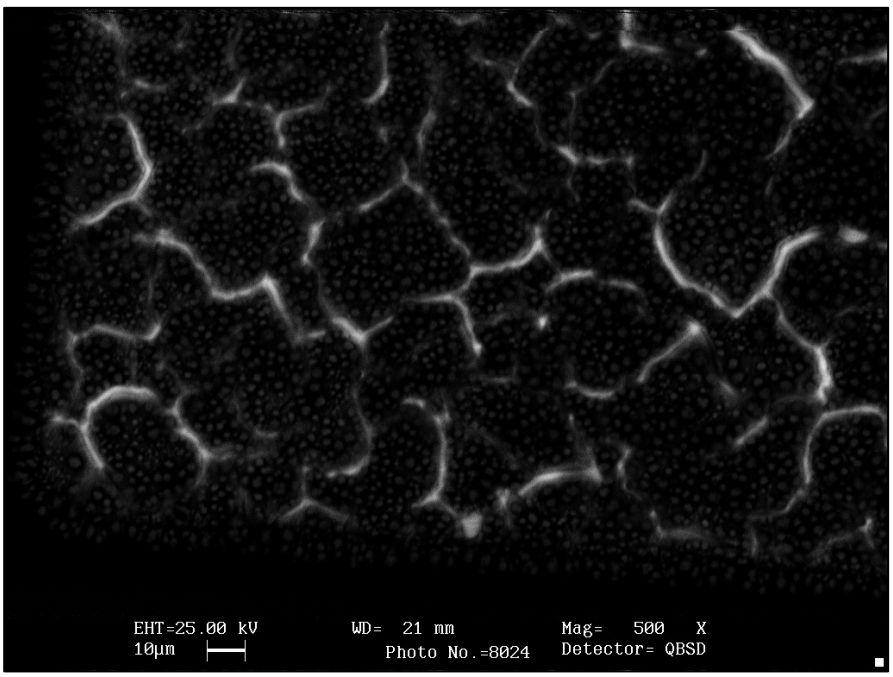

Figure 4.41 - SEM image of Co-Pi catalyst surface.

4.3.3 – OCP over Au-based photoelectrocatalyst

After the deposition protocol was set, we performed more sensing experiments on this new microstructured substrate. Results were compared with data of previous experiments (with ITO substrate) in order to see if the OCP trend was the same and therefore to state if the catalyst deposited over Au was equivalent to the "standard" one deposited over ITO.

Set-up for both the sensing part and the electrolysis part were maintained as in previous OCP measurements over bare microstructured gold, while the experimental conditions were the same as previous OCP sensing experiments over the CoPi/ITO catalyst. Data in Fig. 4.42 show the OCP vs time curve: the trend was the same of sensing experiments over the ITO-based catalyst.

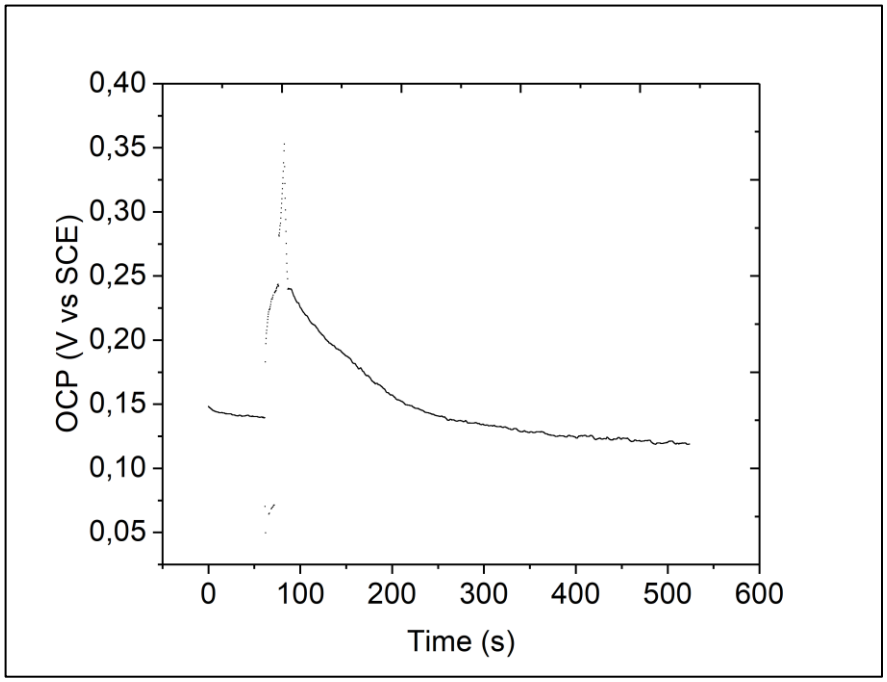

Figure 4.42 - OCP vs Time curve for oxygen evolution over Au-based Co-Pi catalyst.

This last experiment confirmed the possibility to perform sensing experiments over a common electrocatalyst with the SICM-EC device.

4.4 – Microfluidics studies

The final part of the project was focused on the application of a fully characterised photoelectrocatalyst to microfluidic systems. This is indeed one of the most challenging and promising applications of photoelectrocatalysts for water splitting. It would combine the long-described advantages of photoelectrocatalysis for water splitting reactions with the positive features of microfluidic systems, such as the low volume of liquid required for running the device, the fine control of reaction conditions (such as pressure, temperature, etc.), the possibility of better separation of H_2 and O_2.

4.4.1 – Preliminary design of microfluidic system

To approach the world of microfluidic systems, a great amount of information must be taken in account. The fluid dynamic phenomena occurring in a microfluidic channel are different from those in a standard electrochemical cell, as well as the materials that could be used for fabrication of the microchannel have different requirements than the standard ones used, for example, in the fabrication of regular chemical reactors.

To have a solid starting point, we chose a very recent paper[6] on coupling of water splitting and microfluidics. The authors designed a smart set-up, with two platinised electrodes generating hydrogen and oxygen: over them, electrolyte is flushed in a microchamber 400 μm thick. This device presented one inlet and two outlets for electrolyte: moreover, a practical application of this device should feature a side channel for hydrogen extraction. The solution proposed by the authors may be implemented and optimised with useful intuitions.

In the beginning, we focused on the final application of the device. To have a fully engineered photoelectrocatalytic device, its features must be in agreement with the requirements of the practical applications. Since the main goal of the photoelectrocatalytic device is the exploitation of water splitting to generate hydrogen and oxygen, a practical application of this device must feature a collection facility for gas extraction. It is theoretically proposed by the authors of the work by the aforementioned lateral channel, but not implemented in the fabricated device. This solution, however,

is not practical since any occlusion in the channel occurring from the junction point to the outlet of electrolyte will cause a reduction in flow, causing therefore the electrolyte to flux inside the secondary gas channel and therefore contaminating the pure stream of gas. We propose a solution to this problem.

First, it is mandatory to switch from a microchamber structure to a microchannels one. The main reason is to avoid recombination of molecular hydrogen and oxygen, a phenomenon that certainly occurs if the two gases are produced in a common, close environment like the microchamber. The proposed device presented two groups of four microchannels each: one array has the photoelectrocatalyst for to oxygen production; the other has the platinum CE for hydrogen production. The electrical conductance is provided by using a common electrolyte inlet for both arrays of microchannels. Each array of microchannels is connected to a dedicated outlet, in which the produced gas goes along with the wasted electrolyte (Fig. 4.43). After that, a porous membrane is placed to provide gas separation and subsequent collection.

Using microchannels, the electrode contact area will not lower since we planned to use multiple microstructured electrodes: summing up, they will have the same surface area of the planar electrode described in reference.[6] Moreover, such modular system is way more flexible than a microchamber and can be adapted to the requirements of different users. The microchannels featured in our project are 25 mm x 400 µm x 400 µm, while the dimension of the photoelectrocatalytic electrode are 20 mm x 300 µm x 150 nm (Fig. 4.38). The electrodes and the microchannels are axially placed in order to exploit completely their surface area. They need to be connected to a potential of 1046 mV vs SCE in order to perform photoelectrocatalytic water splitting: this electric potential may be provided by a potentiostat.

Another important contribution to the improvement of the proposed device is in the material used for production of microchannels. The authors used PDMS, a widely used material for microfabrication through replica molding. However, this material has the critical drawback to be permeable to gases, in particular to oxygen and hydrogen. This characteristic makes this material not useful for our purposes. For this reason, we switched towards PMMA. This polymer is well known in the industry of microfabrication and commonly used for its plastic properties. Through hot embossing, it is possible to fabricate an array of microchannels that are not permeable to gas,

therefore incrementing the yield of the overall device. Fig. 4.43 shows a schematic representation of our microfluidic system.

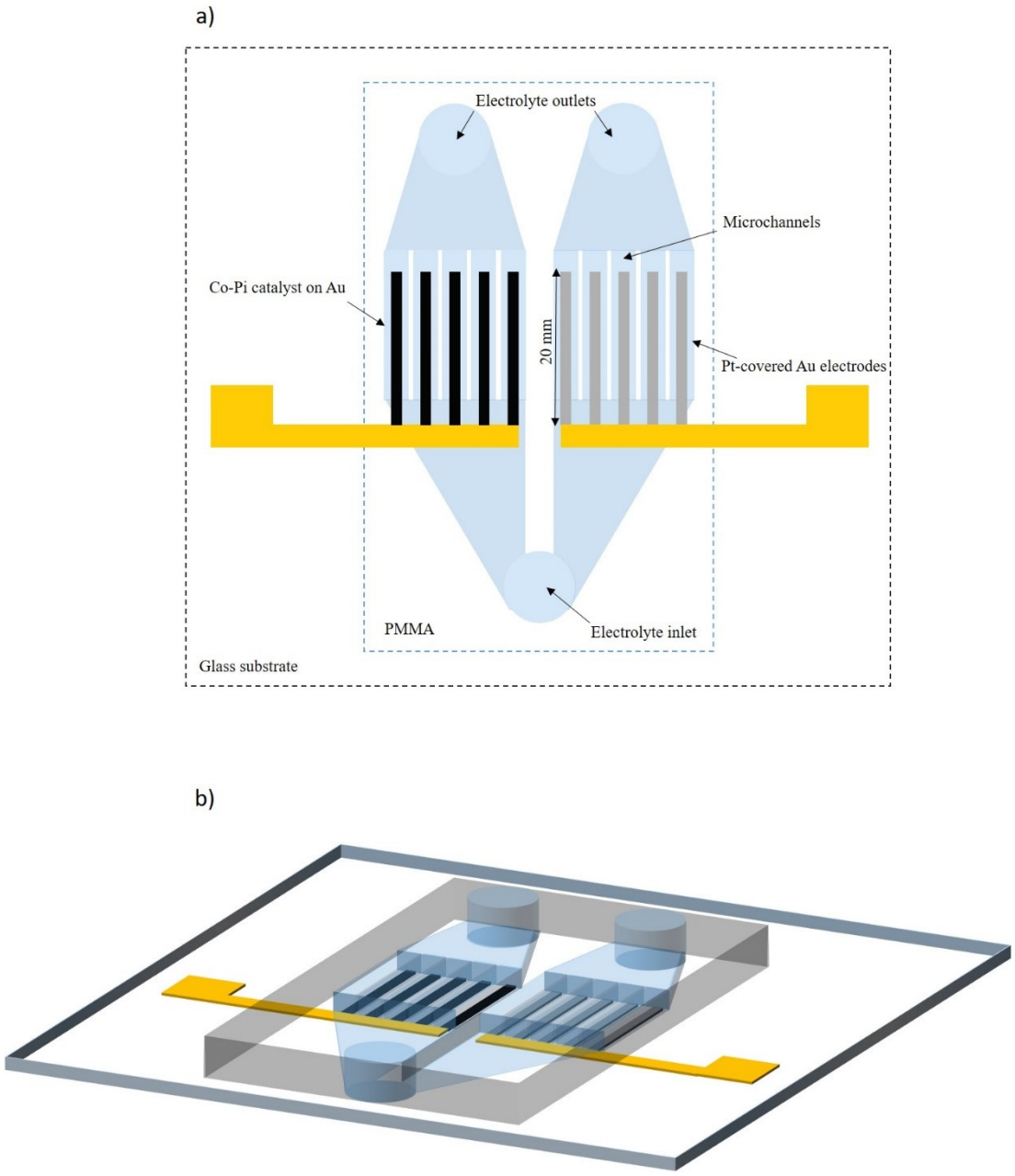

Figure 4.43 - Schematic illustration of the design of the microfluidic device. The photoelectrocatalyst and the platinised electrodes are represented in black and grey, respectively. The microfluidic path of the electrolyte is represented in light blue. a) bottom view; b) 3-D view.

This proposed set-up maintains the easiness of fabrication and the use of common materials like the reference one, eliminating the drawbacks in order to maximise efficiency of water splitting process.

4.4.2 – Fluid dynamics simulations

In this paragraph we describe the performed fluid dynamics simulations with COMSOL software. The aim of this work was to find the proper fluid parameters for the microfluidic system that ensure a behaviour similar to the static conditions studied so far. In this way, it was possible to correlate the information obtained on the photo-electrocatalyst in static conditions to the microfluidic system, while maintaining the intrinsic, positive features of microfluidic applications (low volume of liquid, better separation of H_2 and O_2, etc.).

Flow rate values commonly used in practical microfluidic applications were adopted. Our interest was focused towards the oxygen evolution reaction occurring inside the channels containing the Co-Pi electrocatalyst; numerical simulation was useful for selecting the ideal flow rate. This value should ensure the minimal variation in concentration of reagent, in order to have a homogeneous process in each point of the electrode, simulating the static experimental conditions used in previous experiments; moreover, the flow rate must not be too high to avoid mechanical damages to the channels or to the catalyst.

To describe the photoelectrocatalysed process, it is important to consider some chemical and kinetic data, like the diffusion coefficient of the reactant,[7] its concentration (the Co-Pi photoelectrocatalyst works at pH 7, so it is 10^{-7} mol/L) and the effective rate constant of the reaction for this specific catalyst.[8] The geometry of the device is known, so all the necessary parameters for a realistic simulation were available.

Considering the schematic design described in the previous section and represented in Fig. 4.43, we calculated the electrolyte velocity over the catalyst for each inlet flow rate. E.g., an inlet flow rate of 10 µL/min is equivalent to a velocity of 10^{-4} m/s. Fig. 4.44 shows the predicted values of the spatial concentration distribution of reactant over the electrode surface: only the most representative flow rates were considered. The value 100 µL/min (Fig. 4.44-a) gave the best performance for the microfluidic system: the electrolyte concentration does not change significantly along the electrode, mimicking the static conditions studied using the integrated device. When flow rate is lower (10 µL/min, 1 µL/min, 100 nL/min), the variation in concentration becomes more significant, as highlighted in Fig. 4.44-b,c,d.

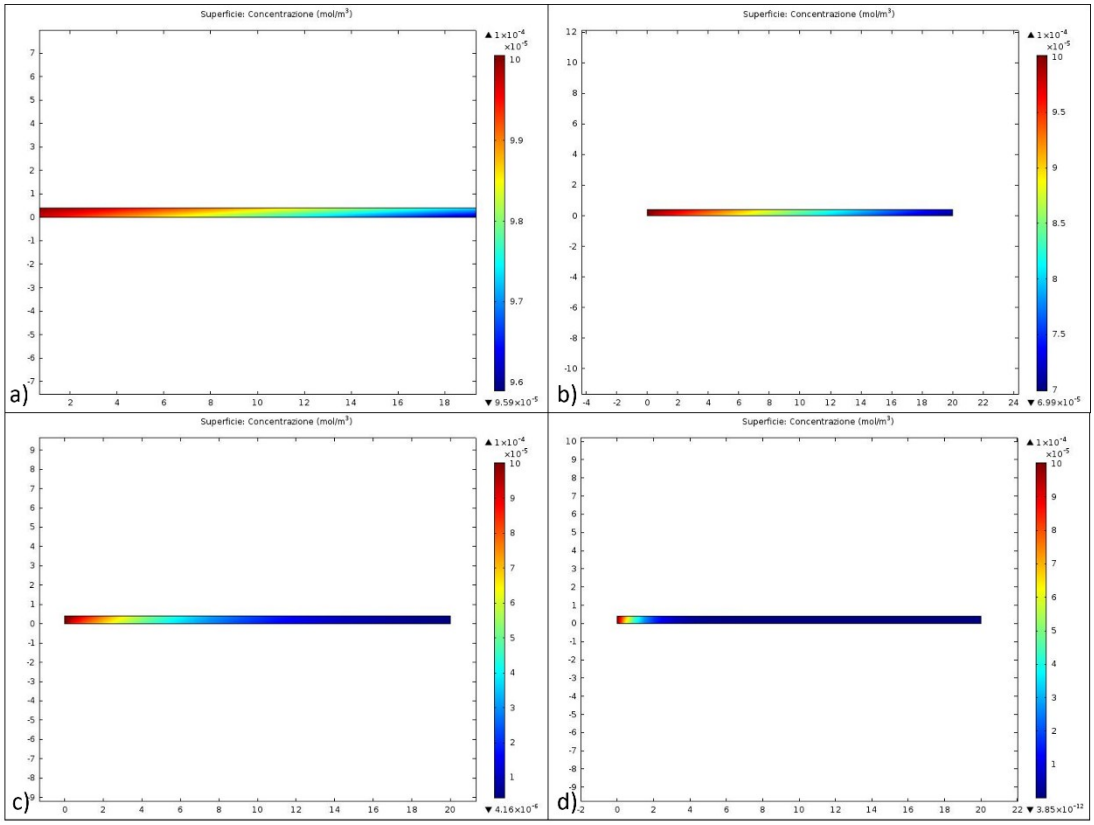

Figure 4.44 - Fluid dynamics simulations for different inlet flow rates. a) 100 µL/min; b) 10 µL/min; c) 1 µL/min; d) 100 nL/min. These simulations are referred to a single channel.

The 100 µL/min flow rate may not seem a common value for microfluidic devices, but it is important to relate it to the non-conventional structure of our device. We used a common inlet to provide electrical conductance between the two arrays of electrodes: however, this inlet needs to feed eight microchannels, not just a single one as in a classic microfluidic device. Moreover, the flow rate is higher compared to Ref. 6 because the channel height proposed in that reference paper (400 µm)[6] is much higher than a typical microchannel (e.g. 15 µm),[9] but the liquid velocity are comparable.

4.5 – Chemicals, materials and instrumentation

This final paragraph collects all the chemicals, materials and instrumentation used during the experimental part of this thesis.

Platinum(II) acetylacetonate 97%, potassium hexacyanoferrate(III), hexaammineruthenium(III) chloride, xylene, sulfuric acid, potassium hydroxide, sodium carbonate, sodium bicarbonate, sodium diphosphate, sodium orthoborate, sodium citrate, potassium chloride, PGMEA, SU-8-remover, cobalt(II) nitrate hexahydrate, phosphate buffered saline solution (Sigma Aldrich), SU-8-2005 (MicroChem), $H_2PtCl_6 \cdot 6H_2O$, lead acetate (abcr GmbH) were used as received. Pt and Ag wires were bought from Advent, the insulating spray paint V-66 was provided by Due-ci Electronic s.n.c.. Platinum(II) acetylacetonate was used as precursor for Pt deposition with MOCVD; insulating spray paint and xylene were used for the creation of the insulating layer. Potassium hexacyanoferrate(III) and hexaammineruthenium(III) chloride were used in the electrochemical characterization procedure. Sulfuric acid, potassium hydroxide, sodium carbonate, sodium bicarbonate, sodium diphosphate, sodium orthoborate, sodium citrate, potassium chloride were used to prepare buffered solutions for potentiometric measurements. SU-8-2005, PGMEA and SU-8-remover were used in the photolithographic production of the array of microelectrodes. $H_2PtCl_6 \cdot 6H_2O$ and lead acetate were used in the platinization of the microelectrodes. $Co(NO_3)_2 \cdot 6H_2O$ and PBS were used for deposition of Co-Pi photoelectrocatalyst.

Borosilicate capillaries were provided by Sutter Instrument Co., soda lime glass substrate for microfabrication was supplied by Waldemar Knittel. The heater capillary puller was model PP-830, Narishige. Potentiostat used was Metrohm Autolab. SICM used was the XE-Bio model, Park Instruments. SEM was Leica / Cambridge / Leo S-440.

Bibliography

1. Mello, R. M. Q. & Ticianelli, E. A. Kinetic study of the hydrogen oxidation reaction on platinum and Nafion® covered platinum electrodes. *Electrochim. Acta* **42,** 1031–1039 (1997).

2. Jin, J. *et al.* An experimental and modeling/simulation-based evaluation of the efficiency and operational performance characteristics of an integrated, membrane-free, neutral pH solar-driven water-splitting system. *Energy Environ. Sci.* **7,** 3371–3380 (2014).

3. Oruc, M. E., Desai, A. V, Nuzzo, R. G. & Kenis, P. J. A. Design , fabrication , and characterization of a proposed microchannel water electrolyzer. *J. Power Sources* **307,** 122–128 (2016).

4. Dešić, M. N., Popović, M. M., Obradović, M. D., Vračar, L. M. & Grgur, B. N. Study of gold-platinum and platinum-gold surface modification and its influence on hydrogen evolution and oxygen reduction. *J. Serbian Chem. Soc.* **70,** 231–242 (2005).

5. Kanan, M. W. & Nocera, D. G. In Situ Formation of an Water Containing Phosphate and Co 2 +. *Science (80-.).* **321,** 1072–1075 (2008).

6. Oruc, M. E., Desai, A. V., Kenis, P. J. A. & Nuzzo, R. G. Comprehensive energy analysis of a photovoltaic thermal water electrolyzer. *Appl. Energy* **164,** 294–302 (2016).

7. Lee, S. H. & Rasaiah, J. C. Proton transfer and the mobilities of the H+ and OH- ions from studies of a dissociating model for water. *J. Chem. Phys.* **135,** (2011).

8. Sonwalkar, H. S. & Haram, S. K. Kinetic Analysis of the Oxygen Evolution Reaction (OER) Performed with a Cobalt-Phosphate Electrocatalyst. *ChemistrySelect* **2,** 3323–3328 (2017).

9. Modestino, M. A. *et al.* Integrated microfluidic test-bed for energy conversion devices. *Phys. Chem. Chem. Phys.* **15,** 7050 (2013).

5 – Conclusions and future perspectives

The aim of this thesis was to provide useful results for technological advance in the field of photoelectrocatalytic water splitting. As written before, this electrochemical process involves many aspects that are in the spotlight of technological improvement. In this project we focused in particular on investigation of photoelectrocatalysts, with emphasis on pH sensing during water splitting. We therefore created a different coupled sensing electrode, with new electrodic material and insulating coating easily realised, suitable for both localized pH sensing and quantitative measurement of chemical species at local scale. We used this integrated probe for pH sensing over microstructured Co-Pi photoelectrocatalysts and we proposed an optimised device to integrate these electrodes inside microfluidic channels. In this chapter, the experimental results obtained in the last three years of research are exploited to draw conclusions, useful to demonstrate how the declared goals of the project have been reached.

5.1 – Pipette design and fabrication

Taking account of current research on solar hydrogen production (particularly on photoelectrocatalytic water splitting), we focused on the current methods used for characterisation of photocatalysts. In particular, from state-of-the-art works the urge for an alternative device was rising: its main characteristics would have been the suitability for fabrication even in non-specialised laboratories, while maintaining the reliability of current probes.

We were inspired by hot papers in this field of science and chose a single-barrel pipette design, obtaining pipettes with an opening diameter that was a good compromise between maximum resolution and easiness of fabrication. This latter aspect is due to the use of a heater capillary puller instead of a much more expensive CO_2 laser puller.

Platinum, as stated previously, is a widely renowned good material for electrochemical studies and its nature of noble metal ensures stability over time. Compared with IrO_2, Pt can be deposited with highly reproducible methods (MOCVD) thanks to

its metallic nature. Moreover, platinum has demonstrated to be affordable for OCP measurement with a quasi-Nernstian behaviour.

The brand-new insulating coating procedure satisfied the minimal requirements: the result was a non-expensive, practical material suitable for our applications. Electrochemically characterising the regenerated pipettes we were also able to demonstrate how the OCP sensitivity was not affected from the regeneration procedure: concluding, the insulating coating did not damage the active platinum layer, both when it was deposited and when it was removed with xylene. Anyway, comparing several pipettes through CVs in $Ru(NH_3)_6Cl_3$ it is clearly noticeable how each Current vs Concentration trend is different, even if the current intensity values are in the same order of magnitude. Therefore, our conclusion is that every pipette is “self-standing” and must be calibrated before use. Improvements in reproducibility of the fabrication procedure can be surely achieved by optimising the dip coating process: in this phase of study, we focused our attention on to the overall "user-friendliness" of the fabrication method.

Concluding, the electrochemical experiments conducted in SICM set-up confirmed the results obtained with previous, standard three-electrode set-up, as seen in section 4.1.5.

5.2 – Approach to sensing

Some useful conclusions may be drawn from the direct sensing experimental part. Most importantly, direct sensing of H_2 produced during electrolysis of water seems unrealisable in a short-term scale. This is due to the inability to perform direct oxidation of molecular hydrogen dissolved in the solution. Moreover, the low electrodical surface of the integrated probe makes impossible to appreciate any difference in the shape and intensity of CV peaks related to platinum oxide formation and reduction: as stated in section 4.2.1, those peaks are influenced by the presence of H_2 in solution. Lastly, future perspectives on a direct approach to hydrogen sensing with the SICM-EC device will need to take in account exclusively a pure source as hydrogen

supply, like a gas stream or a cylinder. This will avoid false positive signal, for example the peak referable to oxygen seen in the previous chapter, and will increase hydrogen solubility in the solution.

The indirect approach was far more satisfactory. Preliminary experiment of OCP measurement in different pH media showed the suitability of our device for this method of detection. First OCP measurements over the half gold-coated glass slide were useful to support experimentally the theoretical assumption of the creation of a pH gradient in the vicinity of the electrode as a consequence of an electrolytical process. This set the foundation of all subsequent experimental work.

Later experiments saw the integrated probe involved in OCP measurement in different solutions: those tests were useful to confirm the suitability of our device in any pH condition. Moreover, the aforementioned experiments were performed towards evolution of both hydrogen and oxygen: it is noticeable how curves had different trends after electrolysis potential is switched off. The interpretation to this phenomenon is the trend of the chemical system to restore the $[H^+]$ close to the electrode surface to that of the bulk solution. In this way, a pH gradient is generated and so forth there is a change in the OCP at the sensing electrode. If hydrogen is formed, H^+ will be consumed; if oxygen is formed, H^+ will be produced. Data showed the suitability for OCP measurements in any pH condition and for evolution of both H_2 and O_2.

5.3 – Studies on Co-Pi catalyst

In order to have a practically useful device for electrocatalytic research, it was mandatory to test its potential application on a general electrocatalyst. During our experiments we were able to develop a new protocol for deposition of Co-Pi over a substrate suitable for our experiments. Results obtained were consistent with literature expectations, as emerged from characterisation with EDX technique.

Then, we approached the OCP sensing of the Co-Pi catalyst deposited over gold and the results were compared with data obtained from sensing of the standard Co-Pi/ITO electrode. In both cases, the OCP trend measured during the experiment is typical of an oxygen evolution experiment: this assumption is based on the data of the

OCP sensing experiments over platinised microelectrodes. This result confirmed theoretical expectation, since Co-Pi is a catalyst for oxygen evolution reactions. Moreover, the OCP vs Time curves of both catalysts are similar, confirming that the behaviour of the Co-Pi electrocatalyst is not substrate dependent.

Future perspectives on this experimental part will include simultaneous pH sensing and topographical imaging, exploiting the integrated nature of the EC-SICM probe. The final aim is to obtain time-dependent, 3-D images of pH gradient: in this way, by looking at how pH changes and relating it to oxygen production, it is possible to evaluate the effect substrate structure on the reaction rate. The smaller the opening diameter of the pipette, the higher the resolution of this map.

5.4 – Microfluidic applications

In the final part of this work, we studied the possibility of integrating the Co-Pi photoelectrocatalysts into a microfluidic device. The goal was to design a functional system useful for optimising the production rate of oxygen and hydrogen, based on the indication coming from the OCP sensing with the integrated SICM-EC probe.

We first provided the design of a microfluidic system based on previous, recent literature works. The main features were revisited and the materials were replaced with more performing ones, while maintaining their micromanufacturability. Furthermore, we used the proposed design to perform fluid dynamics simulations to identify the optimal flow rate for operating the device while ensuring a similar water splitting process to that occurring in static conditions.

Future perspectives will surely focus in detail on the fabrication of the designed device. It is possible to start a mass production of microstructured PMMA using the hot embossing microfabrication technology: in this way, it would be possible to prepare an array of multiple microfluidic devices and use the gas flow generated from water splitting as fuel source for energy production.

Acknowledgements

Nel concludere la mia tesi di laurea magistrale, tre anni fa, scrivevo i ringraziamenti pensando che fossero gli ultimi da destinare al settore accademico. Ma la vita, si sa, è uno stupore continuo, ed eccoci di nuovo qui dopo tre anni passati sulla breccia a fare il bilancio, scientifico e non, di questo periodo che non è errato definire unico. Nei sopracitati ringraziamenti dicevo di essere "al termine di questo lungo ed emozionante percorso, che è l'università"... Questa volta eviterò di scriverlo!

First and foremost, ringrazio Monica Giomo. Sempre disponibile a chiarimenti e a sperimentare vie nuove per il raggiungimento del risultato, il suo contributo al compimento di questo progetto è decisamente sensibile. Si è sempre interessata ai miei progressi ed ha contribuito all'approccio ingegneristico di questa tesi. Un ringraziamento particolare va al mio supervisore, Giovanna Brusatin, che in questi tre anni ha saputo trasformarmi da studente neo-laureato in professionista del settore scientifico. Grazie inoltre per avermi introdotto al mondo dell'ingegneria dei materiali e accettato nel gruppo di ricerca HyMat. *Last, but not least*, ringrazio Nicola Elvassore per aver messo a disposizione il suo laboratorio e per avermi coinvolto nelle attività del gruppo di ricerca Bio.E.R.A., dove sono stato ascoltato pur all'inizio non avendo competenze né ingegneristiche né biologiche. Il periodo trascorso nei due gruppi di ricerca, HyMat e Bio.E.R.A., è stato molto stimolante per la mia curiosità verso gli argomenti ed i problemi affrontati in questi tre anni, con approcci non necessariamente prettamente chimici. Un ringraziamento doveroso va fatto al centro di studi interdipartimentale "Giorgio Levi Cases", mio *sponsor* di questi tre anni di dottorato.

Durante questi tre anni ho avuto modo di affrontare ed imparare tecniche e discipline di cui prima conoscevo meramente l'esistenza: senza alcune persone che mi introducessero questi nuovi aspetti, una parte di questo lavoro di tesi non sarebbe stata possibile. Voglio quindi ringraziare Naida El Habra e Francesca Visentin, del CNR di Padova, per avermi fatto conoscere la tecnica MOCVD e per avermi permesso di utilizzare il loro macchinario per la deposizione di platino sulle pipette; Alain Jody Corso, innanzitutto perché è sempre un piacere ritrovare uno dei ragazzi del College, ma anche per l'aiuto nelle misure di profilometria; Alessandro Zambon, per il duplice e fondamentale aiuto nella parte di microfabbricazione e di simulazione fluidodinamica;

Marcella Bonchio ed i suoi "ragazzi", in particolare Andrea Sartorel ed Andrea Prevedello, per aver condiviso con me le loro conoscenze sugli elettrodi Co-Pi e per il supporto pratico durante questa parte sperimentale.

In questi tre anni ho incontrato molte persone, con le quali sono nate anche delle belle amicizie che spero durino nel tempo. Voglio salutare e ringraziare particolarmente i ragazzi dell'università, a partire dalle "veterane" Laura e Gioia, passando anche per Suji, Giulio e la Franca. Ci tengo molto a citare i giovani del Bio.E.R.A., presenti e passati, come Erika, Andrea (Bio.E.R.A. d'adozione), Max Vetro, Giulia, Seba, Silvia, Anna Contato, Fede, Ida, Ale Zambon, Gio Giobbe, Scarface, Gavino e Beggy. Con tutti abbiamo passato bei momenti assieme in questi periodi e con i colleghi dottorandi ci siamo spalleggiati nei periodi di alti e bassi. Anche se non ho lavorato direttamente con loro, in questi anni ho vissuto quotidianamente la vita da ricercatore con belle persone: Angio, Stu, Jimmy, Elena, Alberto, Paolone, Pietro, Pudu, Ale ed Acacio. Concludo con una menzione per i bioboys: è stato bello mangiare assieme ai lab meeting e partecipare alle feste del VIMM!

Tra i tanti amici, voglio ringraziare e salutare Matteo ed Ulisse per la compagnia e l'amicizia che ci hanno contraddistinto in questi anni, in particolare negli ultimi tre.

Menzione d'onore per il College. Il rapporto che si è creato nei cinque anni di università è forte come una malta cementizia: lo si è visto nel grande marriage dello zio Catte. Come era giusto che fosse, in questi tre anni abbiamo vissuto in luoghi diversi ma non per questo abbiamo perso i contatti o l'entusiasmo. Va fatta nello specifico una citazione necessaria a tutti coloro che si sono laureati "a casa mia", come Max Ingrosso, The Dick, il Giac, ma ringrazio tutti coloro che sono passati a trovarmi ed hanno lasciato una testimonianza sulla famosa lavagna Ratti. Ora che anche per me termina la grande avventura di Padova, possiamo dire conclusa la nostra esperienza del College: esso però continuerà a vivere con noi, perché noi siamo il College.

Dulcis in fundo, il ringraziamento più grande va alla mia famiglia: i miei genitori ed Elena. In questi anni hanno saputo confortarmi e spingere a proseguire, anche quando mollare tutto sembrava essere l'opzione più facile. Siete voi i migliori, se sono arrivato dove sono è solo grazie a voi.